Revealing The Ground State Properties Of The S=1/2 Kagomé Heisenberg Antiferromagnet: ^{17}O Single-Crystal NMR Investigations Of $ZnCu_3(OH)_6Cl_2$

REVEALING THE GROUND STATE PROPERTIES OF THE S=1/2 KAGOMÉ HEISENBERG ANTIFERROMAGNET: ^{17}O SINGLE-CRYSTAL NMR INVESTIGATIONS OF $ZNCU_3(OH)_6CL_2$

By

MINGXUAN FU, B.SC. HON

A Thesis
Submitted to the School of Graduate Studies
in Partial Fulfillment of the Requirements for the Degree
Doctor of Philosophy of Science

McMaster University

Doctor of Philosophy of Science (2015) McMaster University
(Department of Physics and Astronomy) Hamilton Ontario

TITLE: Revealing the Ground State Properties of the S=1/2 Kagomé Heisenberg Antiferromagnet: ^{17}O Single-Crystal NMR Investigations of $ZnCu_3(OH)_6Cl_2$

AUTHOR: Mingxuan Fu, B.Sc. hon

SUPERVISOR: Takashi Imai

NUMBER OF PAGES: 157

Abstract

The experimental quest for a quantum spin-liquid state (QSL) in frustrated magnetic systems addresses fundamental scientific interests, as this intriguing quantum phase provides excellent grounds for discovering exotic collective phenomena. $ZnCu_3(OH)_6Cl_2$ (herbertsmithite), an S=1/2 kagomé-lattice Heisenberg antiferromagnet, is the most promising candidate for experimentally realizing a QSL. However, despite years of intense research, the nature of its paramagnetic ground state remains highly debated. The root cause of the controversy lies in the difficulty in distinguishing the effects of defects from the intrinsic properties of the kagomé lattice.

In this thesis, we present ^{17}O nuclear magnetic resonance (NMR) measurements of an isotope-enriched $ZnCu_3(OH)_6Cl_2$ single crystal. We succeeded in distinguishing the intrinsic magnetic behavior of the kagomé lattice from the defect-induced phenomena down to $T \sim 0.01J$, where $J \sim 200K$ is the Cu-Cu super-exchange interaction. We identify NMR signals arising from the nearest-neighbor ^{17}O sites of Cu^{2+} defects occupying the Zn^{2+} interlayer sites. From the ^{17}O Knight shift measurements, we show that these Cu^{2+} defects induce a large Curie-Weiss contribution χ_{defect} to the bulk-averaged susceptibility at low temperatures. Moreover, our ^{17}O single-crystal lineshapes show no signature of nonmagnetic Zn^{2+} defects within the kagomé lattice, and therefore, we rule out “anti-site disorder” as a cause of the paramagnetic ground state in $ZnCu_3(OH)_6Cl_2$. Most importantly, we

demonstrate that the intrinsic spin susceptibility χ_{kagome} asymptotically tends to zero below $T \sim 0.03J$, indicating the presence of a finite gap $\Delta = 0.03 \sim 0.07J$ in the spin excitation spectrum; this gap is completely suppressed under the application of a high magnetic field $B_{ext} \sim 9T$. The behavior of low-energy spin fluctuations probed by the ^{17}O nuclear spin-lattice relaxation rate $^{17}1/T_1$ is consistent with the gap signature observed for ^{17}K. In short, our ^{17}O NMR results provide the first experimental evidence for a gapped QSL realized in $ZnCu_3(OH)_6Cl_2$.

Dedication

This thesis is dedicated, with love, to my mother.

Your endless enthusiasm for supporting me to achieve my dreams
is everything a daughter can ask for.

Acknowledgments

The process of completing a doctoral degree has been a tough yet rewarding journey. I know that I could not have accomplished this much without the support and guidance of many people. Here, I would like to take the opportunity to express my deepest gratitude to them.

First and foremost, I would like to give special thanks to Prof. Takashi Imai for his unfailingly rigorous and thoughtful supervision. I highly admire Takashi for his diligence, thoroughness and single-minded devotion to research. His high standards have driven me to dig deeper into my potential and bring out the best. More importantly, he believed unswervingly in me throughout the years it took me to complete my Ph.D. project and let me confront and triumph over a variety of research challenges on my own, which enormously enriched my learning experience. I can never thank him enough for his tireless guidance, enduring encouragement and blunt criticisms, without which I could never have made it this far.

I feel fortunate to have Prof. Bruce Gaulin and Prof. Graeme Luke as members of my supervisory committee. I gave my sincere appreciation for their valuable questions, advice and guidance throughout my Ph.D. research.

I am truly grateful to Dr. Tianheng Han and Prof. Young Lee for the fruitful collaboration; without their heroic efforts into synthesising the single crystal samples of $ZnCu_3(OH)_6Cl_2$ my research project could have never been possible.

Thanks also to Prof. Patrick Lee for the inspiring discussions about the gapped Dirac fermion model, which have been extremely helpful for improving the data analysis and interpretation presented in Chapter 4 of this thesis.

My heartfelt gratitude to our cryogenic facility manager, Dr. Paul Dube, and to the experts in the X-ray lab, Dr. Jim Britten and Victoria Jarvis. They are wonderful at what they do, diligent and supportive. I relied on their generous help to carry out each set of NMR experiments successfully. In addition, I would like to thank our former postdoctoral fellow, Dr. Hikaru Takeda, and my colleagues in the department, Jesse Hall and Tim Munsie, who were always ready to help when I found myself stressed out with the physically demanding tasks in the lab.

I have learned a tremendous amount from my mentor, Prof. Stephen Julian, about how to enjoy scientific research and how to become a true scholar. Stephen led me into the fascinating world of condensed matter physics by offering me the opportunity to work with him as an undergraduate research assistant. Since then, he has inspired me greatly with his deep physical intuition, passion for both research and teaching and impressive professionalism. Moreover, he has taught me, through the example he sets, to treat scientific research as a journey of intellectual satisfaction and self-improvement. During my graduate study at McMaster, Stephen continues to be a great source of wisdom and encouragement. Whenever I feel stuck, he magically gets me going again with tea and a delightful chat. With his boundless patience, understanding and kindness, Stephen has made a real difference in shaping my academic career, for which I will forever be in his debt.

Many thanks to my great friends from University of Toronto, in particular: Fazel Fallah Tafti, Wenlong Wu, William Witczak-Krempa, Frank Zhao, Deepak Chandan, Eric Lee, Robert Schaffer, Tyler Dodds, Jeff Rau, Subhro Bhattacharjee, Vijay Venkataraman and Kyusung Hwang, who remain close and supportive no matter where we are and what we do.

Most of all I thank my family for their unconditional love and trust. I am especially grateful to my mother, who has taught me to be true to myself and to stand firmly in my beliefs. She fully understands my enthusiasm for academic research and has supported me at every step. It is to her that I dedicate my thesis.

Mingxuan Fu

Contents

List of Figures

List of Tables

Chapter 1

Introduction

Condensed matter systems comprise a large number of strongly interacting particles such as electrons. Although the behaviors of the constituent particles are well understood, the system may surprise us with an exotic ground state that captures remarkable collective phenomena. One such novel state is a quantum spin liquid (QSL). This chapter introduces the QSL concept and presents an overview of the search for QSLs in two- and three-dimensional spin systems.

1.1 What is a QSL?

Before describing the exotic properties of a QSL, we first consider a bipartite lattice of spins with only nearest-neighbor exchange interaction J, as illustrated in Figure 1.1. This system can be described by the Heisenberg model:

$$H = -\sum_{(i,j)} J S_i \cdot S_j . \tag{1.1}$$

In this expression, J represents the exchange interaction between the i^{th} and j^{th} spins. Below a certain critical temperature, T_c, the system undergoes a magnetic phase transition to a ferromagnetic state in which all the spins align in the same direction $(J > 0)$, or to an antiferromagnetic state in which the spins arrange themselves in an alternating up-down pattern $(J < 0)$. In both cases, the spins freeze into a fixed configuration and the spin rotational symmetry is broken. A particularly interesting exception to this behavior is the QSL state [1-4]. Owing to robust quantum fluctuations, the strongly interacting spins in the QSL overcome the tendency to develop a static, long-range magnetic order even at the lowest temperature, thereby leading to a paramagnetic ground state without breaking the symmetry.

The basic building block for quantum paramagnetic states is the valence bond, which consists of two antiferromagnetically coupled spins that form a singlet, as shown in Figure 1.2. The constituent spins of the valence bond are maximally entangled, and therefore, the valence bond is considered a genuinely quantum object, with no classical counterpart. If every spin in a system is part of the valence bonds, then the ground state possesses a total spin of S = 0 and is nonmagnetic. One way to achieve such a ground state is to generate specific patterns of valence bonds, in which each spin is entangled only with its valence-bond partner. The resulting ground state is known as a valence bond solid (VBS) state, which typically breaks the translational symmetry of the lattice [1, 4]. However, the representation of the QSL state is far more complicated than that of the VBS. By analogy to flowing water, for which a still photograph is unable to capture its rich dynamics, a QSL state incorporates strong quantum spin fluctuations among the valence bonds, which lead to an infinite variety of valence-bond arrangements. Therefore, its representation features a superposition of all the possible valence bond configurations, known as the resonating valence bond (RVB) picture [5] (see Figure 1.2). In contrast to any single arrangement of the valence bond that breaks the translation symmetry, this RVB state preserves all of the conventional symmetries of the system.

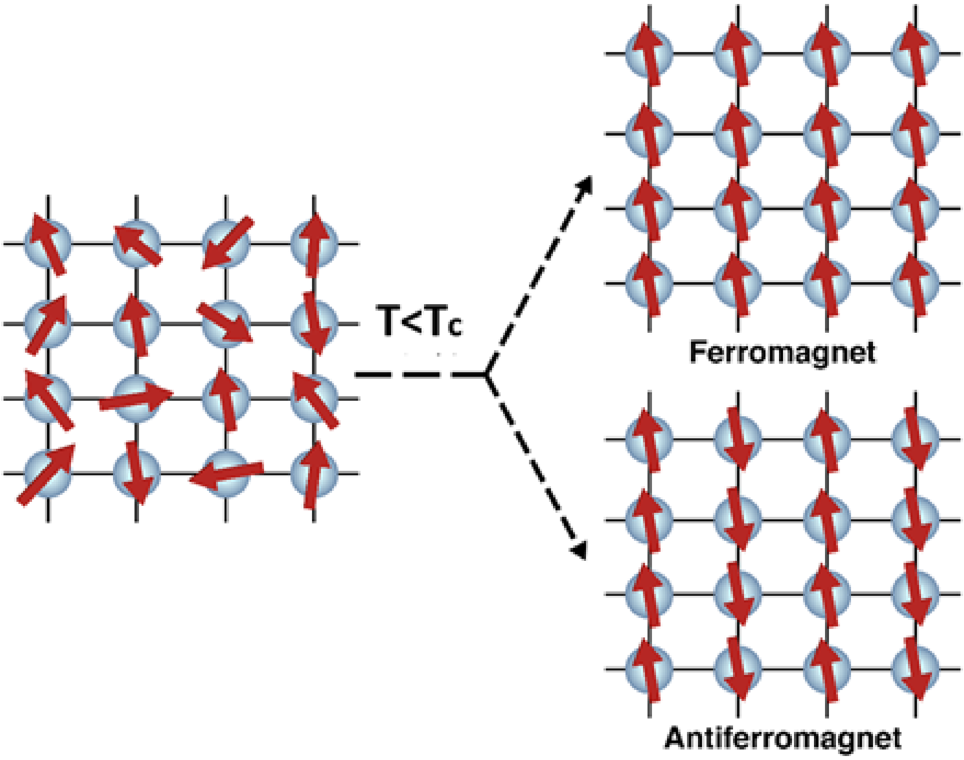

Figure 1.1. Schematic diagram of bipartite lattice of spins with only nearest-neighbor interaction J. Below a critical temperature T_c, the spin system develops a long-range magnetic order, forming either a ferromagnetic or antiferromagnetic state.

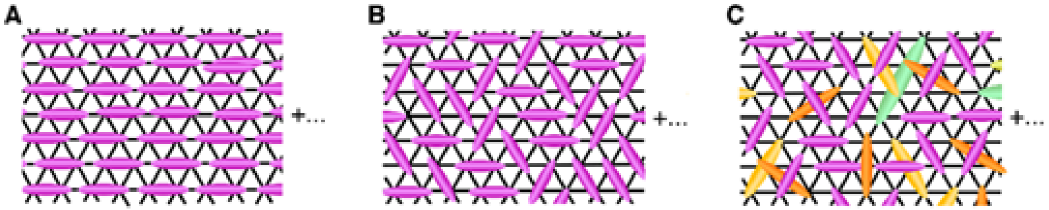

Figure 1.2. Schematic diagram of resonating valence bond (RVB) state that comprises all possible valence bond arrangements. **(A)** and **(B)** represent two possible short-range RVB states, which consist of valence bonds that are formed only by nearest-neighboring spins. **(C)** A long-range RVB state that contains valence bond formed by randomly distributed spins.

The RVB states can be divided into two broad classes: a short-range RVB and long-range RVB [6]. The distinct properties of these RVB states stem from the different weights of valence-bond arrangements in the superposition. In a short-range RVB state, the valence bonds are mainly formed by nearby spins (Figure 1.2A and 1.2B). The limited length scale of the valence bonds results in the exponential decay of the spin-spin correlation function. A predominant feature of the short-range RVB state is a finite spin gap that reflects the absence of low-energy excitations [8]. In contrast, the valence bonds in the long-range RVB may comprise spins that are randomly dispersed (Figure 1.2C). Owing to the lack of a fundamental length scale, the correlation function of the long-range RVB state decays algebraically. This state is also known as a gapless critical QSL, which features a large number of low-energy spin excitations [9-12].

As a highly entangled quantum state, the QSL provides excellent grounds for discovering fascinating collective phenomena. For instance, a QSL state supports elementary excitations with fractional quantum statistics known as spinons. In sharp contrast to the $S = 1$ spin-wave excitations commonly observed in ordered states, spinons behave as charge-neutral $S = 1/2$ particles and are accompanied by an emergent gauge field [1-4, 7].

A well-understood example of the QSL is a one-dimensional (1D) antiferromagnetic spin chain, in which each site along the chain is occupied by one localized electron with spin $S = 1/2$, as illustrated in Figure 1.3A. The exact ground state of the 1D spin chain is represented by a superposition of valence bonds that are not limited to nearest-neighbor pairing [13]. The spinon excitation is created by breaking a valence bond into two unpaired spins. The resulting deconfined spinons act as mobile domain boundaries that disrupt the long-range antiferromagnetic order. They can propagate across the lattice by locally rearranging the valence bond configurations, whereas the electrons themselves cannot move freely, as a result of the strong electron–electron interaction [14, 15]. We should note that the breaking of a valence bond always generates two spinons simultaneously, thereby causing a continuum in the spin excitation spectrum, as shown in Figure 1.3B. Such a spinon continuum has been observed in the 1D compound $KCuF_3$ using neutron scattering [16].

1.2 Searching for QSLs in Higher Dimensions

Although the QSL behavior has been demonstrated in the 1D antiferromagnetic spin chain, identification of QSLs in higher dimensions is still elusive. In Table 1.1, we compare the energies of the antiferromagnetically ordered state (for classical spins) and the valence bond state in a 1D chain, two-dimensional (2D) square lattice and three-dimensional (3D) cubic lattice [17]. According to the mean-field calculation, the ordered state gives an energy of $-zJS^2/2$ per spin, where z represents the number of nearest-neighbors. In the valence bond state, the energy of each singlet pair is given by $J\hat{S}_1 \cdot \hat{S}_2 = J(S^2 - S_1^2 - S_2^2)/2$ where $S = S_1 + S_2 = 0$. Therefore, each spin has an energy of $-JS(S+1)/2$, which is independent of z. For a 1D chain of S=1/2, the energy per spin is $-3J/8$ in the valence bond state, which is considerably lower than the value of $-J/4$ provided by the ordered state. In fact, we know from the Mermin-Wagner theory [18] that the ordered state will be avoided because of strong quantum fluctuations for any spin number S in a 1D system, thereby stabilizing the QSL as the true ground state. In 2D systems, the valence bond state may compete strongly against magnetic ordering, whereas in 3D systems, the ordinary ordered state becomes more energetically favorable [7].

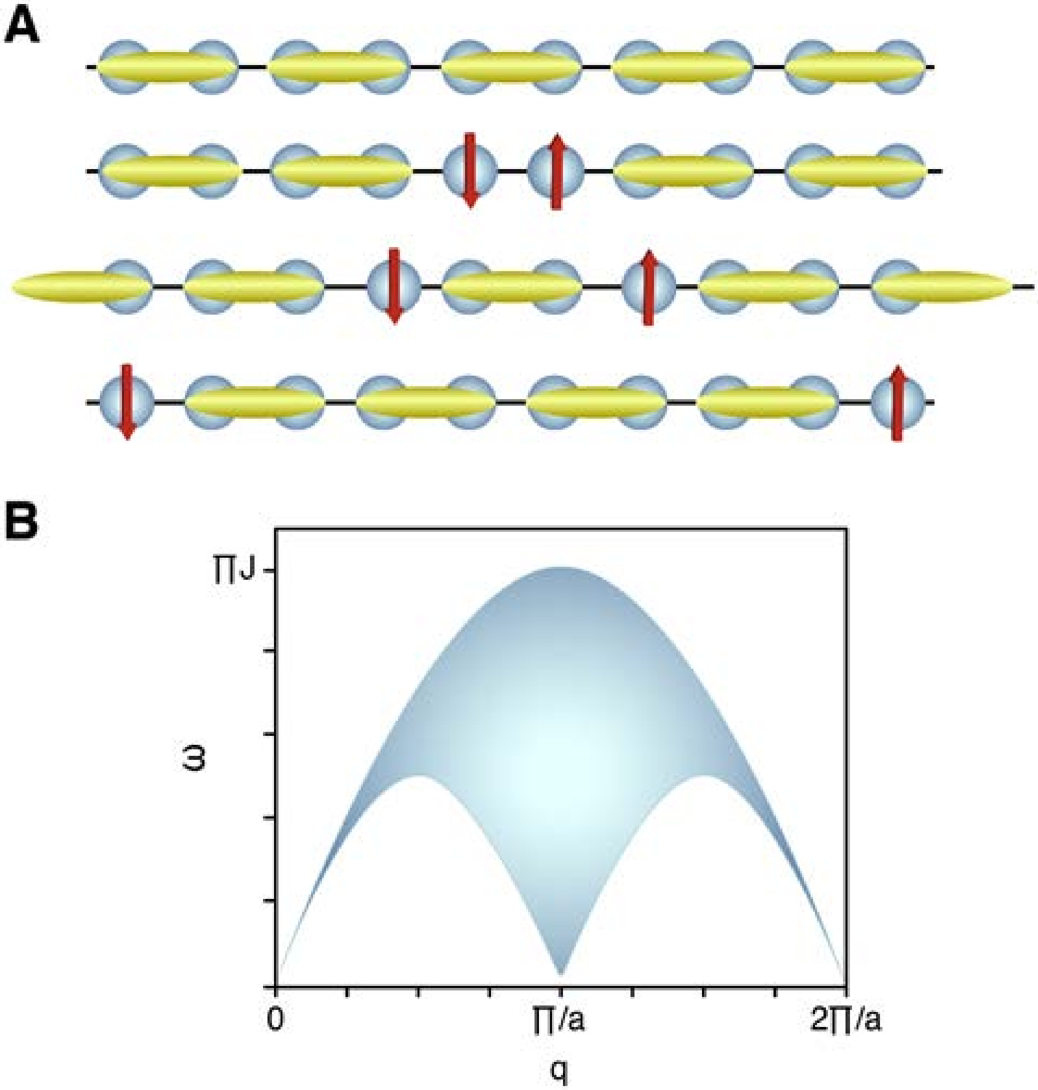

Figure 1.3. The QSL behavior of S = 1/2 antiferromagnetic spin chain. **(A)** The deconfined spinon is generated by breaking a valence bond (yellow ellipse) into two unpaired spins (red arrows). **(B)** The two-spinon excitation induces a continuum (filled area) in the spin excitation spectrum.

Table 1.1. Energies of antiferromagnetically ordered state and valence bond state in 1D chain, 2D square lattice, and 3D simple cubic lattice [17].

Dimensions	***z***	**Ordered state**	**Valence bond state**
1D chain	2	$-JS^2$	$-JS(S+1)/2$
2D square lattice	4	$-2JS^2$	$-JS(S+1)/2$
3D cubic lattice	6	$-3JS^2$	$-JS(S+1)/2$

In higher dimensions, a QSL state is most likely to be realized in a spin system that involves strong geometrical frustration. Geometrical frustration refers to the presence of competing magnetic interactions that result from the geometry of the lattice. The prototype of geometrical frustration is provided by a 2D triangular lattice of antiferromagnetically coupled Ising spins that orient either up or down along a single axis. The lowest possible energy is achieved when all three spins align anti-parallel to one another. However, as illustrated in Figure 1.4, once two of the spins form a singlet pair (i.e. an up-down configuration), the third spin is left over, as it cannot minimize the exchange energies with both its neighbors simultaneously. As a result, the spins strongly fluctuate, leading to a highly degenerate classical ground state manifold [19].

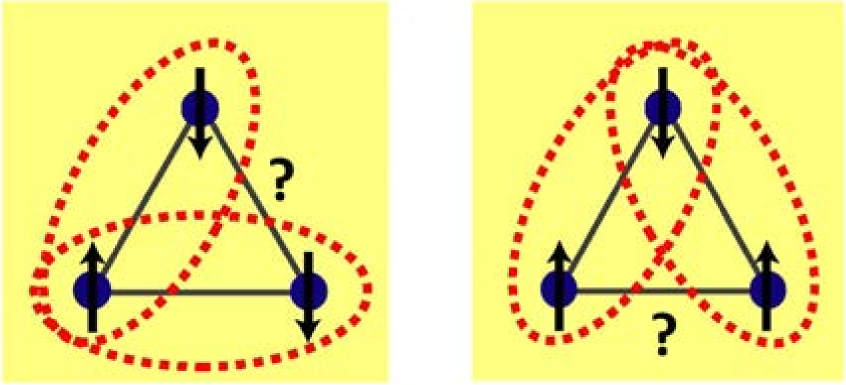

Figure 1.4. The simplest example of geometrical frustration – triangular lattice of antiferromagnetically coupled Ising spins, which points either up or down. The energies of the three bonds cannot be simultaneously minimized, leading to a large degeneracy of the classical ground states.

A key experimental signature of frustration is revealed by the temperature dependence of the magnetic susceptibility χ. At high temperatures, the χ of an antiferromagnet generally exhibits the Curie–Weiss behavior $\chi \propto 1/(T-\theta_{CW})$. The Curie–Weiss temperature θ_{CW} is negative for an antiferromagnet, and its magnitude $|\theta_{CW}|$ characterizes the strength of the magnetic interactions. In an unfrustrated material, the magnetic ordering typically occurs at a Néel temperature $T_N \approx |\theta_{CW}|$. In contrast, a geometrically frustrated system features a paramagnetic phase that persists for temperatures well below $|\theta_{CW}|$, where its susceptibility continues to follow the Curie–Weiss behavior. Such a state is called the cooperative paramagnet or classical spin liquid [1, 19]. At a lower temperature T_c , the frustrated system may develop a long-range magnetic ordering or spin freezing. Accordingly, a large value for the frustration parameter $f = |\theta_{CW}|/T_c \gg 1$ reflects a high degree of frustration [20].

We should note that the cooperative paramagnet realized in the temperature region $T_c < T < |\theta_{CW}|$ is fundamentally different from the QSL state, as it lacks the long-range entanglement, as well as coherent excitations like spinons. In addition to the frustration effect, a small spin number (i.e. S =1/2) is another crucial aspect for realizing a QSL in 2D or 3D spin systems. Large spins are mostly associated with classical fluctuations that are driven by thermal energy. When the thermal energy $k_B T$ vanishes at very low temperatures, the classical fluctuations cease. Consequently, the spin system may undergo a transition into a magnetically ordered state. In contrast, quantum fluctuation dominates for S=1/2 systems because the zero-point motion resulting from the uncertainty principle is comparable to the size of the spin itself. Such quantum fluctuation persist down to T = 0K, serving as the key ingredient of a QSL [1].

Three different classes of frustrated spin systems play prominent roles in the experimental quest for a QSL state: organic compounds featuring triangular lattices [21-23], kagomé antiferromagnets [24-30] and 3D pyrochlore antiferromagnets [31]. In the next section, we present a brief overview of kagomé antiferromagnets.

1.3 Kagomé Antiferromagnet

Among 2D spin systems, the S=1/2 Heisenberg antiferromagnet on a kagomé lattice (HKAF) is a prominent candidate for realizing the QSL ground state [1-4, 30]. A kagomé lattice comprises a network of corner-sharing triangles, as depicted in Figure 1.5B. This lattice structure resembles a particular type of Japanese basket weaving known as the kagomé pattern, and the lattice is named after it.

To demonstrate the high degree of frustration of the kagomé lattice, we compare its classical ground state with that of the edge-sharing triangular lattice, as shown in Figure 1.5. For a 2D triangular lattice with antiferromagnetically coupled spins, the classical ground state takes on a “120° structure”, in which the angle between any two neighboring spins is 120°. In this ground state, the vector summation of the three spins is zero. For the edge-sharing triangular lattice, when the orientation of spins 1 and 2 are fixed on one triangle, the orientation of the third spin is set, as shown in Figure 1.5C. Since every triangle shares two of the three spins with its neighbors, once the 120° pattern of the spins on any one triangle is specified, the orientation of all the other spins throughout the lattice can be uniquely determined (i.e., the direction of spin 4 must be identical to that of spin 1). However, this is not the case for the corner-sharing kagomé lattice. As shown in Figure 1.5D, with a fixed spin arrangement on the top triangle, spins 4 and 5 on the bottom triangle still possess the freedom to choose from two different orientations, both of which satisfy the 120° requirement. Therefore, the kagomé lattice has an infinite degeneracy of the ground state configurations, which highlights the vast potential of this system for hosting an exotic ground state.

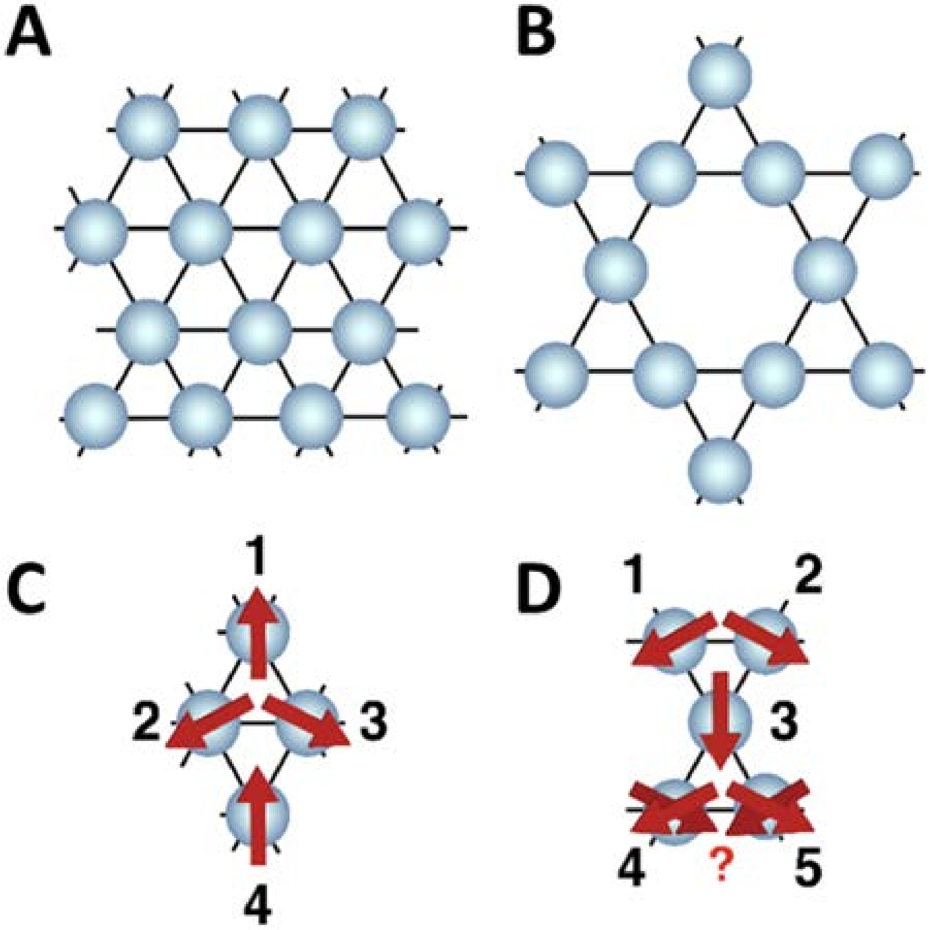

Figure 1.5. Comparison between edge-sharing triangular lattice **(A)** and corner-sharing kagomé lattice **(B)**. In the classical ground state of the triangular lattice shown in **(C)**, setting the 120° arrangement on any constituent triangle will select a unique spin configuration for the entire lattice. In the kagomé lattice, the 120° arrangement of the top triangle leaves two possible orientations for spin 4 and 5 of the bottom triangle, which give rise to an infinite degeneracy of the ground state.

Despite years of extensive theoretical studies, the nature of the ground state of the HKAF remains highly controversial. Currently, several competing theoretical proposals exist, including a fully gapped QSL [32-39], gapless critical QSL [11, 12, 40], and VBS state with a large unit cell [41-46]. Among these, the density-matrix renormalization group (DMRG) calculations predict a fully gapped QSL ground state [33, 34], whereas variational Monte Carlo (VMC) investigations indicate a gapless QSL with an extremely small energy difference compared to the gapped QSL state of the DMRG [46]. Moreover, recent studies have suggested that the nearest-neighbor HKAF may sit close to a quantum phase transition; consequently, its ground state may be changed from a QSL to a VBS by tuning the small next-nearest-neighbor interaction [36, 46-48], or to a long-range ordered state by tuning the Dzyaloshinsky-Moriya (DM) interaction [49-51]. Therefore, an experimental realization of the HKAF becomes all the more urgent to advance our understanding of its ground state properties.

The search for model materials for the S=1/2 KHAF has proven to be very challenging. Most candidates discovered over the last few decades feature distorted kagomé lattices, such as Vesignieite and Volborthite [25, 27, 30]; these materials also exhibit signatures involving a long-range magnetic order or spin freezing at low temperatures, which contradict the theoretically expected behavior of a QSL [26, 28, 30]. The successful synthesis of the structurally perfect S=1/2 kagomé lattice antiferromagnet $ZnCu_3(OH)_6Cl_2$ signifies an important breakthrough in the study of highly frustrated magnetism [2, 3, 24, 30]. In this thesis, we focus on presenting the results of ^{17}O single-crystal NMR studies of $ZnCu_3(OH)_6Cl_2$, as outlined in the next section.

1.4 Thesis Outline

The remainder of this thesis is organized as follows. Chapter 2 presents an introduction to the basics of NMR, helping readers to understand how NMR experiments work and how to interpret the results presented in later chapters. Chapter 3 begins with a brief review of the recent experimental progress on $ZnCu_3(OH)_6Cl_2$. A major challenge in establishing $ZnCu_3(OH)_6Cl_2$ as a QSL lies in the presence of defects, whose nature remains debatable. In the last section of Chapter 3, we summarize our ^{17}O Knight shift measurements, which were conducted in a magnetic field $B_{ext} = 9T$ along the c-axis. The results enabled us to conclusively determine the true identity of the defects. Chapter 4 presents our ^{17}O NMR data obtained with B_{ext} applied along the a*- axis. This field geometry allowed us to isolate the intrinsic magnetic behavior of the kagomé lattice from the defect contributions, thereby providing us with direct evidence for the realization of a gapped QSL ground state in $ZnCu_3(OH)_6Cl_2$. We then discuss the defect-induced phenomena in Chapter 5 and conclude our research in Chapter 6.

Chapter 2

The Basics of NMR

Various experimental techniques have been used in the search for QSL states. Among these, nuclear magnetic resonance (NMR) plays a very important role. In NMR studies, the behavior of atomic nuclei is manipulated and observed to obtain microscopic information about the electronic state of the studied material. The main strength of the NMR technique lies in its ability to distinguish the electronic properties arising from locally different environments. This chapter describes how NMR experiments are performed and how NMR data are interpreted. After introducing the basic resonance theory, we focus on the three key physical quantities measured in NMR: Knight shift K, quadrupole frequency ν_Q, and nuclear spin-lattice relaxation rate $1/T_1$. Details about the NMR theory discussed in this chapter have been well covered by Abragam [54] and Slichter [55].

2.1 Basic Resonance Theory

First, we consider the classical behavior of an isolated nucleus in an external magnetic field $\vec{B}_{ext}$ [54-56]. In a classical setting, a static magnetic field $\vec{B}_{ext} = B_{ext} \cdot \hat{z}$ exerts a torque $\vec{\tau}$ on the nuclear magnetic moment $\vec{\mu}$, namely,

$$\vec{\tau} = \vec{\mu} \times \vec{B}_{ext} . \tag{2.1}$$

While this torque $\vec{\tau}$ tends to align the nuclear magnetic moment $\vec{\mu}$ with the applied field $\vec{B}_{ext}$, $\vec{\mu}$ is accompanied by an angular momentum $\vec{I}$ that prevents such a rotation. Because $\vec{I}$ lies parallel to $\vec{\mu}$, as given by

$$\vec{\mu} = \gamma_N \cdot \vec{I} , \tag{2.2}$$

where γ_N is the nuclear gyromagnetic ratio, we obtain the equation of motion for $\vec{\mu}$ by equating the rate of change of $\vec{J}$ and torque $\vec{\tau}$ such that

$$\vec{\tau} = \frac{d\vec{I}}{dt} = \vec{\mu} \times \vec{B}_{ext} \tag{2.3a}$$

$$\frac{d\vec{\mu}}{dt} = \gamma_N \vec{\mu} \times \vec{B}_{ext} . \tag{2.3b}$$

This equation indicates that the change in $\vec{\mu}$ is perpendicular to both $\vec{\mu}$ and $\vec{B}_{ext}$. Therefore, as illustrated in Figure 2.1, the nuclear magnetic moment $\vec{\mu}$ undergoes a Larmor precession about $\vec{B}_{ext}$ with a fixed angle θ and thus acts as a spinning top. By solving the equation of motion for $\vec{\mu}$, we obtain the Larmor precession frequency

$$\omega_L = \gamma_N B_{ext} . \tag{2.4}$$

Turning to the quantum mechanical description [54, 55], the nuclear magnetic moment $\vec{\mu}$ interacts with the applied static field $\mathbf{B_{ext}} = B_{ext} \cdot \hat{\mathbf{z}}$ via the Zeeman interaction, which is expressed as follows:

$$H = -\vec{\mu} \cdot \mathbf{B_{ext}} = \gamma_N B_{ext} I_z \tag{2.5}$$

This interaction generates a ladder of 2I+1 discrete energy levels for the nuclear spin I with the following energy eigenvalues

$$E_m = -\gamma_N \hbar B_{ext} m \tag{2.6}$$

The Zeeman energy splitting for the ^{17}O nucleus, which has a nuclear spin $I = 5/2$, is depicted in Figure 2.2, which consists of five equally spaced energy levels with separation $\Delta E = \gamma_N \hbar B_{ext}$. In addition to the Zeeman interaction, for nuclear spin $I > 1/2$, the quadrupole interaction causes the energy levels to shift unequally, leading to five different transitions in a typical ^{17}O NMR lineshape. The effects of the quadrupole interaction are discussed in more detail in Section 2.4.

To observe NMR, we must stimulate the transitions between the nuclear energy levels by applying an oscillating magnetic field $\mathbf{B_1} = B_1 \cos(\omega_1 t) \cdot \hat{\mathbf{x}}$ that lies along a direction perpendicular to the static field $\mathrm{B_{ext}}$. The perturbation $H_1 = \gamma_N \hbar B_1 \cos(\omega_1 t) I_x$ generated by $\mathbf{B_1}$ possesses matrix elements proportional to $\langle m' | I_x | m \rangle$, which is zero unless $m' = m \pm 1$; accordingly, only transitions between adjacent energy levels may occur in the high field limit. The angular frequency ω required for activating such a transition is given by

$$\hbar\omega_L = \Delta E = \gamma_N \hbar B_{ext} \tag{2.7a}$$

or

$$\omega_L = \gamma_N B_{ext}. \tag{2.7b}$$

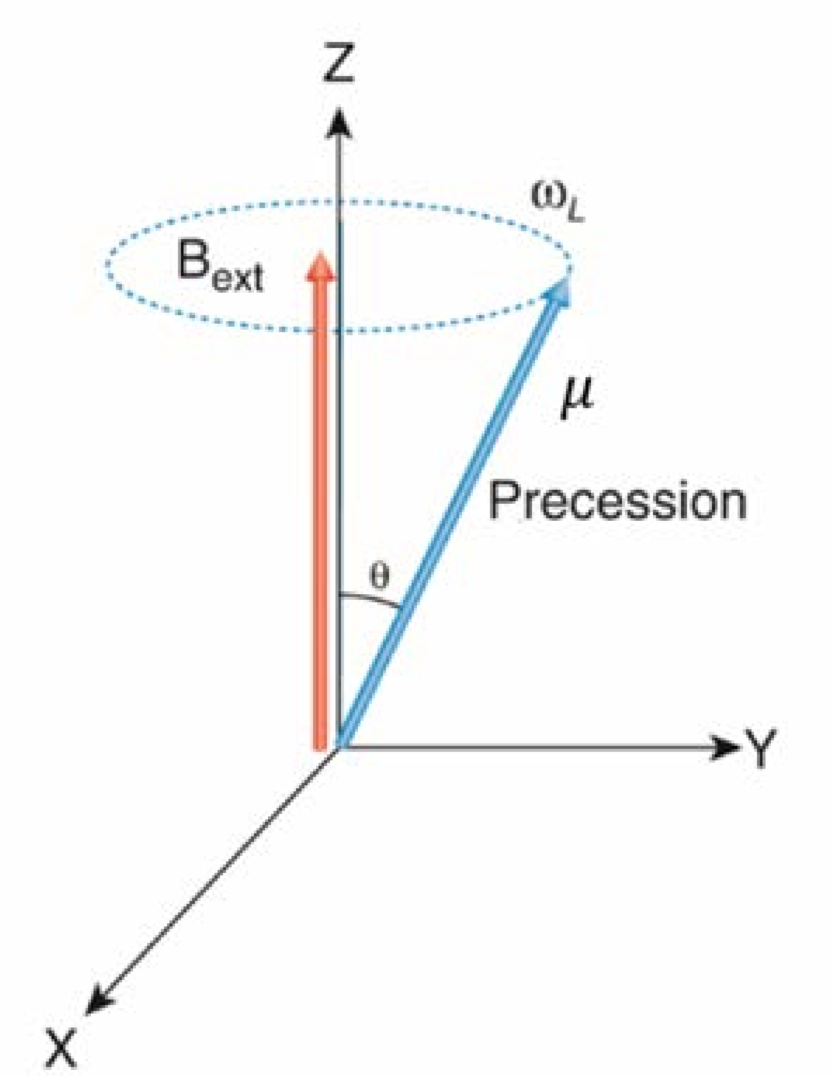

Figure 2.1. Schematic diagram of the classical Larmor precession of a magnetic moment $\vec{\mu}$ in a static magnetic field $\vec{B}_{ext}$.

The magnitude of $\gamma_N / 2\pi$ typically in the range of ~MHz/T, and the applied field is $B_{ext} \sim 10T$; therefore, the resonant frequency $f = \omega/2\pi$ typically lies in the radio- frequency (RF) range, and we apply RF pulses to produce $\mathbf{B_1}$ in NMR experiments. Table 2.1 presents the properties for a few commonly used nuclei in NMR studies, including the values of the nuclear spin, gyromagnetic ratio, and resonant frequency expected for $B_{ext} = 9T$. In practice, it is unnecessary to tune the RF pulse to exactly the expected resonant frequency $f_L = \gamma_N B_{ext} / 2\pi$. As long as the frequency of the applied RF pulse falls within a bandwidth of ~100 kHz around the expected resonant frequency, we can detect an NMR signal [61].

Interestingly, the Larmor precession frequency found in the classical treatment of an isolated magnetic moment is identical to the frequency required for inducing resonant absorption between quantized energy levels of a nucleus. This fact implies a close connection between the classical and the quantum mechanical descriptions. Although the Hamiltonian of the Zeeman interaction (Eq. 2.5) has a discrete set of energy eigenstates $\left|m\right\rangle$, the expectation value of the magnetic moment operator $\left\langle \boldsymbol{\mu} \right\rangle$ derived based on these eigenstates can be expressed as a continuum of magnitudes and orientations such that

$$\left\langle \mu_x \right\rangle = \frac{\gamma_N \hbar}{2} \sin\theta \cos\phi; \tag{2.8a}$$

$$\left\langle \mu_y \right\rangle = \frac{\gamma_N \hbar}{2} \sin\theta \sin\phi; \tag{2.8b}$$

$$\langle \mu_z \rangle = \frac{\gamma_N \hbar}{2} \cos\theta. \tag{2.8c}$$

Thus, the expectation value of the observable $\langle \boldsymbol{\mu} \rangle$ in quantum mechanics acts us a vector of length $\gamma_N \hbar / 2$, and can take any direction in space rather than being constrained to a few discrete orientations. This feature allows us to treat the nuclear magnetic moment μ as a classical vector in the description of NMR [55].

Table 2.1. Properties of the nuclei commonly used in NMR experiments

Atom	Spin I	$\gamma_N / 2\pi$ (MHz/T)	f_L (MHz, in $B_{ext} = 9\mathrm{T}$)
^{1}H	1/2	42.574	383.17
^{2}D	1	6.535	58.82
^{13}C	1/2	10.705	96.345
^{17}O	5/2	5.772	51.948
^{35}Cl	3/2	4.171	37.539
^{63}Cu	3/2	11.285	101.57
^{65}Cu	3/2	12.089	108.80

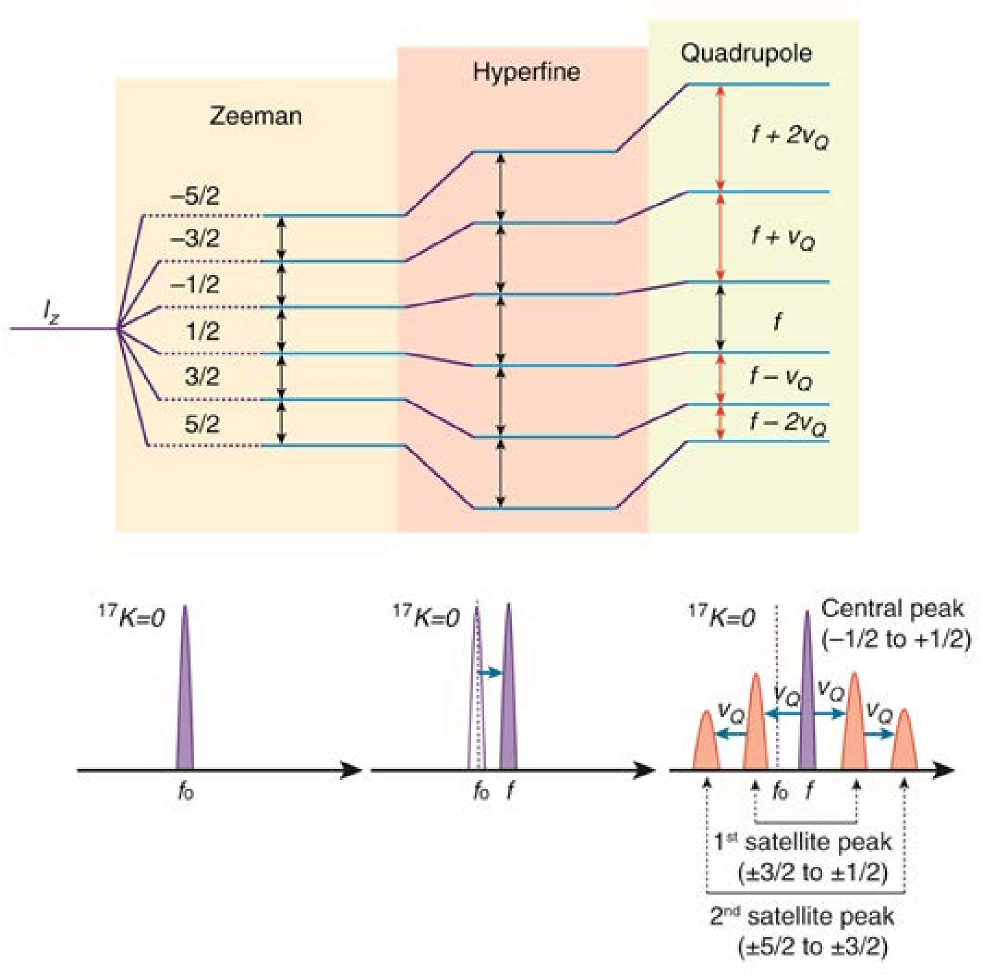

Figure 2.2. Schematic illustration of the modifications in Zeeman energy levels of I = 5/2 nuclei owing to the hyperfine and quadrupole interactions. The bottom panel presents the corresponding changes in the single-crystal NMR lineshape. The hyperfine interaction causes the central peak frequency f to shift from the resonant frequency of a bare nucleus $f_o = \gamma_N B_{ext}$. This shift is commonly known is NMR Knight shift, ^{17}K. The perturbation induced by the quadrupole interaction generates five NMR peaks in the lineshape. To a first-order approximation, the splitting between adjacent NMR peaks is given by the quadrupole frequency ν_Q.

Furthermore, it should be noted that the energy separation between adjacent levels is directly proportional to the applied field. In the absence of an RF excitation pulse, the nuclear spins distribute themselves among the different energy levels obeying the Boltzmann statistics [55, 60]. Accordingly, the population ratio of two adjacent energy states is given by

$$\frac{N_{m-1}}{N_m} = e^{-\Delta E/k_B T} = \mathrm{e}^{-\gamma_N B_{ext}/k_B T}\,. \tag{2.9}$$

As a result, more nuclear spins occupy the lower energy level N_m with increasing B_{ext}, and the difference in their population is the key to the observation of NMR signals. In fact, the NMR signal intensity $A \propto f^2$ (or, equivalently, $A \propto B_{ext}^2$), and therefore the application of a stronger B_{ext} improves the signal-to-noise ratio (S/N) in NMR experiments.

2.2 Spin Echo Method

In this section, we present the pulse sequence employed in NMR signal generation. In a reference frame rotating at the resonant frequency ω_L, a static magnetic field $\mathbf{B_{ext}} \parallel z$ leads to a net nuclear magnetization M_0 along the z-axis. To produce the NMR signal, we apply an RF pulse that generates an oscillating magnetic field $\mathbf{B_1} = B_1 \cos(\omega' t) \cdot \hat{\mathbf{x}}$ for a time duration t_{90} such that

$$\gamma_N B_1 t_{90} = \omega' t_{90} = \frac{\pi}{2}\,. \tag{2.10}$$

When ω' is sufficiently close to ω_L, the applied RF pulse rotates M_0 by 90° entirely into the *xy*-plane, as shown in Figure 2.3C. Accordingly, such an RF pulse is called a 90° degree or a $\pi/2$ pulse.

When the 90° pulse is switched off, the nuclear spins precess freely at ω_L within the *xy*-plane, thereby generating an induced voltage signal across the coil. This voltage signal decays as a function of time, known as the free induction decay (FID). The duration of the FID signal is limited by the following mechanisms: the interactions among the nuclear spins cause differences in the precession frequency; consequently, the net transverse magnetization M_{xy} declines as the nuclear spins fan out (*i.e.*, dephase), as shown in Figure 2.3C. This process is called the spin-spin relaxation, and it is characterized by a time constant T_2. In addition, the static field inhomogeneity ΔB_{ext} also contributes to the nuclear spin dephasing, while the corresponding dephasing time T_2^* is typically much longer than the intrinsic T_2 in our experiments.

To isolate the intrinsic spin-spin relaxation from the effect of the field inhomogeneity, we apply the spin echo pulse sequence depicted in Figure 2.3A. This pulse sequence consists of a 90° pulse and a subsequent 180° pulse ($t_{180} = 2t_{90}$) separated by a delay time τ. With a 180° pulse applied along the x-axis, the orientation of each dephased nuclear spin is inverted; now, the spins that precess slower than average take the lead. Consequently, all the spins realign along the -y axis at time 2τ (see Figure 2.3C), and the spin echo signal appears [54-56].

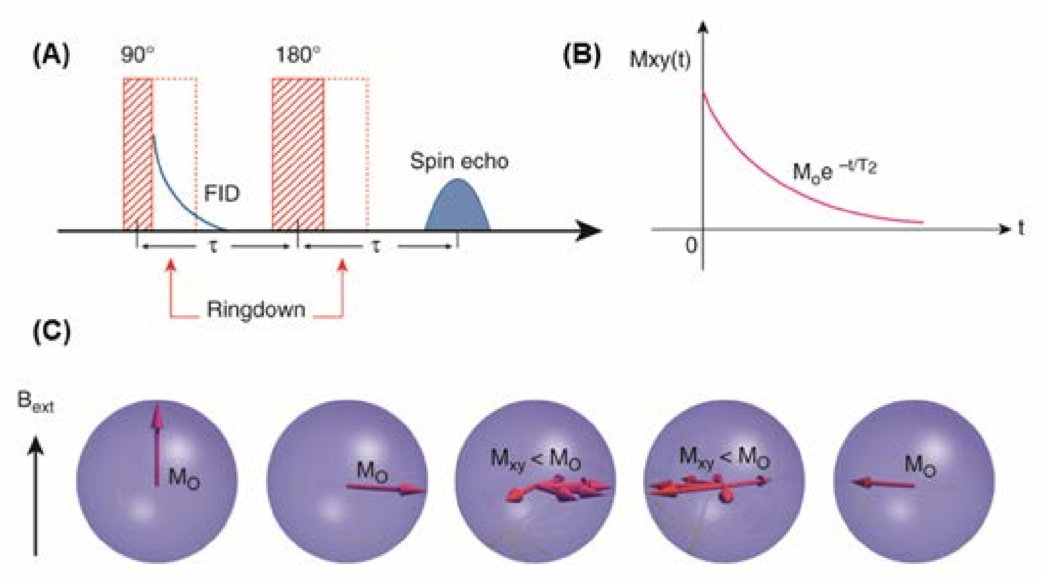

Figure 2.3. Schematic diagrams of the spin echo technique and spin-spin relaxation. **(A)** RF pulse sequence used for measuring the spin echo signal. The FID and spin echo signals are depicted as a function of time. **(B)** The exponential decay of the spin echo intensity owing to the spin-spin relaxation, which provides a measure of the spin-spin relaxation rate $1/T_2$. **(C)** A classical description of the behavior of the nuclear spins in response to the 90° and 180° pulses.

The echo intensity declines as τ increases. To measure the transverse relaxation time T_2, we apply a train of spin echo pulse sequences with varying τ values [56]. The decay of the echo intensity as a function of τ, provides us with information regarding the mechanism of the spin-spin relaxation as well as the magnitude of T_2. For example, the exponential decay of echo intensity shown in

Figure 2.3B indicates that the T_1 spin-lattice relaxation process (see Section 2.6) dominates the T_2 relaxation.

2.3 Knight Shift

In addition to the external static field $\mathbf{B_{ext}}$, nuclear spins in solids are affected by the hyperfine magnetic field $\mathbf{B_{hf}}$ generated by the electrons in their vicinity, which yields an effective field $\mathbf{B_{eff}} = \mathbf{B_{ext}} + \mathbf{B_{hf}}$ at the nuclear sites. As a result, the resonance frequency of the central transition shifts away from the resonant frequency of a bare nucleus $f_L = \gamma_N B_{ext} / 2\pi$ as

$$f_{NMR} = f_L(1+K) . \tag{2.11}$$

The fractional frequency shift *K*, commonly known as the NMR Knight shift, is defined as

$$K = (f_{NMR} - f_L) / f_L , \tag{2.12}$$

and is conventionally expressed as a percentage of the Larmor frequency f_L (see Figure 2.2). The Knight shift *K* consists of two terms: electron spin shift K_{spin} and chemical shift K_{chem}, so that $K = K_{spin} + K_{chem}$.

The electron spin shift K_{spin} is directly proportional to the local electronic spin susceptibility χ_{spin} in the vicinity of the observed nuclear sites such that

$$K_{spin} = \frac{A_{hf}}{N_A \mu_B} \cdot \chi_{spin} , \tag{2.13}$$

where A_{hf} is the hyperfine coupling constant between the nuclear spins and the nearby electron spins polarized by the external magnetic field $\mathbf{B_{ext}}$. The electronic spin susceptibility χ_{spin} (in units of emu/mol) is often temperature dependent in strongly correlated electron systems. By tracking the temperature dependence of K_{spin}, we can gain insights into the site-specific behavior of χ_{spin}.

The chemical shift K_{chem} is associated with two types of magnetic susceptibilities: the orbital (Van Vleck) paramagnetic susceptibility χ_{orb} and the diamagnetic susceptibility χ_{dia} [54, 55]. The orbital susceptibility χ_{orb} stems from the mixing of electron orbitals in the presence of a magnetic field. When a magnetic ion sits in a particular crystal structure, the surrounding charge distribution generates a crystal field at the ion site, which lifts the degeneracy of its electron orbital states. The energy separation among split orbitals is governed by the symmetry of the local environment. Once an external magnetic field is applied, these electron orbitals are no longer the eigenstates, and consequently, they rearrange themselves through a process called hybridization (*i.e.*, mixing of electron orbitals). From the second-order perturbation theory, the orbital susceptibility χ_{orb} is given by

$$\chi_{orb}^{z} \propto \sum_{n} \left| \langle 0 | L_z | n \rangle \right|^2 \Big/ (E_n - E_0)\,, \tag{2.14}$$

where $|0\rangle$ represents the ground state of the system, and the summation is take over all the allowed excited states $|n\rangle$. In the transition metal systems of our interest, the magnitude of the crystal field splitting $E_n - E_0$ is approximately 1eV = 11,600K, which is much larger than our experimental temperature of ~300 K. Thus, χ_{orb} may be considered independent of temperature [57-59].

The diamagnetic susceptibility χ_{dia} arises from the diamagnetic shielding current induced by the orbital motion of inner core electrons, and it is purely a quantum mechanical effect. χ_{dia} is also independent of temperature [57-59]. Therefore, the chemical shift K_{chem} is a temperature-independent term, and the temperature variation of the Knight shift is dominated by the electronic spin susceptibility χ_{spin}. Accordingly, we can write the hyperfine coupling constant A_{hf} as

$$A_{hf} = N_A \mu_B \cdot \frac{\Delta K}{\Delta \chi}, \tag{2.15}$$

where χ is the uniform magnetic susceptibility; N_A, the Avogadro constant; and μ_B, the Bohr magneton. By plotting K as a function of the bulk-averaged susceptibility χ_{bulk} with temperature being the implicit parameter, we can obtain the value of A_{hf} from the slope of the linear relation [62].

2.4 Hyperfine Interaction

The hyperfine coupling A_{hf} quantifies the strength of the local hyperfine magnetic field B_{hf} generated by electrons surrounding a nucleus. In principle, A_{hf} is a tensor quantity; nonetheless, for simplicity, we often treat it as a scalar. In NMR studies, we commonly express A_{hf} in units of kOe/μ_B, which corresponds to the strength of the magnetic field (kOe) at the nuclear site induced by one Bohr magneton (μ_B) of the electron spin susceptibility χ_{spin}. This method of specifying A_{hf} is advantageous as it considers A_{hf} a property of the local electronic environment that is independent of the nuclear spin involved as an experimental probe.

For a magnetic ion such as Cu^{2+}, the hyperfine interaction generally results from the onsite electrons, which couple with the nuclear spins via two main types of interactions—Fermi contact and dipole-dipole interaction [62-64]. The Fermi contact interaction takes the form

$$H_{contact} = \frac{8\pi}{3}\gamma_e\gamma_N\hbar^2 I \cdot S\delta(\boldsymbol{r}), \tag{2.16}$$

where S is the electron spin operator; γ_e, the gyromagnetic ratio of an electron; and $\boldsymbol{r}$, the position vector of an electron relative to the nuclear site ($\boldsymbol{r} = 0$). Only unpaired s-electrons that possess finite probability density at the nucleus may be directly involved in this interaction. Owing to the spherical symmetric probability distribution of the s-electron orbitals, the Fermi contact interaction produces an isotropic contribution to K_{spin}.

Although the non-s-electrons do not generate the contact interaction directly owing to their vanishing probability density at the nucleus, they may cause an unbalance in the spin density of the paired inner s-electrons via direct exchange interactions. The resulting finite spin polarization in the s-orbitals will, in turn, give rise to a Fermi contact interaction with nuclear spin. This process is called inner core polarization. For instance, when the unpaired 3d-electron spins in Cu^{2+} ions are polarized by an external magnetic field, they induce a net spin polarization in the inner s-orbitals that aligns anti-parallel to the applied field; consequently, the resulting contact interaction contributes a negative isotropic term to K_{spin}. In fact, the core polarization effect in transition metal ions typically generates a negative contact interaction.

The dipole-dipole interaction between a nuclear spin *I* and an electron spin *S* is expressed as

$$H_{dip-dip} = \frac{\gamma_e \gamma_N \hbar^2}{r^3}[3\frac{(\mathbf{I}\cdot\mathbf{S})(\mathbf{S}\cdot\mathbf{I})}{r^2} - \mathbf{I}\cdot\mathbf{S}]. \qquad (2.17).$$

As a dipole field averages to zero over the spherical surface of the s-electron orbitals, this interaction appears only for non-s electrons. Such a dipolar hyperfine field is anisotropic; therefore, the sign and magnitude of the resulting K_{spin} varies with the direction of the applied magnetic field. For a partially filled p-orbital, K_{spin} generated by the dipolar hyperfine interaction is given by [54, 63]

$$K^{\parallel}_{spin} = \frac{4}{5}\left\langle \frac{1}{r^3} \right\rangle \chi_{spin} \qquad (2.18a)$$

$$K^{\perp}_{spin} = -\frac{2}{5}\left\langle \frac{1}{r^3} \right\rangle \chi_{spin}, \qquad (2.18b)$$

where "$\parallel$" and "$\perp$" indicate the direction of the applied field with respect to the lobe of the p-orbital, χ_{spin} is proportional to the polarization of 2p electrons and

$\left\langle \frac{1}{r^3} \right\rangle$ is the average radial electron distribution. The magnitude of $\left\langle \frac{1}{r^3} \right\rangle$ often determined through electron spin resonance (ESR) experiments.

In the case of a non-magnetic ion, the hyperfine magnetic field at its nucleus originates from the transferred hyperfine interaction. Such an interaction allows us to probe the spin susceptibility of the Cu^{2+} electrons in $ZnCu_3(OH)_6Cl_2$ using the ^{17}O Knight shift. Once the Cu^{2+} electrons are polarized by an external magnetic field, this polarization can be transferred to the O^{2-} electrons surrounding the Cu^{2+} site through hybridization between Cu^{2+} and O^{2-} orbitals. The induced polarization of O^{2-} electrons then exerts the hyperfine field on its nucleus via the aforementioned mechanisms.

The wave-vector-dependent hyperfine form factor $A_{hf}(\mathbf{q})$ arises from the geometric effects of the local hyperfine interactions, and it is defined as [65]

$$A_{hf}(\mathbf{q}) = \sum_i A_{hf}^i e^{-i\mathbf{q}\cdot\mathbf{r}_i}, \tag{2.19}$$

where A_{hf}^i represents the hyperfine interaction of the observed nuclear spin with the electron spin *i* in its vicinity, and $\boldsymbol{r}_i$ is the position vector of the electron spin *i* relative to the nucleus. As discussed in Section 2.6, $A_{hf}(\mathbf{q})$ is incorporated into the expression of the nuclear spin-lattice relaxation rate $1/T_1$, and it governs which *q*-component of the electron spin fluctuations $1/T_1$ is sensitive to [66].

2.5 Nuclear Quadrupole Interaction

In addition to the magnetic hyperfine interactions, the nucleus also couples to the local charge environment through its quadrupole moment Q via the so-called nuclear quadrupole interaction. The strength of this interaction is represented by the quadrupole frequency ν_Q, which is directly related to the second derivative of the total Coulomb potential at each nuclear site. Thus, the quadrupole interaction is an effective probe of the local lattice distortion close to the observed nuclear site.

The nuclear quadrupole moment is derived from the multipole expansion of the nuclear charge distribution in spherical harmonics of order l. The first term in this expansion is the charge monopole moment (l = 0), Ze, which treats the nucleus as a point charge. However, the monopole interaction is independent of the orientation of nuclear spins, and therefore, it does not affect the transitions among different nuclear spin states. The next moment, the electric dipole moment (l = 1) is forbidden owing to the definite parity of the nuclear states. In fact, such a well-defined parity prohibits any charge multipoles with odd l.

The quadrupole moment Q (l = 2) is allowed, and it is defined as [54, 55]

$$Q = \frac{1}{2e}\int (3\mathrm{z}^2 - \mathrm{r}^2)\rho(\vec{r})d\vec{r}\,, \tag{2.20}$$

where $\rho(\vec{r})$ represents the charge density distribution of the nucleus in its highest magnetic eigenstate $I = I_z$, and $e = |e|$ is the electron charge. The sign and magnitude of the quadrupole moment Q depends on the nature of the nuclear charge distribution $\rho(\vec{r})$. Suppose that we have a perfectly spherical $\rho(\vec{r})$; then, Q becomes zero. A finite Q reflects the deviation of $\rho(\vec{r})$ from spherical symmetry; a charge distribution $\rho(\vec{r})$ that is elongated along the z-axis will lead to a positive quadrupole moment, whereas a charge distribution that is flattened within the *xy*-plane will provide a negative quadrupole moment. Moreover, nuclei with spin $I = 1/2$ do not experience nuclear quadrupole interaction (*i.e.*, Q = 0) because flipping between the $I = \pm 1/2$ states does not alter the total electrostatic energy of the nucleus.

Higher-order moments of the charge distribution do exist. However, the effect of these interactions is expected to be negligibly small because the decay of the interaction strength follows [54]

$$(\frac{R_n}{R_e})^l \approx (10^{-5})^l \, , \tag{2.21}$$

where R_n and R_e are the radius of the nucleus and electronic charge distribution, respectively. To illustrate this very rapid decrease in the interaction strength with increasing l, we compare the magnitude of the l = 0 monopole and l = 2 quadrupole interactions; the monopole interaction is of the order of 10 eV, whereas a typical quadrupole interaction is of the order of 10 MHz to 10^{-8} eV, which is about ten orders of magnitude weaker.

The Hamiltonian of the nuclear quadrupole interaction takes the form [54, 55]

$$H_Q = \frac{e^2qQ}{4I(2I-1)}[3I_z^2 - I(I+1) + \frac{1}{2}\eta(I_+^2 + I_-^2)], \tag{2.22}$$

and the z-axis component of the quadrupole interaction tensor is expressed as

$$\nu_Q^z = \frac{3e^2q_z}{2hI(I+1)}Q. \tag{2.23}$$

In these expressions, $eq = \partial^2 V / \partial z^2 = V_{zz}$ is the electric field gradient (EFG) along the principle z-axis of the quadrupole interaction tensor, and V is the electric potential. The asymmetry parameter is defined as

$$\eta = \left|\frac{V_{xx} - V_{yy}}{V_{zz}}\right| = \left|\frac{\nu_Q^x - \nu_Q^y}{\nu_Q^z}\right|. \tag{2.24}$$

According to the Laplace equation for the electrostatic potential *V*, the EFG along the three principle axes of the quadrupole interaction tensor should sum to zero such that

$$\frac{\partial^2 V}{\partial x^2} + \frac{\partial^2 V}{\partial y^2} + \frac{\partial^2 V}{\partial z^2} = 0. \tag{2.25}$$

This relation indicates that the three principle components of the quadrupole interaction will also add up to zero as

$$\nu_Q^x + \nu_Q^y + \nu_Q^z = 0. \tag{2.26}$$

When EFG possess axial symmetry, as is the case with the tetragonal crystal structure, $\eta = 0$ and $\nu_Q^x = \nu_Q^y = -\nu_Q^z/2$.

As shown in Figure 2.2, the quadrupole interaction shifts the nuclear energy levels, leading to different energies for each nuclear transition. For the single-crystal NMR lineshape of ^{17}O, the Zeeman transition splits into five resonant peaks owing to the quadrupole interaction. The separation between two adjacent peaks is equal to the value of the quadrupole frequency ν_Q^α, where α indicates the direction of the applied field. Note that since ν_Q^α is typically anisotropic, the value of ν_Q^α varies with the orientation of the applied field. In the high field limit, the quadrupole interaction is substantially weaker than the magnetic Zeeman interaction, and therefore, it can be treated as a perturbation to the Zeeman Hamiltonian. Then, the effect of the quadrupole interaction on the nuclear energy levels can be easily quantified based on the perturbation theory [54].

2.6 Spin-lattice Relaxation Rate *$1/T_1$*

While the NMR Knight shift probes the static and uniform (q = 0) magnetic properties of the studied material, the dynamical magnetic properties are revealed by the nuclear spin-lattice relaxation rate $1/T_1$. $1/T_1$ characterizes the rate at which the nuclear spin system returns to the thermal equilibrium after being perturbed by RF pulses. Figure 2.4 depicts the process of a T_1 measurement using the inversion-recovery pulse sequence. In such a pulse sequence, we first apply a π pulse at the resonant frequency f_{NMR} to invert the population of the nuclear spin system. Once this π pulse is turned off, the nuclear spins tend to release the excess energy $(\hbar\omega_{NMR})$ to the lattice to recover the equilibrium distribution. After a delay time t, we collect the spin echo signal using the spin echo pulse sequence. By tracking the integrated echo intensity as a function of the delay time t, we obtain the recovery curve of the nuclear magnetization $M(t)$ to its equilibrium value M_0. We can then determine the value of $1/T_1$ by fitting $M(t)$ to the standard recovery form [67, 68]:

$$M(t) = M_0 - A\sum_{j=1}^{2I} a_j e^{-(\frac{b_j t}{T_1})} . \tag{2.27}$$

This fitting formula involves three free parameters: M_0, A, and $1/T_1$. By solving the coupled rate equations for a particular nuclear spin I, we can obtain the values of coefficients a_j and b_j for each NMR transition (see Appendix A for a detailed calculation of $I=5/2$ relaxation curves).

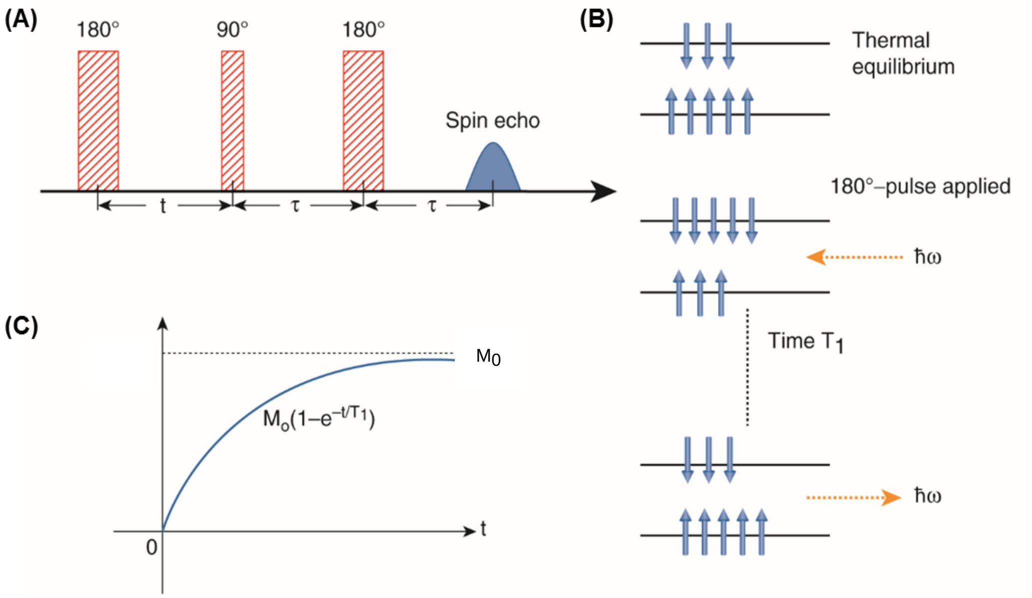

Figure 2.4. Schematic diagram of a T_1 measurement. **(A)** The inversion-recovery pulse sequence. **(B)** The 180° pulse inverts the nuclear spin population between two

adjacent energy levels. Following the 180° pulse, the nuclear spin system returns to the equilibrium distribution via the T_1 relaxation process, which involves the loss of energy $\hbar\omega$ by the nuclear spin system. **(C)** The exponential recovery of the nuclear magnetization as a function of the delay time *t*; the recovery process is characterized by the nuclear spin-lattice relaxation rate $1/T_1$.

Since the NMR frequency is rather low ($\hbar\omega_{NMR}/k_B \approx 1mK$), the lattice absorbs the lost energy of the nuclear spin system through low-energy excitations. Therefore, T_1 probes the low-energy regime of the spin-fluctuation spectrum at ω_{NMR} or the slow spin dynamics. The larger the amount of low-energy excitations present in the lattice, the faster T_1 will be. Assuming that the electron-nuclear spin interaction is the dominant T_1 relaxation mechanism, $1/T_1$ is related to the dynamical structure factor $S(\mathbf{q},\omega)$ as [66]

$$\frac{1}{T_1} = \frac{\gamma_N^2 \hbar}{2\mu_B^2} \sum_q \left(\left| A(\mathbf{q})_{\perp,1} \right|^2 + \left| A(\mathbf{q})_{\perp,2} \right|^2 \right) S(\mathbf{q},\omega_{NMR}), \tag{2.28}$$

where ω_{NMR} is the NMR frequency, and the **q**-summation is taken within the first Brillouin zone. The wave-vector-dependent hyperfine form factor $A(\mathbf{q})_\perp$ is perpendicular to the applied magnetic field. For example, with a magnetic field along the z-axis, the form factor $A(\mathbf{q})_x$ and $A(\mathbf{q})_y$ along the x- and y-axis, respectively, will contribute to $1/T_1$. Moreover, the **q**-dependence of the form factor

$A(\mathbf{q})$ may vary among different nuclear sites, which may result in the distinct temperature dependence of $1/T_1$ for different nuclei in the same compound [64].

The dynamical structure factor $S(\mathbf{q},\omega)$ is the space-time Fourier transform of the spin-spin correlation function, $S(\mathbf{r},t) = \left\langle S(0,0)S(\mathbf{r},t) \right\rangle$, such that [57, 66]

$$S(\mathbf{q},\omega) = \frac{1}{2\pi} \sum_{\mathbf{r_i}} \int_{-\infty}^{\infty} \left\langle S(0,0)S(\mathbf{r_i},t) \right\rangle \cdot e^{i(\mathbf{q}\cdot\mathbf{r_i}-\omega t)} dt \,. \tag{2.29}$$

The summation is taken over every electron spin i at position $\mathbf{r_i}$ relative to the nucleus. $S(\mathbf{q},\omega)$ is the key quantity measured in inelastic neutron scattering experiments, and it is related to the imaginary part of the dynamical electron spin susceptibility $\chi^{''}(\mathbf{q},\omega)$ as

$$S(\mathbf{q},\omega) = \frac{1}{N_A \mu_B} \cdot \frac{\chi^{''}(\mathbf{q},\omega)}{1-e^{-\hbar\omega/k_B T}} \,. \tag{2.30}$$

In the low-frequency limit that is valid for NMR measurements, this relation reduces to

$$S(\mathbf{q},\omega_{NMR}) \propto T \cdot \frac{\chi^{''}(\mathbf{q},\omega_{NMR})}{\omega_{NMR}} \,. \tag{2.31}$$

We can then write $1/T_1$ divided by T as

$$\frac{1}{T_1 T} \propto \sum_{\mathbf{q}} \left| A(\mathbf{q}) \right|^2 \frac{\chi^{''}(\mathbf{q},\omega_{NMR})}{\omega_{NMR}} \,. \tag{2.32}$$

2.7 NMR Electronics

The NMR experiments presented in this thesis were conducted using the spectrometers constructed by former group members Dr. Kent Thurber and Dr. Allen Hunt as well as by Prof. Takashi Imai using commercially available components [69]. Figure 2.5 shows a schematic diagram of the NMR electronics, which has two major functions: (1) to produce the radio frequency (RF) pulses required for stimulating a nuclear transition and (2) to detect the NMR signal. The general flow of the electronics is as follows.

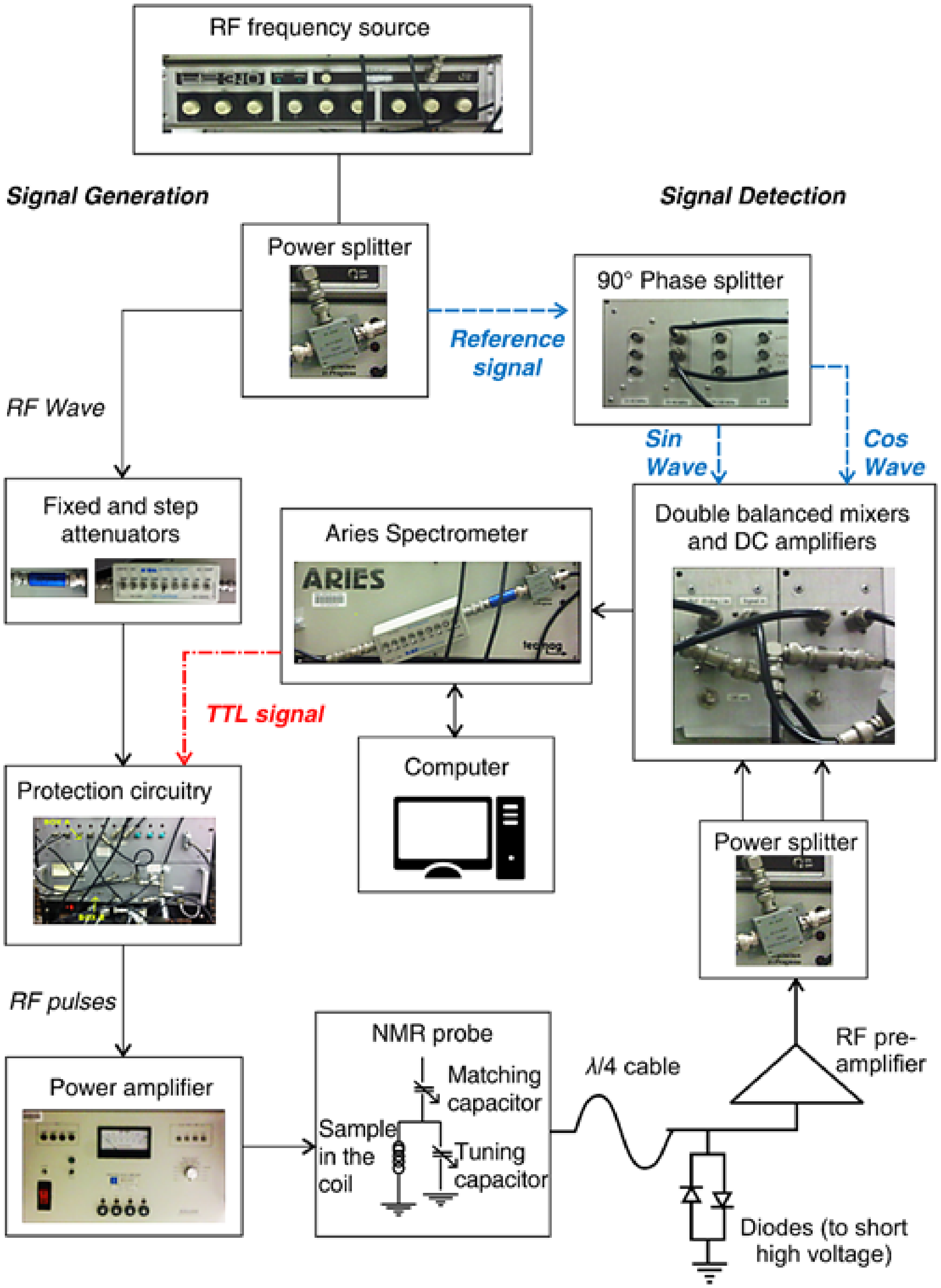

Figure 2.5. The flow diagram of the electronics used in our NMR experiments.

The PTS 310 (or 500) RF frequency source generates continuous RF waves in the frequency range of 1 to 310 (or 500) MHz. These RF waves are divided into two components with identical phase via the power splitter (ZFSC-2-1W by Mini Circuits). One component is used as a reference signal in the detection process, and the other is gated into RF pulses by the TTL (transistor-transistor logic) signals from the Aries spectrometer. These TTL signals are protected by a homemade logic circuitry that controls the trigger line to the power amplifier. This procedure prevents the accidental amplification of continuous RF waves in the case of a computer crash or power surge that may damage both the power amplifier and the sample. The resulting protected RF pulses are then amplified by the Kalmus power amplifier with a gain of +60dB (factor of ~1000) before being fed into the NMR probe.

The tank circuit of the NMR probe comprises two variable capacitors and an inductive coil. By adjusting the capacitors, we can tune the resonant frequency of the circuit to the desired value for the NMR experiments and match the circuit to the 50-Ω impedance of the electronic devices. It should be noted that the breakdown voltage of these variable capacitors limits the maximum output voltage allowed from the Kalmus power amplifier. Therefore, the NMR circuit involves a series of attenuators to reduce the output voltage from the power amplifier. This step aims at preventing the occurrence of arcing, namely, the electric discharge of RF pulses that tends to be exacerbated by helium gas. The sample is placed inside the inductive coil, and therefore, it is subjected to an oscillating transverse field B_1

in the presence of the RF pulses, which induces magnetic resonance. Owing to the resonant response of the system, the coil then generates an induced voltage signal that arises from the nuclear spin precession, i.e., the NMR signal. This process is discussed in Section 2.2.

To detect the extremely weak NMR signal (~μV), we must isolate this signal from any background noise while amplifying its intensity. Immediately upon exiting the probe, the NMR signal goes through a λ/4 cable with length of $45/f_{NMR}$ meters, where f_{NMR} is the desired frequency for the NMR measurement. This cable acts as a selective filter that passes the NMR signal at f_{NMR} while attenuating unwanted voltage signals at all other frequencies. Next, the diodes connected in series suppress any voltage signal that exceeds the threshold of ~0.6V. Then, the NMR signal is amplified by two RF signal pre-amplifiers (LN-2L or LN-2M by Doty) and split into two components with equal phase and intensity by a power splitter. Meanwhile, the continuous RF reference signal is divided into two components of equal intensity with 90° phase difference (*i.e.*, sine and cosine waves). Each of these is mixed with one component of the NMR signal via the double-balanced mixers (DBMs). The DBMs eliminate the frequency components of RF pulses from the NMR signal by subtracting the reference signal from the NMR signal (see Figure 2.6A). This results in two DC components of the NMR signal with 90° phase difference, namely, the real and imaginary components. This procedure is called phase-sensitive detection [56, 69]. After these two DC components of the NMR signal are amplified again by a DC amplifier, they are digitized by the Aries spectrometer for visual display and analysis.

Owing to the finite Q of our tank circuit, it takes $\geq 5\mu s$ for the applied RF pulses to decay, which saturates the preamplifiers. This phenomenon is called ringdown; it may conceal the tiny NMR signal. As our NMR spectrometer is capable of phase-sensitive detection, we apply the phase cycling technique that is effective for isolating the NMR signal from the ringdown. To employ phase cycling in the spin echo sequence, we repeat the sequence four times and vary the phases for both the 90° and 180° pulses, as shown in Table 2.2. For sequences 1 and 2, the 90° rotation of the net nuclear magnetization M_0 takes place around the +x and the –x axis, respectively. The phase of the 180° pulse is adjusted accordingly, and therefore, the spin echo signals generated by these two sequences possess identical phase of +y. Therefore, by adding sequences 1 and 2, the ringdown from the 90° pulse is canceled, whereas the intensity of the spin echo is doubled, as shown in Figure 2.6B. The subtraction between sequences 2 and 4 suppresses the ringdown from the 180° pulse. For NMR measurements that require a short delay time τ or very low frequencies, the phase cycling technique is particularly helpful for achieving a clean NMR signal.

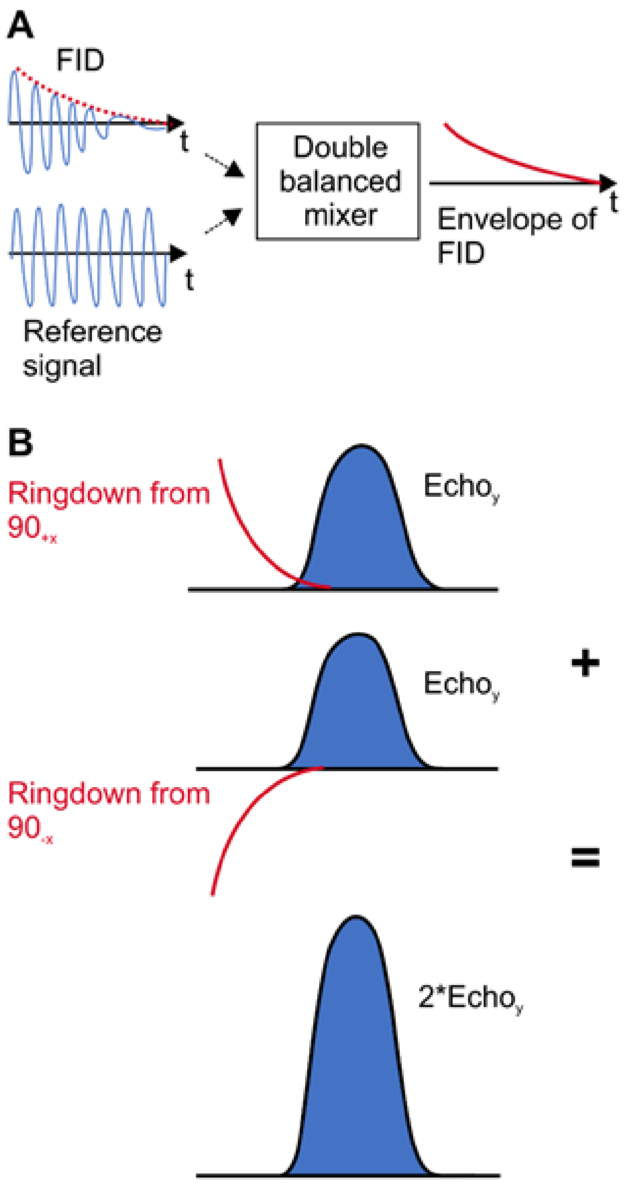

Figure 2.6. Schematic diagrams of phase-sensitive detection (PSD). **(A)** The double-balanced-mixer that mixes the acquired NMR signal with a reference signal to eliminate the frequency components of the RF pulse from the NMR signal. **(B)** The phase cycling process that cancels the ringdown.

Table 2.2. The spin-echo pulse sequences with phase cycling

1	90_{+x}	τ	180_{+x}	τ	echo_{+y}	Add
2	90_{-x}	τ	180_{+x}	τ	echo_{-y}	Subtract
3	90_{-x}	τ	180_{+y}	τ	echo_{+y}	Add
4	90_{+x}	τ	180_{+y}	τ	echo_{-y}	Subtract

2.8 Summary

NMR is a powerful local probe of condensed matter studies. To conduct NMR experiments, we apply a static magnetic field B_{ext} to the sample; this field polarizes both the nuclear and the electron spins via the Zeeman interaction. In addition, we subject the sample to an oscillating RF field B_1 that is perpendicular to B_{ext}. By tuning the frequency of B_1 to the expected resonant frequency, we were able to observe the NMR signals. The hyperfine interaction between the nuclear spin and the nearby electrons allows us to utilize the nuclei for investigating the local electronic properties. In particular, the NMR Knight shift K resulting from the hyperfine magnetic field B_{hf} is proportional to the local uniform spin susceptibility χ_{spin} in the vicinity of the observed nuclear site. Therefore, we can distinguish the various contributions to the bulk-averaged susceptibility χ_{bulk} by measuring the temperature dependence of K at distinct nuclear sites. This feature is extremely useful for investigating selectively the intrinsic spin susceptibility χ_{kagome} of the kagomé plane under the presence of defects, which is discussed in the following chapters. Moreover, the nuclear spin-lattice relaxation rate $1/T_1$ probes the low-energy excitations of the electron spin system, which are typically in the μeV range. This makes NMR an excellent complementary technique to neutron and X-ray scattering studies.

Chapter 3

Herbertsmithite $ZnCu_3(OH)_6Cl_2$ and the Defect Controversy

The S=1/2 kagomé-lattice Heisenberg antiferromagnet herbertsmithite $ZnCu_3(OH)_6Cl_2$ is a leading candidate for experimental realization of the QSL state. The successful synthesis and characterization of $ZnCu_3(OH)_6Cl_2$ [24] has stimulated intensive research into its physical properties. However, establishing this material as a quantum spin liquid remains a challenge, primarily owing to the difficulty in revealing the intrinsic magnetic behavior of the kagomé lattice from defect contributions. In this chapter, we first provide an overview of recent experimental studies on $ZnCu_3(OH)_6Cl_2$, outlining the motivation behind our single-crystal NMR experiments. We then focus on presenting the results of ^{17}O Knight shift measurements performed in an external magnetic field $B_{ext} = 9T$ along the c-axis, which enables us to settle the longstanding controversy regarding the nature of the defects.

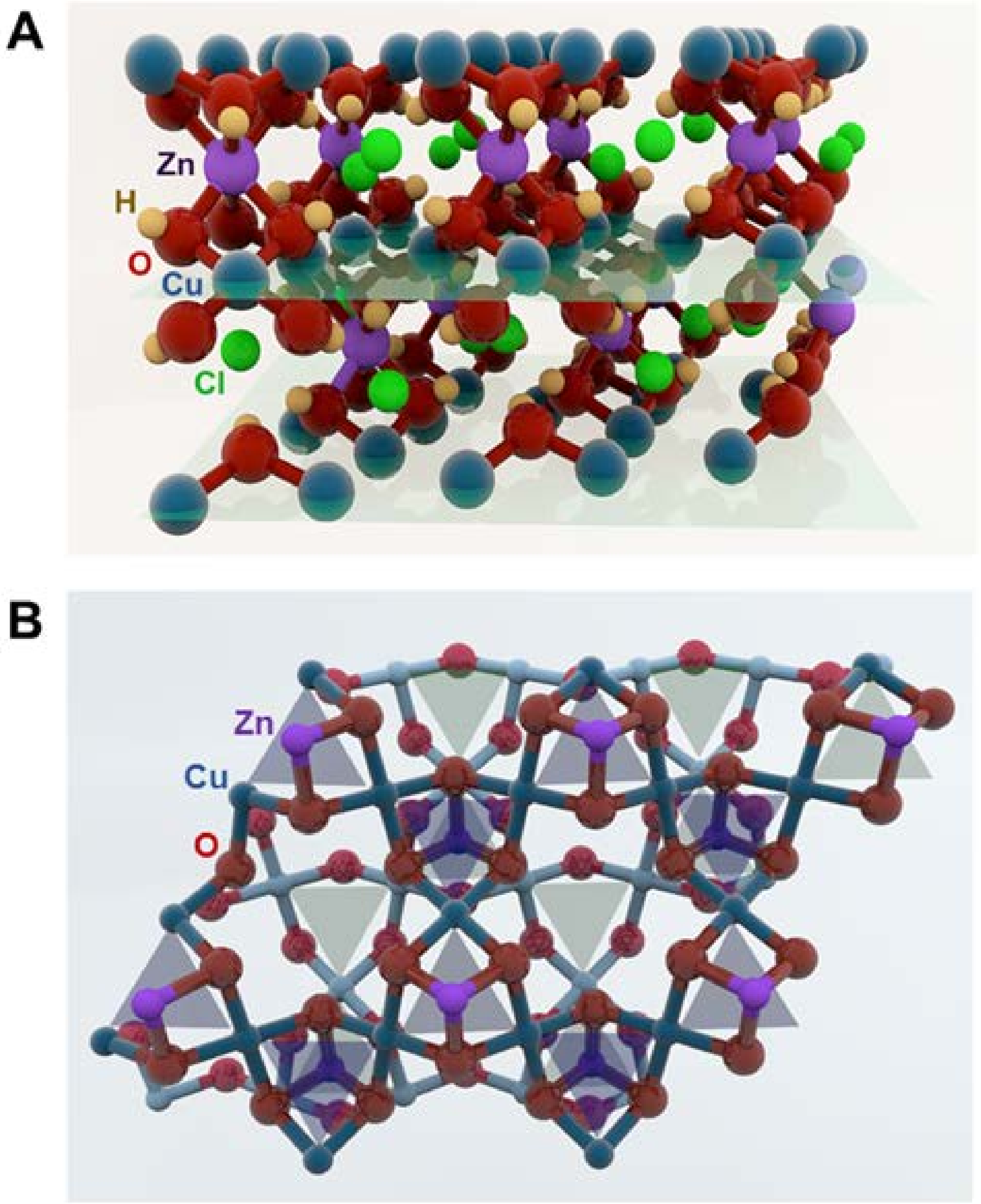

Figure 3.1. Crystal structure of $ZnCu_3(OH)_6Cl_2$. **(A)** Side view of the structure of $ZnCu_3(OH)_6Cl_2$. **(B)** Top view of the two layers of the Cu_3O_3 kagomé lattice; the adjacent lattice planes are separated by nonmagnetic Zn^{2+}.

3.1 Crystal structure of $ZnCu_3(OH)_6Cl_2$

As the $x = 1$ end member of the Zn-paratacamite family $Zn_xCu_{4-x}(OH)_6Cl_2$, $ZnCu_3(OH)_6Cl_2$ comprises a kagomé lattice of hydroxide-bridged Cu^{2+} ions with Cu-O-Cu bond angles of 119°; these kagomé lattice planes are separated by a layer of nonmagnetic Zn^{2+} ions along the c-axis [24]. The crystal structure is depicted in Figure 3.1. Each Cu^{2+} ion is located in a tetragonally elongated chemical environment involving four equatorial O^{2-} ions with a Cu-O distance of 1.98Å, and two apical Cl^- ions with Cu-Cl distance of 2.77Å. The interlayer Zn^{2+} ion is enclosed in an octahedral cage of six O^{2-} ions with identical Zn-O bond length of 2.10Å. These $[Zn(OH)_6]$ units link the kagomé layers via the hydroxide ligands with a Zn-O-Cu bond angle of 96.7° [17, 70]. With one vacancy in the 3d orbitals, Cu^{2+} is a Jahn-Teller distorting ion [71], and therefore its occupancy is energetically favored in the tetragonal environment of the kagomé sites. In contrast, Zn^{2+} consists of completely filled 3d shells and is most commonly coordinated in the octahedral environment of the interlayer sites [72].

In Figure 3.2, we illustrate the variation of the crystal structure of the Zn-paratacamite family $Zn_xCu_{4-x}(OH)_6Cl_2$ as Zn concentration increases. The parent phase clinoatacamite $Cu_2(OH)_3Cl$ $(x = 0)$ consists of monoclinicly distorted kagomé layers that are coupled ferromagnetically via the interlayer magnetic Cu^{2+} ions. This material undergoes a transition to a long-range magnetic ordered state at ~6 K. By increasing the Zn occupancy at the interlayer sites to approximately $x = 0.33$, the crystal symmetry transforms from monoclinic ($P2_1/n$) to rhombohedral ($R\bar{3}m$). As a result, the Cu^{2+} ions within the *ab*-plane form equilateral triangles, leading to a structurally perfect kagomé lattice. With $x = 1$, the interlayer sites are fully occupied by nonmagnetic Zn^{2+} ions, which completely suppress the magnetic bridge between adjacent kagomé planes, thereby resulting in the two-dimensional S = 1/2 kagomé lattice in $ZnCu_3(OH)_6Cl_2$ [24, 30].

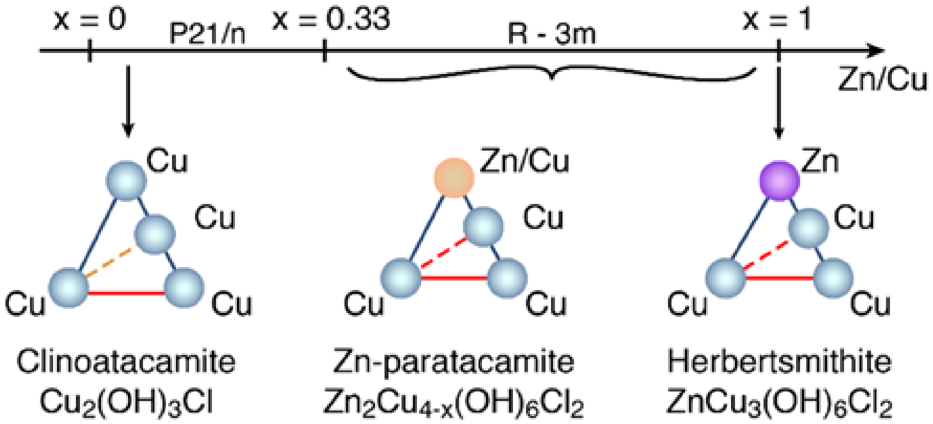

Figure 3.2. Evolution of the structure of paratacamites with increasing Zn concentration x. A structural phase transition occurs at approximately x = 0.33, which results in a kagomé lattice of Cu^{2+} in the *ab*-plane. With full Zn occupancy ($x = 1$) at the interlayer sites, the magnetic bridges between neighboring kagomé planes are completely suppressed, thereby yielding the two-dimensional S = 1/2 kagomé lattice in $ZnCu_3(OH)_6Cl_2$.

3.2 Experimental advances and challenges

The discovery of $ZnCu_3(OH)_6Cl_2$ has triggered intense experimental investigations that aim to identify signatures of an exotic ground state. Early experiments on powder samples of $ZnCu_3(OH)_6Cl_2$ demonstrated that, despite the strong short-range antiferromagnetic Cu-Cu exchange coupling $J \sim 17\text{meV}$, the system does not undergo a magnetic long-range order or a spin freezing down to at least $T \sim 50\text{mK}$; this feature is a promising hint of a quantum spin-liquid state [73-75]. Recently, the success in synthesizing high-quality single crystals of $ZnCu_3(OH)_6Cl_2$ [76] marked a major milestone in the study of its physical properties. In particular, inelastic neutron scattering measurements on single crystals revealed a continuum of spin excitations, in contrast to the conventional magnons expected in a magnetically ordered state. This finding is considered one piece of crucial evidence for the presence of deconfined spinon excitations with S = 1/2, a signature of a quantum spin-liquid state realized in this material [77].

Despite recent progress, fundamental issues regarding the nature of the non-magnetic ground state in $ZnCu_3(OH)_6Cl_2$ remain far from settled. For instance, the central question of whether a gap exists in the spin excitation spectrum is still open to debate. This information is key to distinguishing among the competing theoretical proposals for the ground state of the S = 1/2 kagomé antiferromagnet mentioned in Chapter 1. The challenge in classifying the ground state of $ZnCu_3(OH)_6Cl_2$ stems from the presence of defects, whose nature remains controversial. An early ^{17}O powder NMR study by Olariu *et al.* [78] suggested the presence of approximately ~5% intersite exchange between Zn^{2+} and Cu^{2+} ions, also known as “anti-site disorder”; consequently, ~5% of Cu^{2+} ions within the kagomé planes are replaced by nonmagnetic Zn^{2+}, as illustrated in Figure 3.4C. These Zn^{2+} defects could generate spin singlet pairs in their vicinity, which might provide a trivial explanation for the observed nonmagnetic ground state of $ZnCu_3(OH)_6Cl_2$ without invoking a spin-liquid state.

In contrast, the recent site-specific anomalous X-ray diffraction measurements on single crystals by Freedman *et al.* [70] reported ~5% excess Cu^{2+} ions occupying Zn^{2+} in the interlayer sites and determined that the concentration of Zn^{2+} inside the kagomé plane is negligible; their experiments set the upper bound of Zn^{2+} anti-site defects as ~1%. Accordingly, the actual structural formula was estimated as $(Zn_{0.85}Cu_{0.15})Cu_3(OH)_6Cl_2$.

The presence of $S = 1/2$ Cu^{2+} on the Zn interlayer sites poses significant challenges for identifying the ground state using bulk-averaged magnetic susceptibility. As shown in Figure 3.3A, the bulk-averaged susceptibility χ_{bulk} exhibits a large Curie-Weiss enhancement below ~50K, which contradicts the theoretically predicted behavior of the spin susceptibility χ_{kagome} of an ideal kagomé antiferromagnet; χ_{kagome} is expected to decrease in the low temperature regime, as shown in Figure 3.3B, and its behavior near $T = 0$ varies depending on the nature of the ground state [39, 52, 53]. In the presence of a spin gap, χ_{kagome} is expected to decline exponentially with decreasing temperature [33, 34], while the gapless excitation of an algebraic spin liquid will give rise to a *T*-linear behavior of χ_{kagome} toward T = 0 [11, 12]. In addition, for a spin liquid state with a spinon Fermi surface, χ_{kagome} would display a finite intercept $\chi_0 = \mu_B^2 D(\varepsilon_F)$ at *T* = 0, where μ_B is the Bohr magneton and $D(\varepsilon_F)$ is the density of states at the Fermi surface [79, 80]. The inelastic neutron scattering measurements revealed no evidence of a spin gap down to 0.25meV (~ *J*/70). However, the Cu^{2+} defect moments strongly contribute to the excitations in the neutron scattering spectrum at low energies $(< 2\text{meV})$ and may conceal the intrinsic gap of the kagomé spins even if the gap exists [77, 83, 84]. Furthermore, once the interlayer site is occupied by a S = 1/2 Cu^{2+} defect, it is possible that the defect interacts with the constituent Cu^{2+} of the kagomé plane directly above and below, thereby complicating the matter further.

NMR plays a pivotal role in probing the intrinsic magnetic behavior of host materials in the presence of defects, as demonstrated by successful investigations of Kondo-oscillations and similar phenomena in metals [85, 95], high-T_c superconductors [86], and low-dimensional spin systems [87]. Bulk experimental techniques such as the superconducting quantum interference device (SQUID) measure susceptibilities averaged over the entire sample, mixing the contribution from defects with intrinsic behaviors. In contrast, NMR is a local probe, and therefore it distinguishes susceptibilities subjected to different local magnetic environments, as discussed in Chapter 2. Consequently, it enables us to untangle the effects from the defects and directly probe the intrinsic magnetic properties of the kagomé lattice. Moreover, using single crystals for NMR measurements is more effective than measuring powder samples. By applying an external magnetic field along a specific crystallographic orientation, the single-crystal NMR lineshapes provide higher spectral resolution by eliminating the line broadening caused by anisotropic magnetic and quadrupole interactions, and therefore maximize the possibility for identifying NMR signals originating from the intrinsic kagomé sites.

Unfortunately, our earlier attempts to elucidate the behavior of the intrinsic spin susceptibility χ_{kagome} using ^{2}D and ^{35}Cl single-crystal NMR were unsuccessful due to the limited transferred hyperfine coupling at these sites [81, 82]; while ^{63,65}Cu NMR was ineffective as a result of the large quadrupole interaction $\nu_Q \sim 40.6$MHz. Since O^{2-} ions bridge the super-exchange interaction between the two neighboring Cu^{2+} ions within the kagomé plane, they are expected to possess substantial transferred hyperfine coupling from the Cu^{2+} at the kagomé sites. In addition, the typical quadrupole interaction of ^{17}O is about two orders of magnitude smaller than that of ^{63,65}Cu. Therefore, ^{17}O NMR is the best possible compromise for probing the intrinsic magnetic behavior of the kagomé lattice and the influence of the defects on intrinsic magnetism.

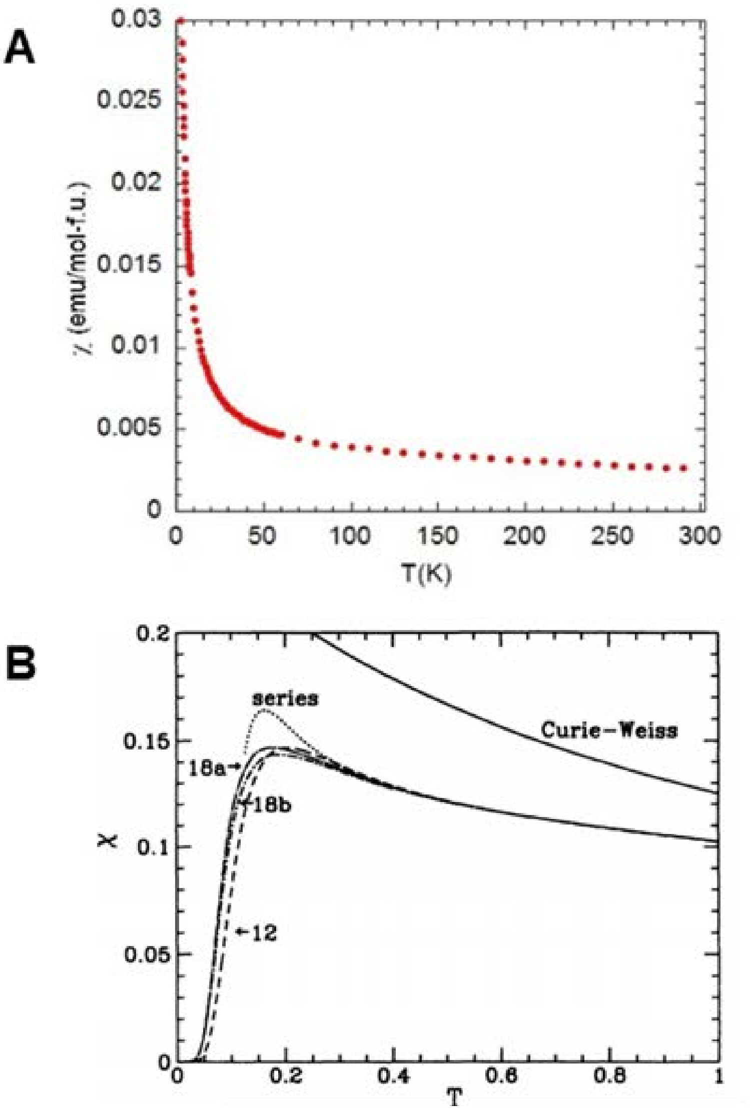

Figure 3.3. A comparison between the bulk-averaged magnetic susceptibility χ_{bulk} of ZnCu$_3$(OH)$_6$Cl$_2$ measured by SOUID at $B_{ext} = 0.2T \parallel c$ **(A)** and the theoretically predicted behavior of the spin susceptibility χ_{kagome} of an ideal kagomé antiferromagnet **(B)**. Panel **(B)** is reprinted with permission from Ref. [52]. Copyright (1994) The American Physical Society.

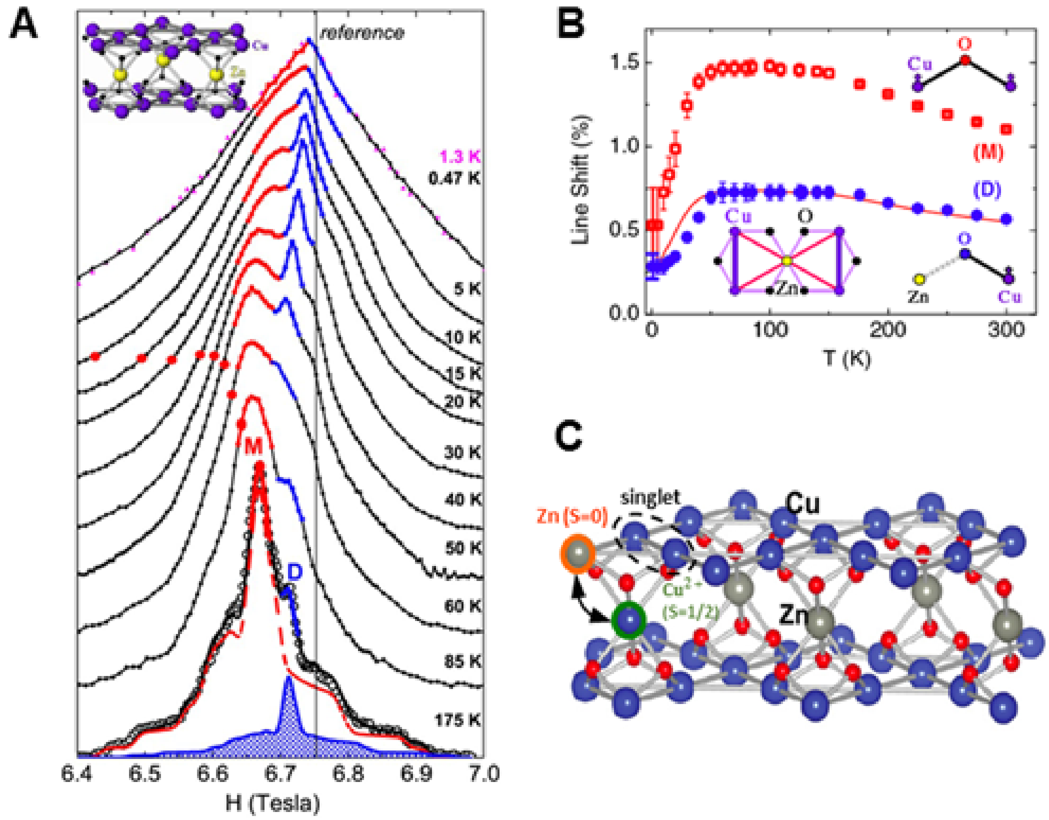

Figure 3.4. The ^{17}O powder NMR study of $ZnCu_3(OH)_6Cl_2$ by Olariu *et al*. [78]. **(A)** The representative field-swept ^{17}O powder NMR lineshapes at a fixed frequency of 38.974MHz. The vertical line indicates the zero Knight shift position. The powder lineshapes reveal two distinct ^{17}O sites: *Main* (M) and *Defec*t (D) sites. **(B)** The temperature dependence of Knight shift at the *Main* (M) and *Defect* (D) sites. **(C)** An illustration of the “anti-site disorder” (black arrow) and a spin singlet (dashed circle) near the Zn^{2+} (S = 0) defect inside the kagomé plane. Panels **(A)** and **(B)** are reprinted with permission from Ref. [78]. Copyright (2008) The American Physical Society.

3.3 ^{17}O NMR measurements at B_{ext} = 9T∥c

The $ZnCu_3(OH)_6Cl_2$ single crystal used for our ^{17}O NMR measurements is grown by the hydrothermal method described in Ref. [76]. The crystal is enriched with ^{17}O isotope using enriched-water ($H_2{}^{17}O$) as a starting ingredient. Approximately ~10% of the ^{16}O sites were replaced with the ^{17}O isotope. The our primary goal is to unveil the nature of the ground state of $ZnCu_3(OH)_6Cl_2$ by probing the intrinsic spin susceptibility χ_{kagome} separately from the defect-induced contribution χ_{defect}. Nonetheless, to understand the ground state properties of this material, we must first identify the location of the defect and elucidate its magnetic behavior. In the following sections, we present our NMR data collected with an external magnetic field of 9T applied along the c-axis $(B_{ext} = 9\ T \parallel c)$, which enables us to unveil the nature of the defects.

3.3.1 Pinpointing the location of the defects

As mentioned in Chapter 2, the ^{17}O nucleus has a nuclear spin of I = 5/2. If we assume that there is no defect, such that all ^{17}O nucleus in $ZnCu_3(OH)_6Cl_2$ reside in the same local environment, then with an external field magnetic field B_{ext} applied along the c-axis, we would observe five resonance peaks in the single-crystal lineshapes. In reality, as shown in Figure 3.5, the ^{17}O lineshape measured in $B_{ext} = 9T \parallel c$ at 295K consists of three groups of five peaks labelled respectively as A, B, and C. This feature clearly indicates that the presence of defects results in three ^{17}O sites with distinct magnetic and structural properties in $ZnCu_3(OH)_6Cl_2$.

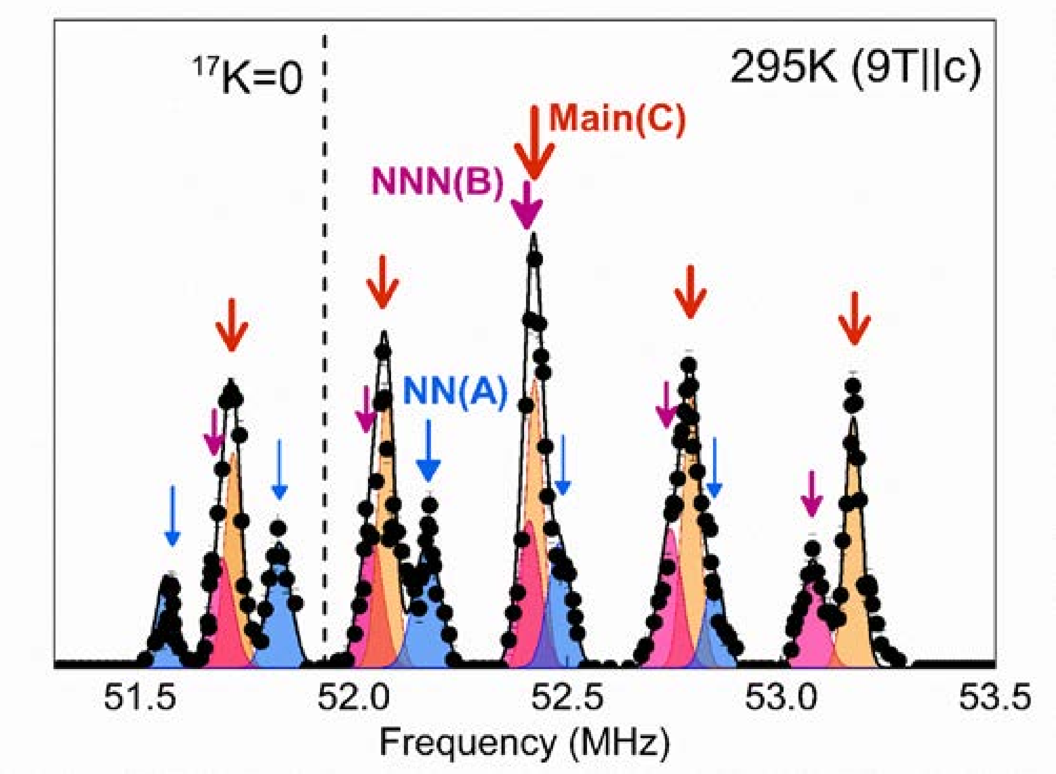

Figure 3.5. The room-temperature ^{17}O NMR lineshape measured at $B_{ext} = 9T \parallel c$ with $\tau = 15\mu s$. The lineshape is fitted with three sets of five Gaussian peaks arising from the *NN* (A) ($\nu_Q \sim 310\text{kHz}$), *NNN* (B) ($\nu_Q \sim 350\text{kHz}$) and *Main* (C) ($\nu_Q \sim 350\text{kHz}$) sites. The dashed vertical line marks the zero-shift frequency $f_0 = \gamma_N B_{ext} \sim 51.9\text{MHz}$, at which $^{17}K^{(c)} = 0$. After T_2 correction, we estimated the integrated intensity of the isolated second satellite peaks ($I_z = \pm 5/2$ to $\pm 3/2$) of the three sites by calculating the product of the peak amplitude and the linewidth at

half amplitude. The resulting relative population of the *NN* (A), *NNN* (B), and *Main* (C) sites are 13 ±4%, 28 ±5%, and 59 ±8%, respectively.

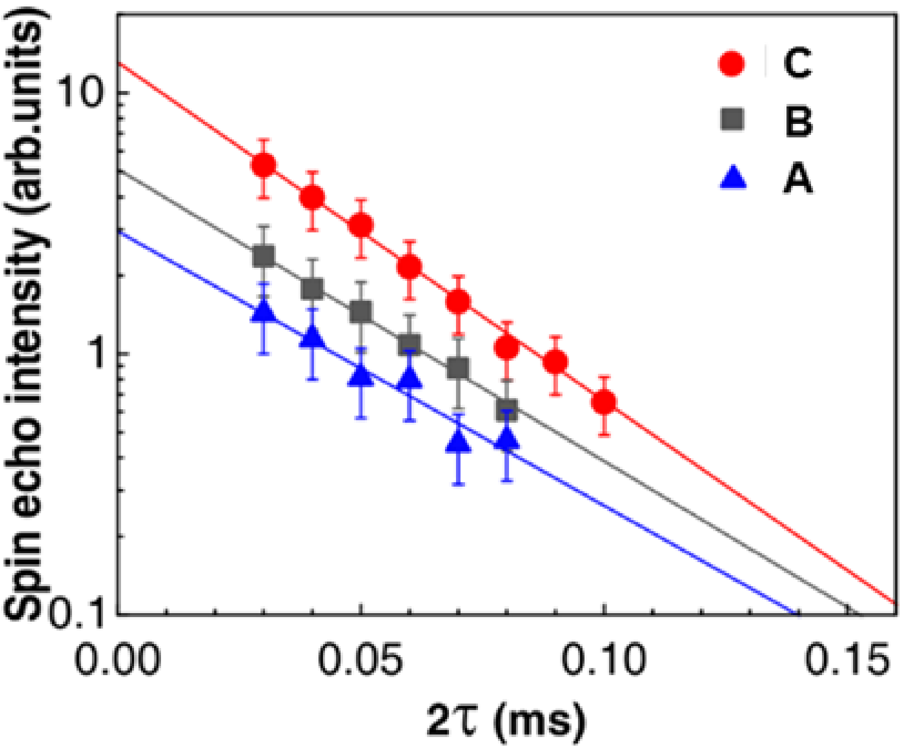

Figure 3.6. The T_2 spin echo decay measured at 295K in $B_{ext} = 9T \parallel c$ for the *NNN* (B) (uppermost satellite peak at 53.073MHz) and *NN* (A) sites (lowermost satellite peak at 51.573MHz), and *Main* (C) (uppermost satellite peak at 53.163MHz) sites. The solid lines represent the single exponential fits. In our estimation of the relative intensities of the *Main*, *NN*, and *NNN* sites, we accounted for the effect of the different spin-echo decay rate on the lineshape when estimating the relative population of the three sites.

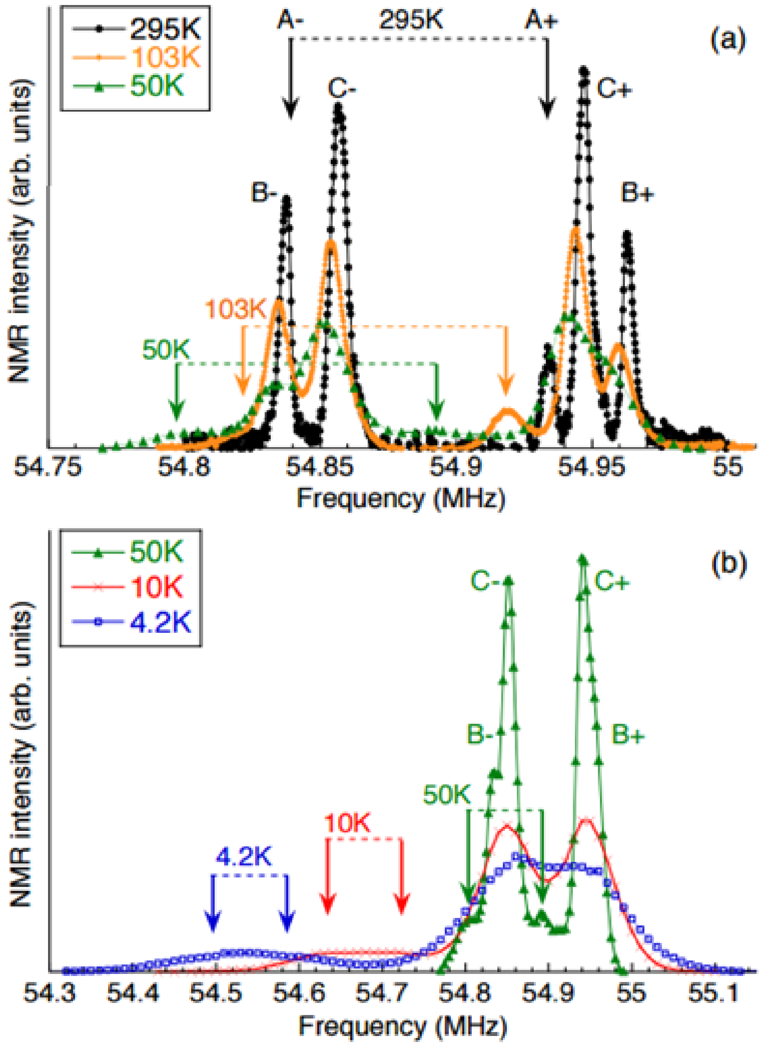

Figure 3.7. Representative ^{2}D NMR lineshapes measured at $B_{ext} = 8.4T \parallel c$. The lineshapes consist of three pairs of NMR peaks arising from the *NN* (A), *NNN* (B), and *Main* (C) sites. Downward arrows mark the resonant frequencies $f_{\pm}$ for the two NMR peaks of NN (A) sites. This figure is reprinted with permission from Ref. [82]. Copyright (2011) The American Physical Society.

In order to identify the location of these ^{17}O sites with respect to the defects, we must first estimate their relative intensities. Figure 3.6 presents the spin-echo decay measured at the well-resolved second satellite peaks ($I_z = \pm 5/2$ to $\pm 3/2$) of the three ^{17}O sites as a function of 2τ, where τ is the delay time in the spin-echo sequence. For all three ^{17}O sites, the decay of spin-echo intensity is dominated by the T_1 relaxation process and follows a single exponential [56]. The transverse relaxation times T_2 of the three sites are different from one another, thereby leading to varying rates of decay. Since B and C sites possess shorter T_2 than A sites, the satellite peaks corresponding to B and C sites display faster decline of intensity; therefore their intensity tends to be underestimated in comparison to the satellite peak of A sites at $\tau = 15\mu s$, the delay time we used for all lineshape measurements at 9T. To properly estimate the population ratio of the three sites, we extrapolated the intensity of the satellite peaks to $\tau = 0$, a process called T_2 correction. We then estimated that the population of A, B, and C sites are 13 ± 4%, 28 ± 5% and 59 ± 8%, respectively. This result is in agreement with the earlier ^{2}D NMR observation of three corresponding sites with relative population of 14 ± 2%, 28 ± 4% and 58 ± 4% in deuterated $ZnCu_3(OH)_6Cl_2$ single crystals, as shown in Figure 3.7 [82].

The intensity ratio of the three ^{17}O sites provides key evidence for deducing the nature of the defects. As depicted in Figure 3.8, each S = 1/2 Cu^{2+} defect replacing the interlayer Zn^{2+} are surrounded by six nearest-neighbor (*NN*) ^{17}O and twelve next nearest-neighbor (*NNN*) ^{17}O. The 1:2 ratio of *NN* ^{17}O and *NNN* ^{17}O is identical to the intensity ratio of A and B sites. Thus, we can naturally assign the A and B sites to the *NN* and *NNN* of Cu^{2+} defects, respectively, which implies that ~15% of the interlayer Zn sites are occupied by Cu^{2+} defect, equivalent to ~5% of excess Cu^{2+} at Zn sites. This finding implies that the actual chemical composition is $(Zn_{0.85}Cu_{0.15})Cu_3(OH)_6Cl_2$, which is consistent with the ^2D NMR [82] and the anomalous X-ray diffraction measurements [70] on single crystals. The C sites represent the *Main* ^{17}O sites located far from the defects. These sites are least influenced by the defects, and therefore enable us to probe the intrinsic spin susceptibility χ_{kagome} of the kagomé lattice. Henceforth, we will refer to A, B, and C sites as *NN*, *NNN*, and *Main*, respectively.

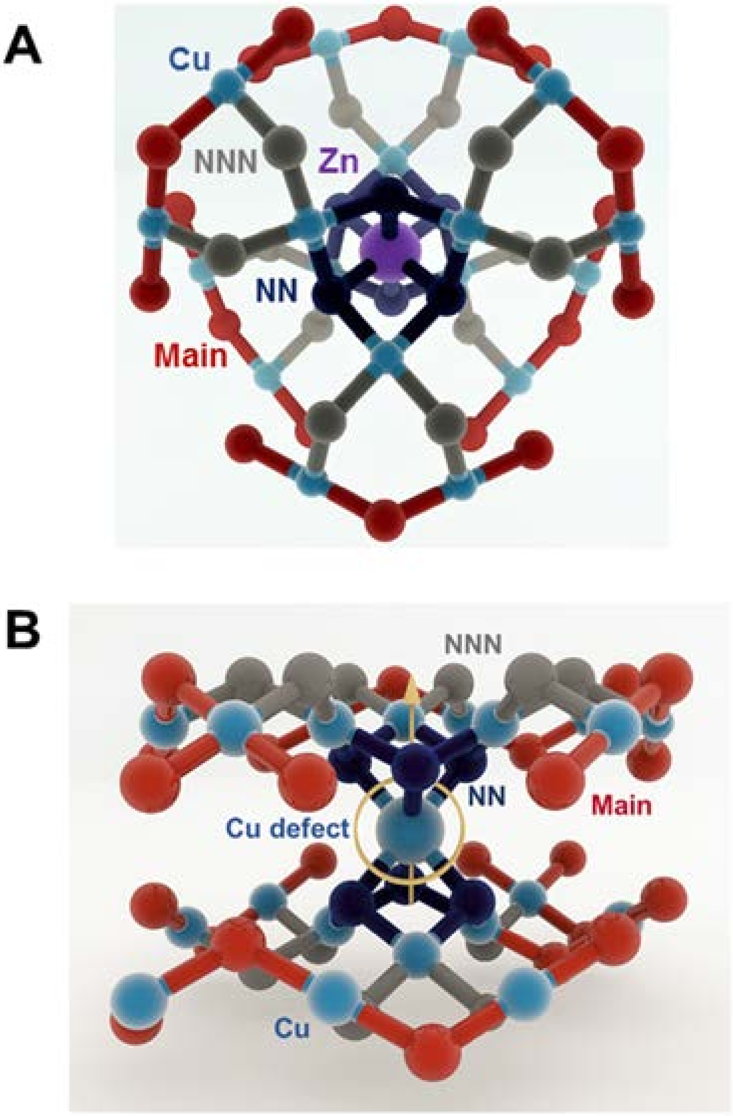

Figure 3.8. The local crystal structure of a Cu^{2+} defect occupying the interlayer Zn^{2+} site. **(A)** A nonmagnetic Zn^{2+} (purple) linking two adjacent kagomé layers of Cu^{2+} (top view). Each Zn^{2+} site is surrounded by six *NN* (navy blue) and twelve *NNN* (grey) ^{17}O sites. **(B)** Side view of the local environment around a Cu^{2+} defect (yellow circle) at the interlayer Zn^{2+} site polarized by $B_{ext} \parallel c$ (upward arrow).

3.3.2 Knight shift $^{17}K^{(c)}$

The temperature dependence of ^{17}O Knight shift $^{17}K_{NN}^{(c)}$ at the *NN* sites reflects the magnetic property of the excess S = 1/2 Cu^{2+} defects at the interlayer Zn sites. Figure 3.9 presents the variation of ^{17}O NMR lineshapes measured in $B_{ext} = 9T \parallel c$ as the temperature decreases. Below 77K, all relatively sharp, resolvable features in the lineshapes originate from the *NN* ^{17}O sites. Moreover, as shown in Figure 3.10, the peaks of *NN* ^{17}O sites may be isolated with a long delay time $\tau \geq 200\mu s$ in the low temperature regime. This feature indicates that the transverse relaxation time T_2 of the *NN* ^{17}O sites is significantly longer than T_2 of the *Main* and *NNN* ^{17}O sites. Note that the central peak frequency of the *NN* ^{17}O sites crosses the Larmor frequency ($^{17}K = 0$) at approximately 30K and becomes increasingly negative with decreasing temperature.

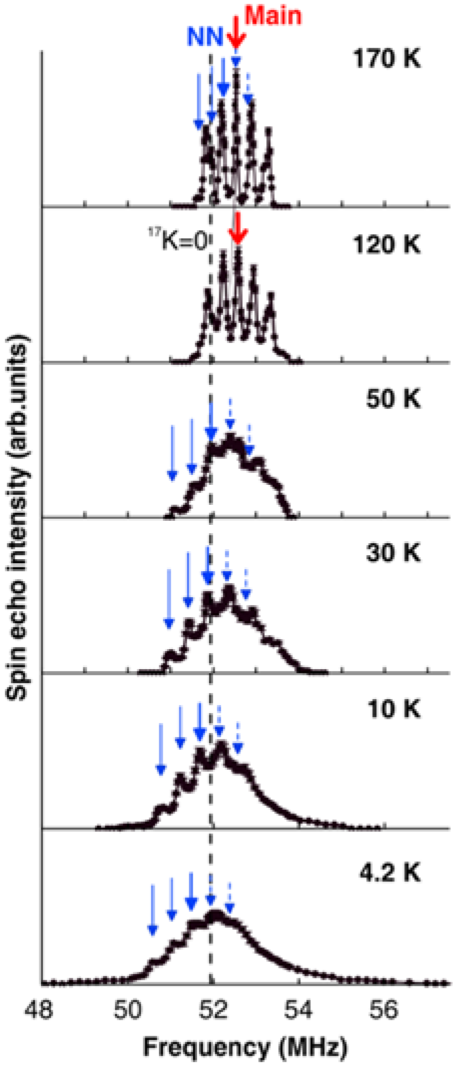

Figure 3.9. Temperature dependence of ^{17}O NMR lineshapes measured at $B_{ext} = 9T \parallel c$. The dashed vertical line represents the zero-shift frequency $f_0 = \gamma_N B_{ext} \sim 51.9\mathrm{MHz}$, at which $^{17}K^{(c)} = 0$. The blue arrows mark the resonant frequencies of the five NMR peaks of *NN* sites, and the red arrows indicate the central peak frequency (I_z = -1/2 to +1/2) of the *Main* sites.

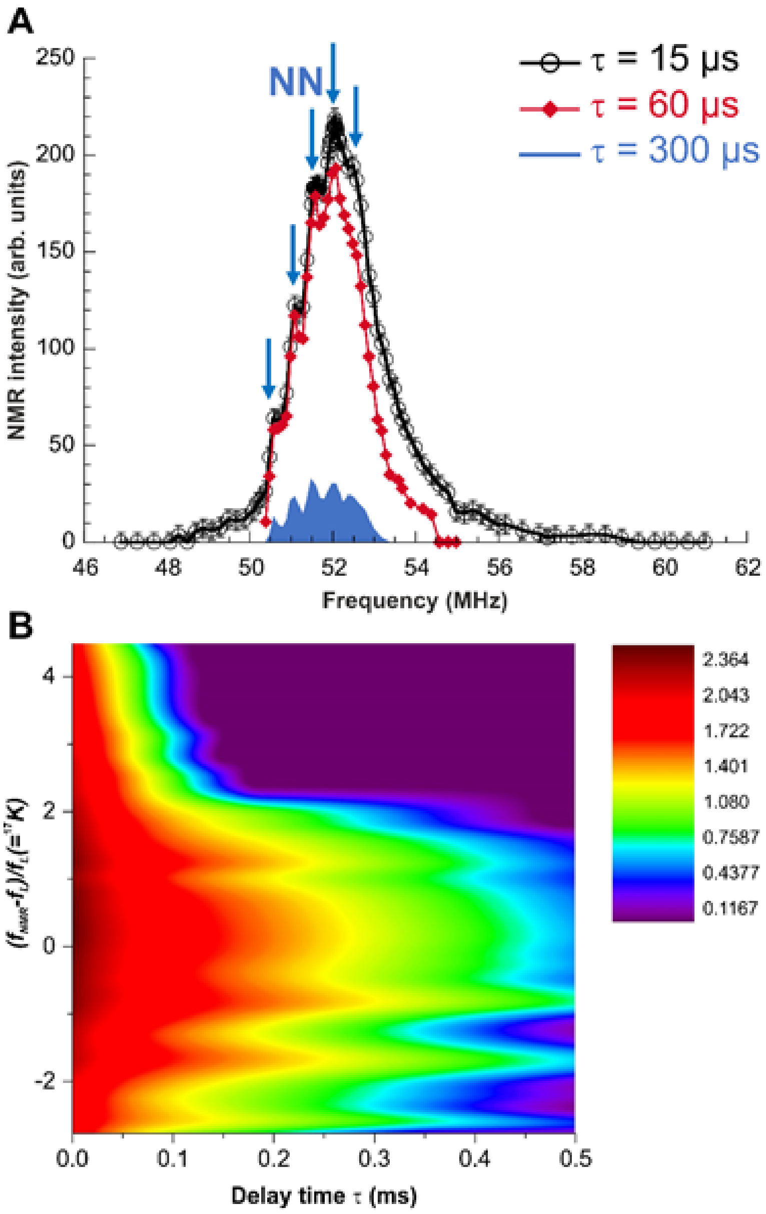

Figure 3.10. The variation of ^{17}O NMR lineshapes with increasing delay time τ at 4.2 K in $B_{ext} = 9T \parallel c$. **(A)** A comparison of lineshapes obtained with $\tau = 15\mu s$, $60\mu s$ and $300\mu s$. The overall intensity of the $\tau = 60\mu s$ and $300\mu s$ lineshapes are magnified by a factor of two for clarity. **(B)** A color map of the NMR intensity distribution as a function of τ. The NMR peaks of the NN sites are isolated with

long $\tau \geq 200\mu s$ due to the slow transverse relaxation time T_2, whereas the high-frequency tail with much shorter T_2 is suppressed with $\tau \geq 60\mu s$. This high-frequency tail is most likely to arise from the *NNN* sites with a large, positive Knight shift (to be discussed in more detail in Chapter 5).

In Figure 3.11, we summarize the temperature dependence of the Knight shift at *NN*, *NNN*, and *Main* ^{17}O site, namely, $^{17}K_{NN}^{(c)}$, $^{17}K_{NNN}^{(c)}$, and $^{17}K_{Main}^{(c)}$. The Knight shift $^{17}K^{(c)}$ and the quadrupole frequency $\nu_Q^{(c)}$ at the *NNN* and *Main* sites are almost identical. Consequently, we could distinguish them only in the high temperature regime, where the NMR lines are sufficiently narrow for the uppermost second satellite peak of *NNN* sites to be resolved (the behavior of *NNN* sites is discussed in more detail in Chapter 5). The Knight shift at *NN* sites $^{17}K_{NN}^{(c)}$ consists of both the defect and intrinsic contributions, such that

$$^{17}K_{NN}^{(c)} \cong \frac{A_{hf}^{kagome}}{N_A\mu_B}\chi_{kagome} + \frac{A_{hf}^{defect}}{N_A\mu_B}\chi_{defect}. \tag{3.1}$$

At high temperatures, $^{17}K_{NN}^{(c)}$ behaves similarly to $^{17}K_{Main}^{(c)}$, except that $^{17}K_{NN}^{(c)}$ is halved in magnitude. This feature indicates that, at high temperatures, the defects have a negligible effect on the *NN* ^{17}O sites, while the hyperfine coupling A_{hf}^{kagome} of the intrinsic contribution at the *NN* sites is approximately one-half of that at the *Main* sites. Below 50K, the behavior of $^{17}K_{NN}^{(c)}$ is dominated by the defect-induced component ${}^{17}K^{(c)}_{defect} = \frac{A_{hf}}{N_A \mu_B} \cdot \chi_{defect}$, which follows the Curie-Weiss law and saturates toward $T = 0$. Note that the peaks of *NN* ^{2}D sites in Figure 3.7 progressively shift to lower frequencies and split off from the peaks of *Main* and *NNN* sites below ~10K. The corresponding Knight shift ${}^{2}K^{(c)}_{NN}$ of the *NN* ^{2}D sites exhibits a sharp Curie-Weiss enhancement with negative sign [82], which is consistent with the low temperature behavior of ${}^{17}K^{(c)}_{NN}$. This result clearly indicates that the defects are S = 1/2 Cu^{2+} at interlayer Zn sites, which behave as nearly free spins. Both ${}^{17}K^{(c)}_{NN}$ and ${}^{2}K^{(c)}_{NN}$ are negative at low temperatures, implying that the polarization of Cu^{2+} defect spins results in a negative transferred hyperfine coupling $A^{defect}_{hf} < 0$ at the *NN* ^{17}O and ^{2}D sites. We estimated $A^{defect}_{hf} \simeq -24 kOe/\mu_B$ at the *NN* ^{2}D sites, while A^{defect}_{hf} at the *NN* ^{17}O sites is ~2 times larger in magnitude.

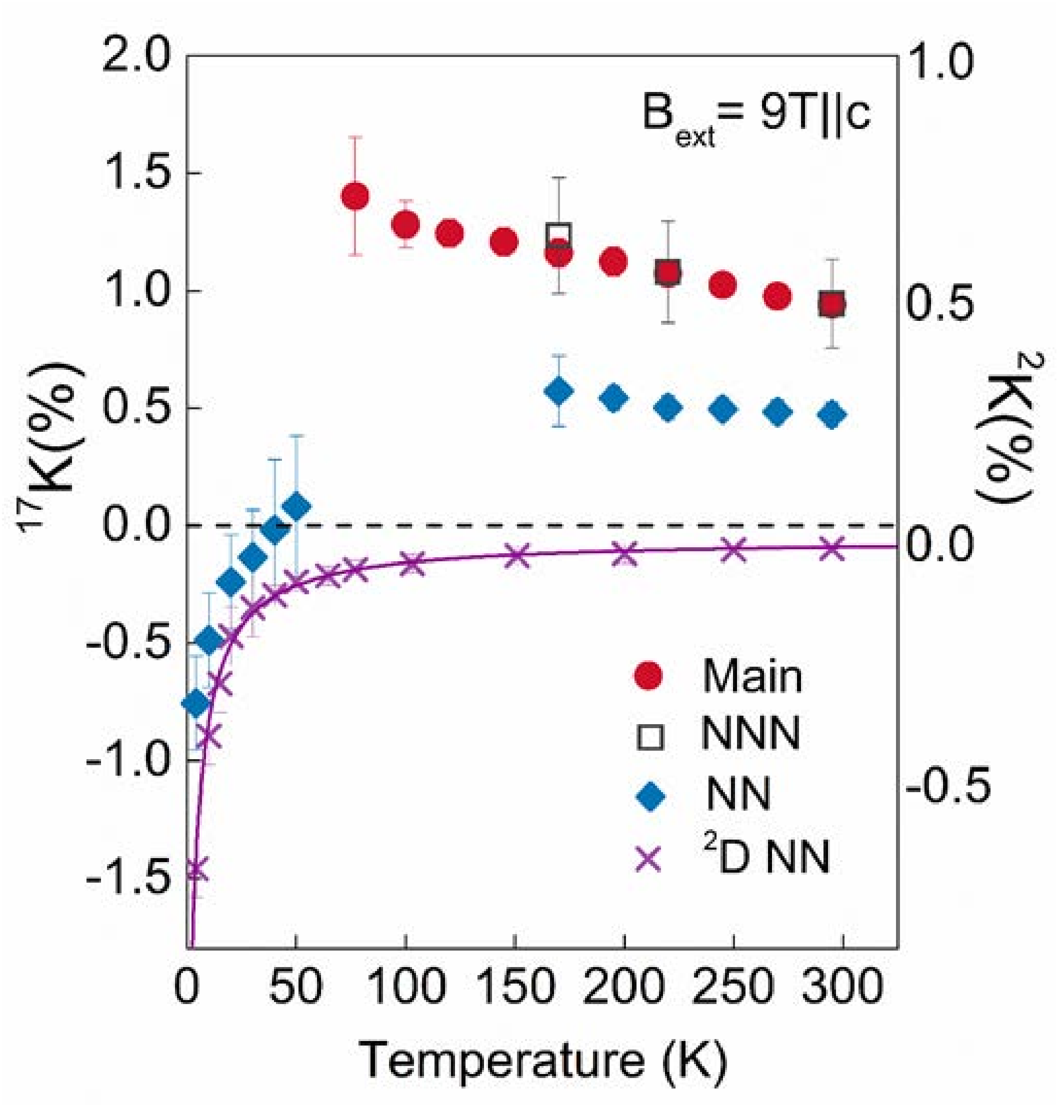

Figure 3.11. The temperature dependence of the Knight shift $^{17}K^{(c)}$ at *NN*, *NNN*, and *Main* ^{17}O sites measured at $B_{ext} = 9T \parallel c$. Also included is the Knight shift $^{2}K^{(c)}$ at the *NN* ^{2}D sites obtained at $B_{ext} = 8.4T \parallel c$ that is dominated entirely by the defect Cu^{2+} spins; the solid line represents a Curie-Weiss fit $^{2}K_{NN}^{(c)} \propto -(T-\theta)^{-1}$ with Weiss temperature $\theta \sim -1.2K$.

The *Main* ^{17}O peaks undergo dramatic broadening as temperature decreases, and overlap with the sharp *NN* peaks below ~70K, as shown in Figure 3.9. Consequently, we cannot track the low temperature behavior of the intrinsic spin susceptibility χ_{kagome} using $^{17}K_{Main}^{(c)}$. In the next chapter, we show that the field geometry of $B_{ext} \parallel a^*$ provides an optimal condition for resolving the *Main* ^{17}O peaks, which allows us to measure χ_{kagome} directly in the low temperature regime.

3.3.3 Comparison with earlier ^{17}O powder NMR data

The ^{17}O single-crystal lineshapes show no signature associated with nonmagnetic Zn^{2+} defects occupying the Cu^{2+} sites within the kagomé layers. Therefore, we conclude that the anti-site disorder inside the kagomé plane is negligible. In contrast, the earlier ^{17}O powder NMR report claimed that approximately ~5% of the kagomé Cu^{2+} sites are replaced by non-magnetic Zn^{2+} defects that leads to spin singlets in their vicinity [78]. To clarify this discrepancy, we compare our single-crystal line shapes with the powder-averaged spectra presented in Ref. [78] (see Figure 3.4 and 3.9). The sharpness of the *NN* peaks as well as their long T_2 at low temperatures indicate that the *NN* ^{17}O sites are the same defect sites found in Ref. [78]. However, as shown in Figure 3.9, the single-crystal lineshapes provide a much higher resolution of the central peak of the *NN* ^{17}O sites than the powder spectrum does for $T \leq 20$K, thereby enabling us to better identify the behavior of the *NN* Knight shift $^{17}K_{NN}^{(c)}$. Note that $^{17}K_{NN}^{(c)}$ does not level off at a positive value, as previously reported in Ref. [78] (see Figure 3.4B). Instead, it exhibits a large Curie-Weiss enhancement at low temperatures. Thus, Ref. [78] misidentified the ^{17}O NMR signals arising from the *NN* sites of the S = 1/2 Cu^{2+} defects as that from the ^{17}O sites neighboring the nonmagnetic Zn defects.

3.4 Summary

The $S = 1/2$ kagomé-lattice Heisenberg antiferromagnet herbertsmithite $ZnCu_3(OH)_6Cl_2$ is the best candidate for experimental realization of a quantum spin-liquid ground state known to date. This material displays no sign of a magnetic long-range order down to at least ~50mK. Moreover, the recent inelastic neutron scattering measurements on single-crystal samples revealed a spinon continuum in its excitation spectrum. However, almost a decade after its discovery, the true identity of the nonmagnetic ground state of $ZnCu_3(OH)_6Cl_2$ remains a mystery. The complication mostly arises from the presence of defects, whose nature has been a matter of hot debate for years. As a local probe, NMR is an ideal technique in investigating the intrinsic magnetic behavior of $ZnCu_3(OH)_6Cl_2$ under the presence of magnetic defects. The availability of single crystals also enabled us to achieve high spectral resolution in NMR measurements.

Through ^{17}O single-crystal NMR measurements at $B_{ext} = 9T \,||\, c$, we identified NMR signals arising from the nearest-neighbor *NN* ^{17}O sites of Cu^{2+} defects replacing Zn^{2+} at the interlayer sites. These *NN* ^{17}O sites account for approximately ~15% of the total integrated intensity, suggesting that the Cu^{2+}

defects occupy the interlayer Zn sites with ~15% probability. The temperature dependence of the Knight shift at the *NN* ^{17}O sites $^{17}K_{NN}^{(c)}$ is dominated by a large, negative Curie-Weiss component at low temperatures, indicating that the Cu^{2+} defect moments behave as nearly free spins. In addition, our ^{17}O single-crystal lineshapes show no evidence of the mixing of nonmagnetic Zn^{2+} onto the Cu^{2+} sites within the kagomé planes. This result eliminates the possibility of anti-site disorder being the trivial cause of the nonmagnetic ground state of $ZnCu_3(OH)_6Cl_2$.

Chapter 4

Revealing the Nature of the Ground State in $ZnCu_3(OH)_6Cl_2$

We now focus on the intrinsic properties of $ZnCu_3(OH)_6Cl_2$. As stated in previous chapters, the realization of the S=1/2 kagomé lattice in this material opens up a promising avenue to resolve the debate regarding the ground state properties of the kagomé Heisenberg antiferromagnet. Various experiments on $ZnCu_3(OH)_6Cl_2$ reported no signature of a spin gap. A critical unanswered question is whether such gapless behavior reflects the intrinsic ground state of the kagomé lattice or whether it is simply a defect-induced phenomenon. In this chapter, we present the key results of our ^{17}O NMR measurements conducted with an external magnetic field B_{ext} applied along the a^*- axis ($B_{ext} \, || a^*$), which provide us with new insights into the true identity of the ground state in $ZnCu_3(OH)_6Cl_2$.

4.1 NMR Lineshapes

For each Cu_3O_3 triangle within the kagomé lattice, B_{ext} applied along the a^*-axis forms a 60° angle with the Cu-O-Cu bond of two ^{17}O, whereas it is perpendicular to the bond of the remaining ^{17}O, as shown in Figure 4.1A. Owing to the anisotropies of the Knight shift ${}^{17}K^{(a*)}$ and the quadrupole frequency $\nu_Q^{(a*)}$, the resonance peaks arising from these inequivalent ^{17}O divide into two sets with an integrated intensity ratio of 2:1. Figure 4.1B shows the ^{17}O NMR lineshape at 295 K measured at $B_{ext} = 9T \,||\, a*$. The *Main 1* ^{17}O sites exhibit a coincidentally small value of $\nu_Q^{(a*)} \sim 8\text{kHz}$, causing all five $I_z = m$ to m+1 resonance peaks of *Main1* ^{17}O sites to merge into one; the five peaks of *Main2* ^{17}O sites are separated by $\nu_Q^{(a*)} \sim 520\text{kHz}$. Under normal circumstances, $B_{ext} \,||\, a*$ geometry is less favorable than $B_{ext} \,||\, c$ because doubling the number of resonance peaks in the ^{17}O NMR lineshapes would lower the spectral resolution and complicate the analysis. However, in this case, the bundle of *Main1* peaks possesses exceptionally large intensity and is well-resolved in the crucial temperature range below ~10 K despite the substantial line broadening, as shown in Figure 4.2. Consequently, we can directly probe the low-temperature behavior of the intrinsic spin susceptibility χ_{kagome} using the Knight shift of *Main1* ^{17}O sites ${}^{17}K_{Main1}^{(a*)}$.

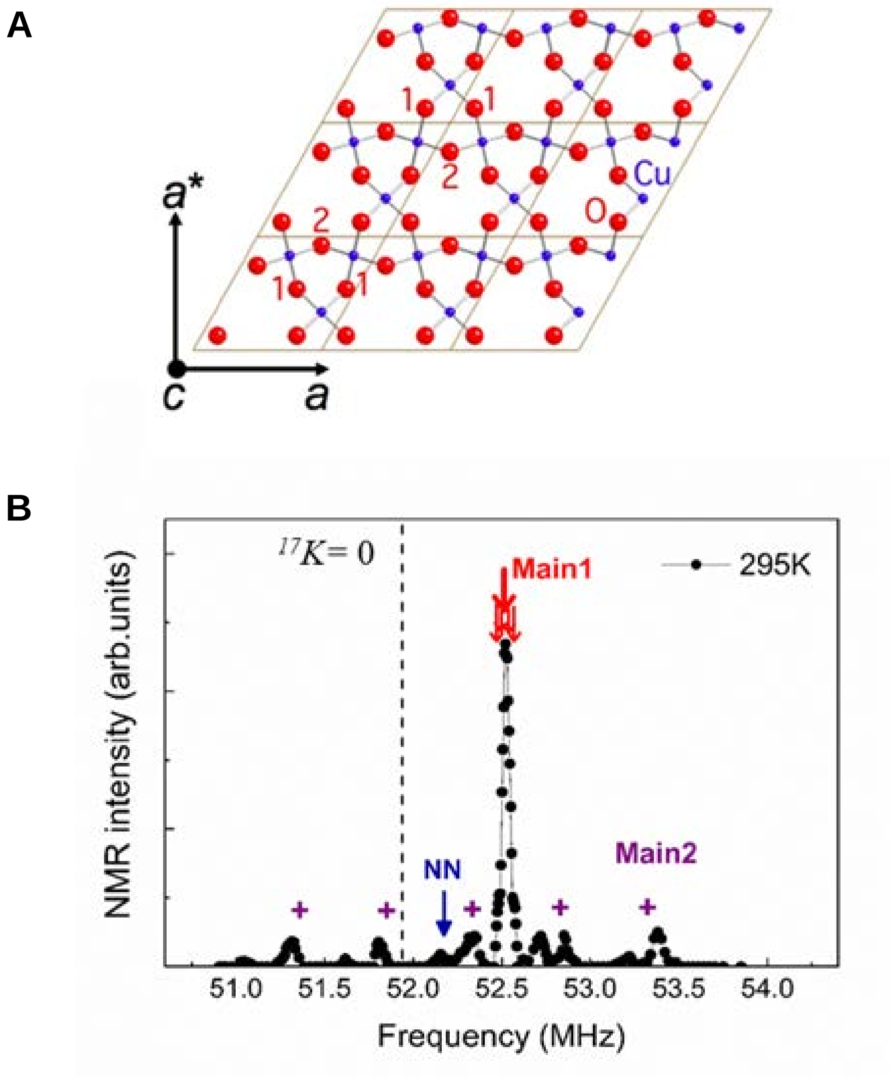

Figure 4.1. The NMR properties of the *Main1* and *Main2* ^{17}O sites for the $B_{ext} \parallel a*$ geometry. **(A)** Top view of the Cu_3O_3 kagomé plane. The presence of $B_{ext} \parallel a*$ generates two inequivalent ^{17}O sites, labelled as 1 and 2, respectively. **(B)** The room-temperature ^{17}O lineshape measured at $B_{ext} = 9T \parallel a*$. The dashed vertical line indicates the zero-shift frequency $f_0 = \gamma_N B_{ext} \sim 51.9\text{MHz}$, at which $^{17}K^{(a*)} = 0$. The five resonance peaks of the *Main1* sites (red arrows) are bundled into one

large peak owing to the very small $\nu_Q^{(a^*)} \sim 8\text{kHz}$. The five peaks of *Main2* sites (purple crosses) are separated by $\nu_Q^{(a^*)} \sim 520\text{kHz}$. The blue arrow marks the well-resolved central peak (I_z = -1/2 to +1/2) of *NN1* sites.

As mentioned in Chapter 2, we usually attempt to maximize the S/N ratio of NMR measurements by applying a strong magnetic field. Nonetheless, a high magnetic field $B_{ext} = 9T$ may induce unfavorable conditions for identifying the nature of the ground state in $ZnCu_3(OH)_6Cl_2$ for the following reasons. First, the magnetic line broadening of *Main1* and *Main2* peaks is dominated by the increasing distribution in ${}^{17}K^{(a^*)}$ at low temperatures, which is proportional to B_{ext}, whereas the magnitude of $\nu_Q^{(a^*)}$ is independent of B_{ext}. Thus, the higher the magnetic field B_{ext}, the lower is the resolution of the *Main1* and *Main2* peaks in the lineshapes (see Figure 4.2 and 4.4A). Second, once the magnetic Zeeman energy $g\mu_B SB_{ext}$ of Cu^{2+} electron spins becomes comparable to or larger than the magnitude of the spin gap, the applied B_{ext} itself may cause closure of the intrinsic spin gap, even if the gap exists at zero field, as demonstrated in Section 4.2 below. Therefore, to facilitate the observation of the intrinsic ground-state properties of the kagomé lattice, we lowered the applied field to $B_{ext} = 3.2\ T$ and measured the lineshapes again, as shown in Figure 4.4A. We emphasize that NMR measurements at such a low field are technically very challenging because the signal intensity at $B_{ext} = 3.2\ T$ is roughly an order of magnitude lower than that at $B_{ext} = 9T$.

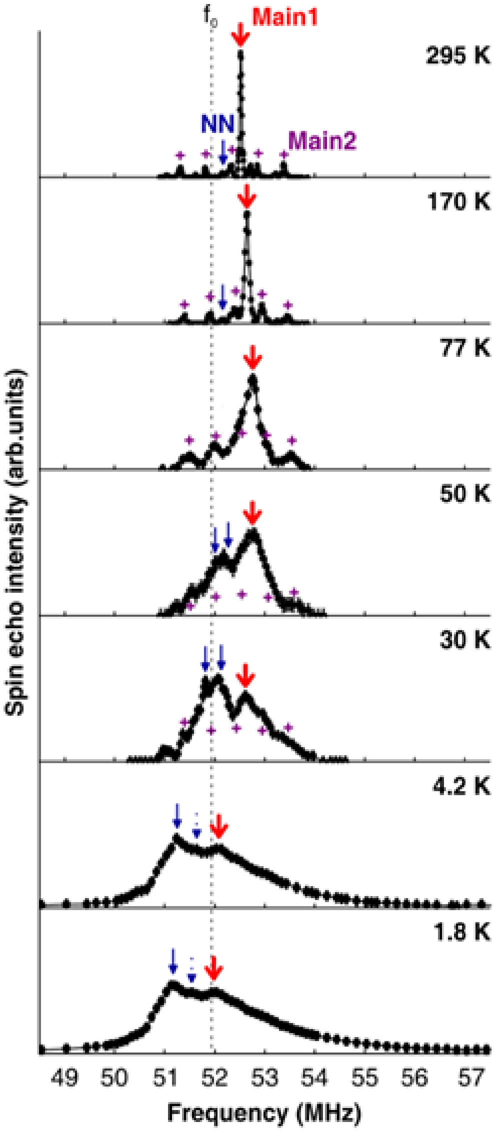

Figure 4.2. Temperature dependence of ^{17}O lineshapes measured at $B_{ext} = 9T \parallel a^*$. The dashed vertical line indicates the zero-shift frequency $f_0 = \gamma_N B_{ext} \sim 51.9$MHz. The large *Main1* peak (red arrows) is observable down to 1.8 K. The purple crosses

and blue arrows denote the approximate frequencies of the five resonance peaks of *Main2* ($\nu_Q^{(a*)} \sim 520\text{kHz}$) and the central peaks of the *NN1* (left) and *NN2* (right) sites, respectively. The magnetic line broadening induced by Cu^{2+} defects is proportional to B_{ext}; therefore, the lineshapes observed at 9 T have lower resolutions than those measured at 3.2 T, as shown in Figure 4.4A.

We obtained the lineshapes shown in Figure 4.2 and Figure 4.4A with 90°–180° RF pulse condition optimized for individual $I_z = m$ to $m+1$ NMR transitions. However, owing to the small $\nu_Q^{(a*)} \sim 8\text{kHz}$, the *Main1* peak consists of all five transitions; therefore, the optimal pulse width to detect spin-echo signals originated from the *Main1* ^{17}O sites is expected to be around 2.2 to 3 times broader than the ideal pulse width for a specific individual transition. Specifically, the 90° pulse optimized for exciting the five NMR transitions simultaneously corresponds to the ~180° pulse for the second satellite peak ($I_z = \pm 5/2$ to $\pm 3/2$) and ~270° pulse for the central ($I_z = -1/2$ to $+1/2$) and the first satellite peak ($I_z = \pm 3/2$ to $\pm 1/2$) [56]. By applying such long pulses, we succeed in isolating the unsplit *Main1* peak because over-pulsing suppresses the signals from the *Main2* and *NN* sites, as shown in Figure 4.3 and Figure 4.4B, respectively. We confirmed that the peak frequency of *Main1* determined using the long-pulse technique in Figure 4.4B agrees well with that in Figure 4.4A in the entire temperature range.

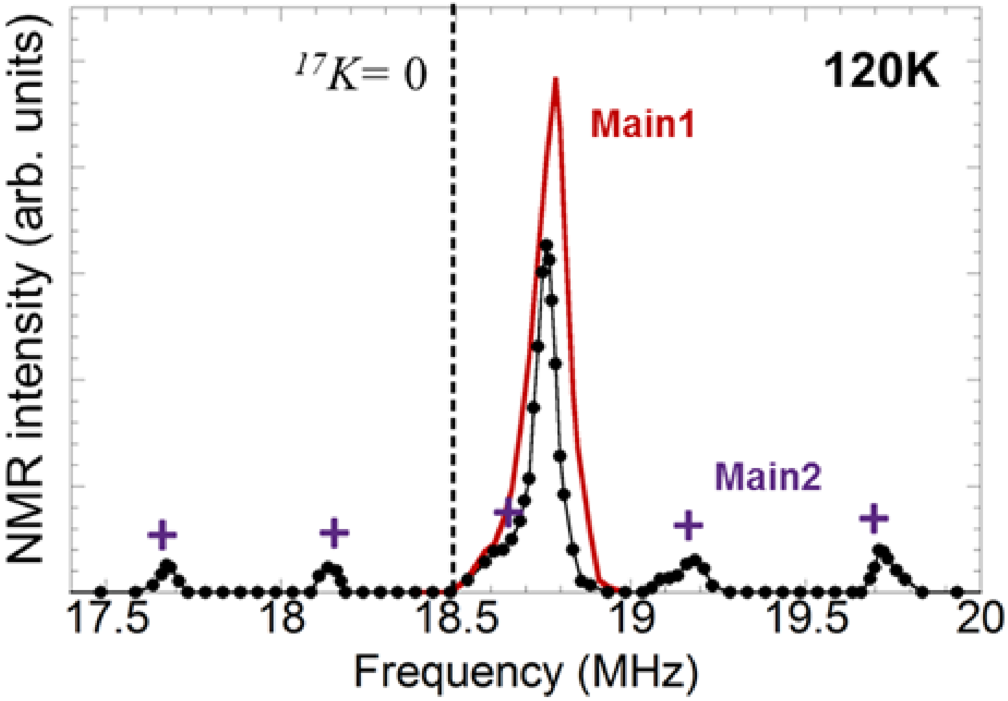

Figure 4.3. ^{17}O NMR lineshape at 120 K measured at $B_{ext} = 3.2T \parallel a^*$. The *Main1* peak is isolated with long RF pulses optimized for exciting all five transitions simultaneously (red line). Over-pulsing suppresses peaks of *Main2* (purple crosses) and the defect-induced signals that appear in the lineshape measured with optimal pulse conditions for individual $I_z = m$ *to* $m+1$ transitions (black circles).

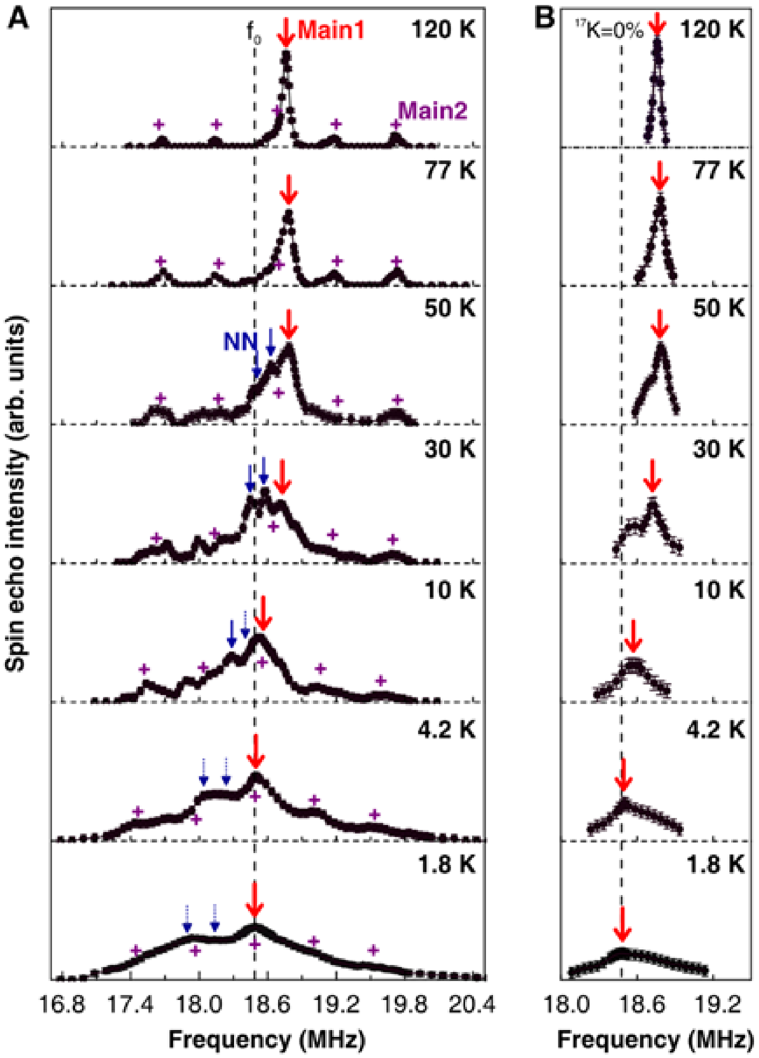

Figure 4.4. Representative ^{17}O lineshapes measured at $B_{ext} = 3.2T \parallel a*$. **(A)** ^{17}O NMR lineshapes measured with RF pulse conditions optimized for individual I_z = m to m+1 transitions. **(B)** ^{17}O NMR lineshapes measured with long RF pulses optimized to excite all five transitions of *Main1* simultaneously. Red arrows in **(B)** indicate the same *Main1* peak frequencies as those in the corresponding panels of **(A)**. The dashed vertical lines in both panels mark the zero shift-frequency $f_0 = \gamma_N B_{ext} \sim 18.5\text{MHz}$.

4.2 Knight Shift $^{17}K^{(a^*)}$

The Knight shift at the *Main1* ^{17}O sites $^{17}K_{Main1}^{(a^*)}$ provides crucial information concerning the nature of the ground state in $ZnCu_3(OH)_6Cl_2$. Figure 4.5 summarizes the temperature dependence of $^{17}K_{Main1}^{(a^*)}$ measured at $B_{ext} = 3.2T \parallel a^*$. In contrast to the bulk-averaged magnetic susceptibility χ_{bulk} (see Figure 4.3A), $^{17}K_{Main1}^{(a^*)}$ reaches a broad maximum between 50 and 100 K and then declines dramatically below T ~50 K. More importantly, $^{17}K_{Main1}^{(a^*)}$ asymptotically tends to zero below ~8K (~ 0.05 J, where J ~200 K is the Cu-Cu super-exchange energy). This feature indicates that the ground state has total spin S = 0 and the low-energy spin excitations are absent. The observed qualitative behavior of $^{17}K_{Main1}^{(a^*)}$ establishes the presence of a finite gap in the intrinsic spin excitation spectrum of $ZnCu_3(OH)_6Cl_2$. Combined with the fact that the low-temperature structural analysis based on Rietveld refinement showed no evidence of an enlarged unit cell expected for the valence bond solid (VBS) state [70], we conclude that $ZnCu_3(OH)_6Cl_2$ possesses a QSL ground state with a gapped excitation spectrum.

The central peak (I_z = -1/2 to +1/2) of the *Main2* ^{17}O sites overlaps with the large *Main1* peak, which hinders the accurate measurement of $^{17}K_{Main2}^{(a^*)}$ at *Main2* sites. However, the uppermost second satellite peak (I_z = ±5/2 to ±3/2) near 19.8MHz is resolvable down to 4.2 K; its frequency shift qualitatively exhibits the same temperature dependence as that of the *Main1* peak, as shown in Figure 4.4A and Figure 4.6. The frequency shift of the second satellite peak may also depend on $\nu_Q^{(a^*)}$, which is independent of temperature within experimental uncertainty (see Figure 5.2). Therefore, Figure 4.6 suggests the consistent behavior of $^{17}K^{(a^*)}$ at *Main1* and *Main2* ^{17}O sites.

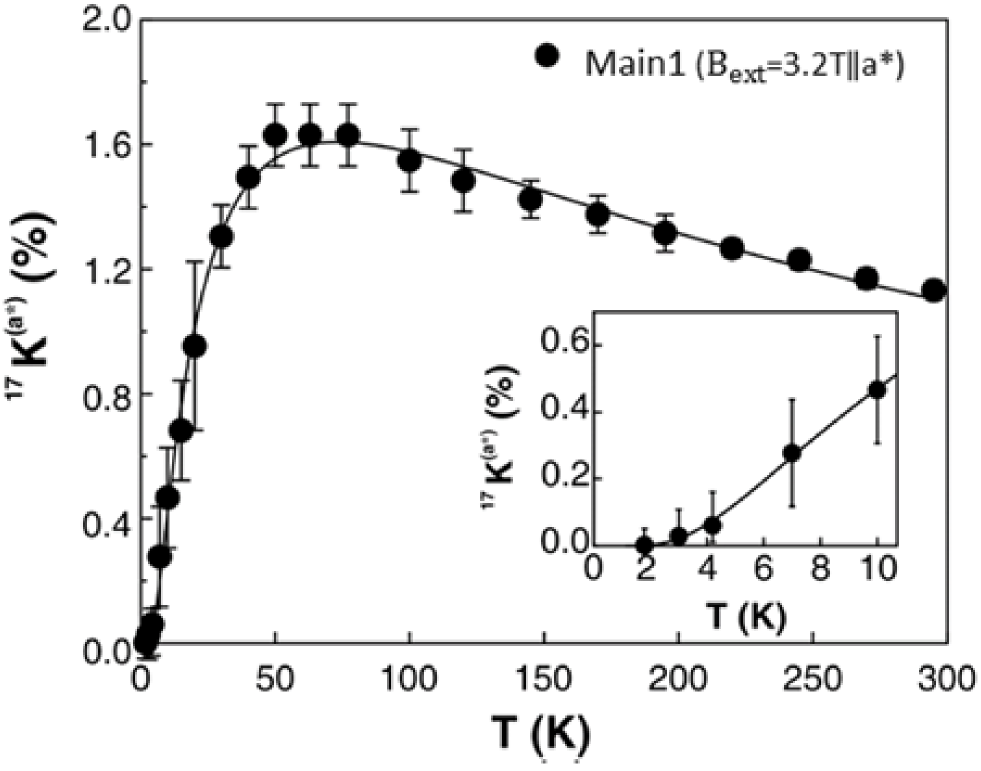

Figure 4.5. Temperature dependence of Knight shift $^{17}K_{Main1}^{(a^*)}$ at *Main1* ^{17}O sites in $B_{ext} = 3.2T \parallel a^*$; $^{17}K_{Main1}^{(a^*)}$ reflects the behavior of the intrinsic spin susceptibility χ_{kagome}. The solid curve is a guide for the eyes. Inset: Magnification of the low-

temperature region ($T \leq 10\text{K}$) of the same plot. Fitting ${}^{17}K^{(a*)}_{Main1}$ data in the temperature range $T \leq 10\text{K}$ to the empirical formula ${}^{17}K^{(a*)}_{Main1} \sim T \cdot exp(-\Delta / T)$ yields a gap $\Delta \sim 6.8\text{K}$ (solid line).

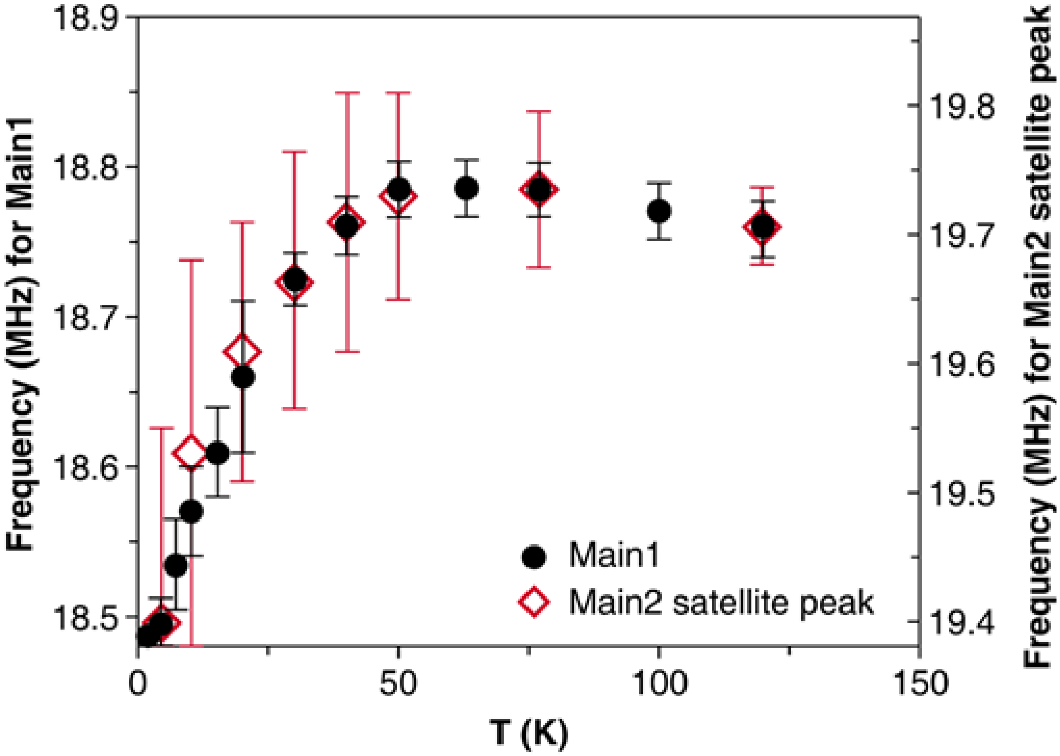

Figure 4.6. Temperature dependence of the *Main1* peak frequency (black circles) compared with the frequency of the uppermost satellite peak of *Main2* ^{17}O sites (red diamonds).

To estimate the magnitude of the gap Δ, we fitted ${}^{17}K_{Main1}^{(a*)}$ below 10 K to the empirical formula

$$ {}^{17}K^{(a*)} \sim T \cdot exp\,(-\frac{\Delta}{T}). \tag{4.1}$$

This fit provides Δ ~ 6.8 K at $B_{ext} = 3.2\ T$, as shown in the inset of Figure 4.5. The constant background term arising from the chemical shift ${}^{17}K_{chem}$ is typically negligibly small $(\sim \pm 0.02\%)$ at ^{17}O sites in copper oxides [91-94], and therefore, it does not affect the estimated Δ. With a pre-factor T, the fitting function (Eq. 4.1) phenomenologically takes into account the decline of the spin susceptibility resulting from the effects of antiferromagnetic spin correlations, which is irrelevant to the low-temperature gap behavior. In addition, the same pre-factor T emerges for the uniform Pauli spin susceptibility of spinon excitations in the gapped Dirac Fermion model [35, 90], as discussed in more detail in Section 4.3.

The Knight shift ${}^{17}K_{Main1}^{(a*)}$ measured at $B_{ext} = 9T \parallel a*$ is identical to that measured at $B_{ext} = 3.2\ T \parallel a*$ except for the low-temperature regime $T \leq$ 10K, where ${}^{17}K_{Main1}^{(a*)}$ declines almost linearly and exhibits finite magnitude even below ~5 K (Figure 4.7 and 4.9A). In fact, as shown in Figure 4.8, lowering B_{ext} causes the peak frequency of *Main1* to shift toward ${}^{17}K^{(a*)} = 0$ at low temperatures. This feature indicates that ${}^{17}K_{Main1}^{(a*)}$ shows a systematic dependence on the magnetic field strength B_{ext}.

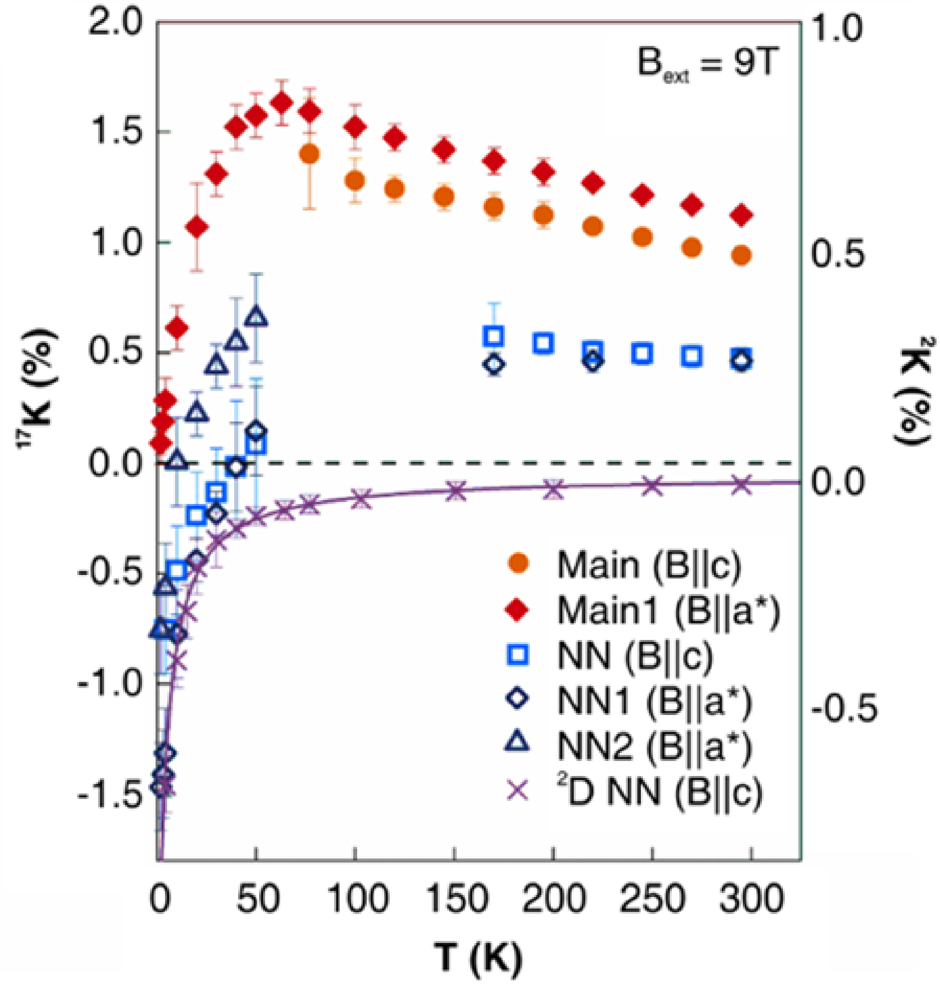

Figure 4.7. A summary of $^{17}K^{(a*)}$ and $^{17}K^{(c)}$ data measured at $B_{ext} = 9\text{T}$. The filled and open symbols represent the data for the *Main* (or *Main1*) and *NN* (or *NN1* and *NN2*) sites, respectively. Below ~50 K, $^{17}K^{(a*)}_{Main1}$ (filled diamonds) declines sharply to a small finite value of ~0.1% at 1.8 K. $^{17}K^{(c)}_{NN}$ (open squares), $^{17}K^{(a*)}_{NN1}$ (open diamonds), and $^{17}K^{(a*)}_{NN2}$ (open triangles) all become increasingly negative with decreasing temperature, similar to the low-T behavior of $^{2}K^{(c)}$ at *NN* ^{2}D sites

(crosses) observed at $B_{ext} = 8.4\mathrm{T}$. The solid curve is a Curie-Weiss fit with Weiss temperature $\theta \sim -1.2\mathrm{K}$.

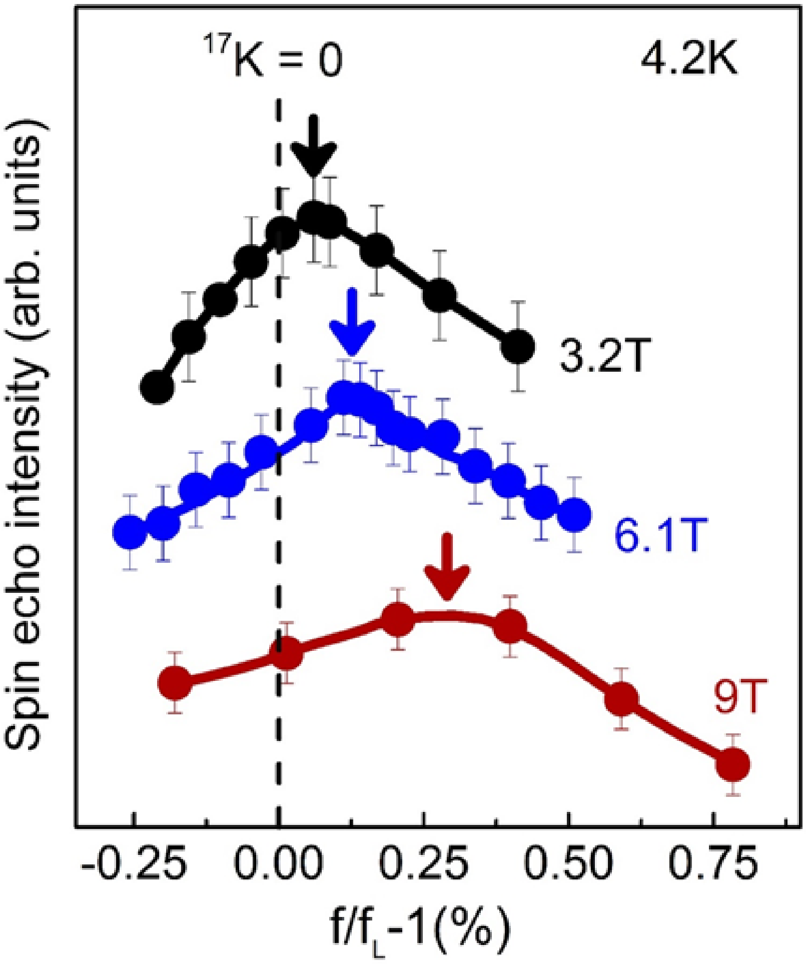

Figure 4.8. The *Main1* peak at 4.2 K at B_{ext} = 3.2, 6.1, and 9 T plotted as a function of the normalized frequency $f/f_L - 1$ $(= {}^{17}K^{(a^*)})$. The downward errors mark the peak frequencies at which ${}^{17}K^{(a^*)}$ is estimated for the three field values.

In Figure 4.9A, we summarize the low-temperature behavior of ${}^{17}K_{Main1}^{(a*)}$ observed at three different fields of 3.2, 6.1, and 9 T. By fitting the ${}^{17}K_{Main1}^{(a*)}$ data at various B_{ext} in Figure 4.9A with ${}^{17}K^{(a*)} \sim T \cdot exp\left(-\Delta/T\right)$, we deduced the field dependence of the gap size $\Delta\left(B_{ext}\right)$ as a function of B_{ext}, as shown in Figure 4.9B. We also confirmed that reducing the upper bound of the fitting range from 10 to 4.2 K does not alter the estimated $\Delta\left(B_{ext}\right)$. With increasing magnetic field, $\Delta\left(B_{ext}\right)$ diminishes linearly following the relation $\Delta\left(B_{ext}\right) = \Delta(0) - g\mu_B S B_{ext}$ [88], where the Landé g-factor of the kagomé Cu^{2+} spins is $g \simeq 2.2$ [89], and μ_B is the Bohr magneton; we expect S = 1/2 for the single-spinon excitations and S = 1 for the spin-triplet or two bound-spinon excitations. From the best linear fit with free parameters, we estimated the zero-field gap, Δ(0)=10±3K, namely, $\Delta(0)/J$ = 0.03~0.07. This result is consistent with the theoretical prediction, $\Delta(0)/J \sim 0.1$, based on the most recent density-matrix renormalization group (DMRG) calculations [33, 34]. Extrapolating this linear fit to intercept the horizontal axis yields a critical field $B_c \sim 9T$ at which the spin gap is suppressed completely. Owing to the large uncertainties in the estimated values of $\Delta\left(B_{ext}\right)$, we were unable to definitively determine the total spin of the excited state, $S = 1/2$ or $S = 1$, from the slope of the linear fit.

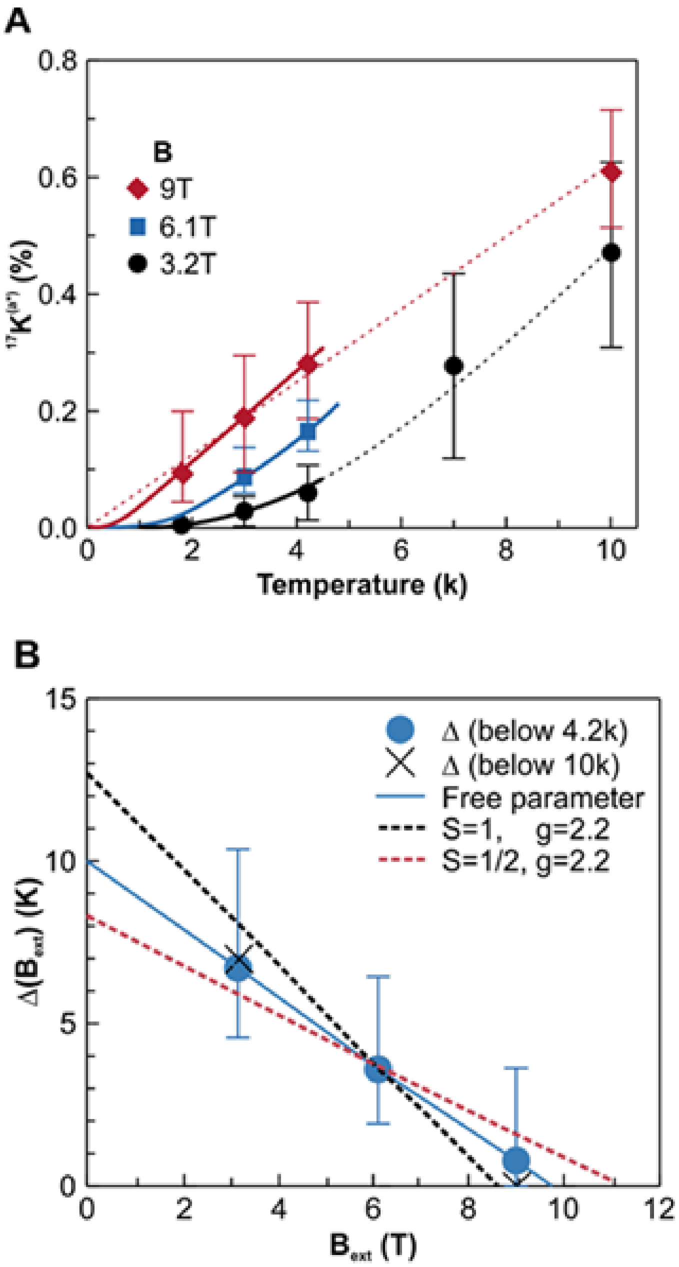

Figure 4.9. The intrinsic spin susceptibility χ_{kagome} deduced from $^{17}K^{(a^*)}_{Main1}$ at various values of B_{ext} and spin gap Δ. **(A)** The low-temperature behavior of $^{17}K^{(a^*)}_{Main1}$ at $B_{ext} = 3.2\text{T}$, 6.1 T, and 9 T, with fits to $^{17}K^{(a^*)} \sim T \cdot exp(-\Delta/T)$ for the

temperature range $T \leq 4.2\text{K}$ (solid curves) and $T \leq 10\text{K}$ (dashed curves). **(B)** The spin gap $\Delta\left(B_{ext}\right)$ deduced from **(A)** for the fitting range $T \leq 4.2\text{K}$ (circles) and $T \leq 10\text{K}$ (crosses). The solid curve represents the best linear fit with free parameters; also included are the linear fits with the constraint of $S = 1$ (black dashed line) and $S = 1/2$ (red dashed line), respectively.

Figure 4.10 shows an alternative method to analyze the low-temperature ${}^{17}K_{Main1}^{(a*)}$ data using a simple exponential function

$$ {}^{17}K^{(a*)} \sim exp\,(-\frac{\Delta}{T}). \tag{4.2} $$

The fit provides a larger zero-field gap Δ(0) = 17±3K; nonetheless, it does not change the qualitative properties of the gapped state. Therefore, our fundamental conclusion for the presence of a finite gap in the spin excitation spectrum is independent of the details of the analysis.

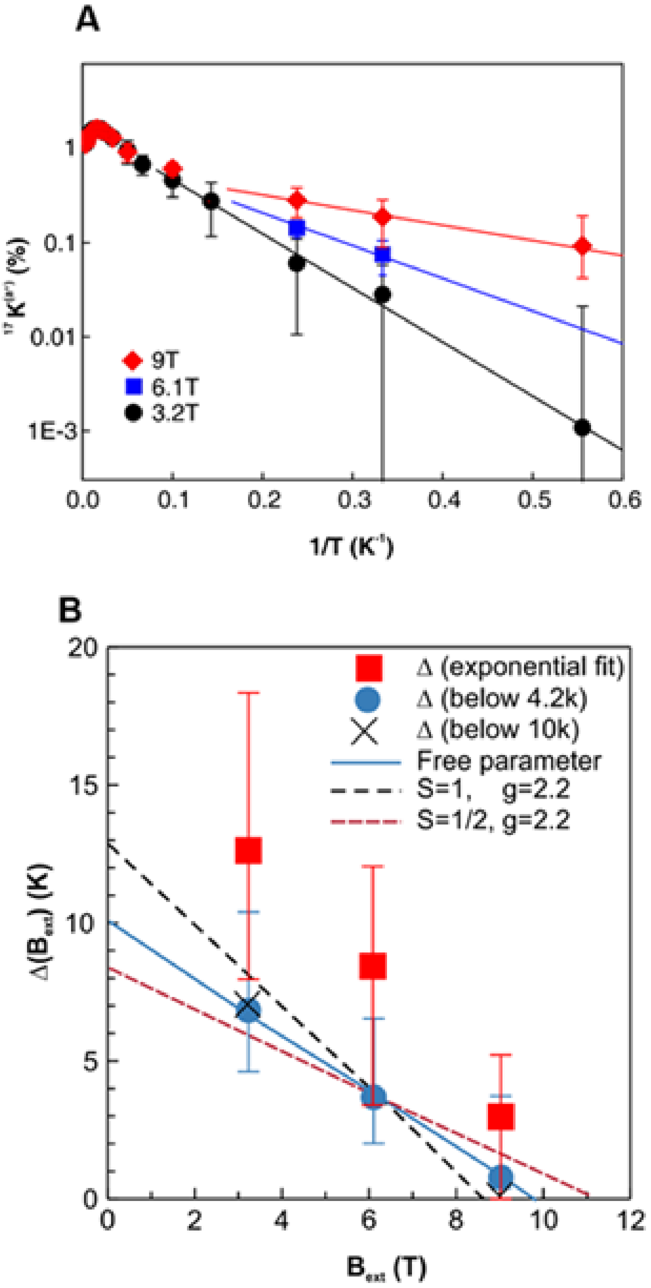

Figure 4.10. An alternative method for estimating the spin gap Δ. **(A)** The low-temperature behavior of $^{17}K^{(a*)}_{Main1}$ at $B_{ext}=3.2$T, 6.1 T, and 9 T with single exponential fits $^{17}K^{(a*)}\sim exp(-\Delta/T)$ (solid lines). **(B)** The spin gap $\Delta(B_{ext})$

extracted from the exponential fits in **(A)** (squares) compared with $\Delta\left(B_{ext}\right)$ estimated from the empirical fit ${}^{17}K^{(a^*)} \sim T \cdot exp\,(-\Delta/T)$ shown in Figure 4.9B.

4.3 Knight Shift ${}^{17}K$ of Gapped Dirac Fermions

In this section, we present the theoretical calculations for the ^{17}O Knight shift ${}^{17}K$ in the framework of the gapped Dirac Fermion model [35, 90], which provides a theoretical justification for including the pre-factor T in the empirical fitting function (Eq. 4.1).

The dispersion relation of gapped Dirac Fermions is given by

$$E_k = \sqrt{(vk)^2 + \Delta^2}, \tag{4.3}$$

where v is the velocity of the Dirac Fermion and $\mathbf{k}$, the wave vector. This expression implies that the energy E increases linearly with $|\mathbf{k}|$, forming a Dirac cone in the 2D $\mathbf{k}$-space, as shown in Figure 4.11A. For notational simplicity, we consider the Dirac cone centered at $\mathbf{k} = 0$ for calculating the uniform spin susceptibility χ_{spin}. We note that the resulting expression of χ_{spin} is also valid for $\mathbf{k} \neq 0$. We then derive the density of states $g(E)$ based on Eq. 4.3 such that

$$\frac{kdk}{2\pi} = \frac{E_k}{2\pi v^2} dE_k = g(E) dE_k. \tag{4.4}$$

Similar to the case of Pauli paramagnetism in conventional metals, the energy E_k of the Dirac Fermion is raised or lowered depending on its spin orientation in the presence of a finite magnetic field *B*, as shown in Figure 4.11B; the separation between the two energy bands is $g\mu_B B$, namely,

$$E_\uparrow = E_k + \frac{1}{2} g\mu_B B, \tag{4.5a}$$

$$E_\downarrow = E_k - \frac{1}{2} g\mu_B B. \tag{4.5b}$$

Thus, the uniform magnetization *M* is given by

$$\begin{aligned} M(B) &= -\frac{1}{2} g\mu_B (n_\uparrow - n_\downarrow) \\ &= -\frac{1}{2} g\mu_B \int_0^\infty \frac{kdk}{2\pi} [f(E_{k\uparrow}) - (E_{k\downarrow})], \end{aligned} \tag{4.6}$$

where $f(E) = 1/(\mathrm{e}^{E/k_B T} + 1)$ is the Fermi-Dirac distribution function, and we set the Boltzmann constant as $k_B = 1$ for simplicity. This analytic formula was provided to us by P. A. Lee [90]. By substituting Eqs. 4.4 and 4.5 into Eq. 4.6, we evaluated $M(B)$ numerically using the following expression:

$$M \propto [\int_\Delta^\infty x \cdot dx(\frac{1}{\mathrm{e}^{(x-\delta)/T} + 1}) - \int_\Delta^\infty y \cdot dy(\frac{1}{\mathrm{e}^{(y+\delta)/T} + 1})], \tag{4.7}$$

where we set $\delta = 1/2\, g\mu_B B$, $x = E_\downarrow + \delta$, and $y = E_\uparrow - \delta$. The resulting temperature dependence of $M(B)$ at various field values *B* ($b \equiv B/\Delta = 0.01 \sim 0.99$, and $\Delta = 1$) is shown in Figure 4.12.

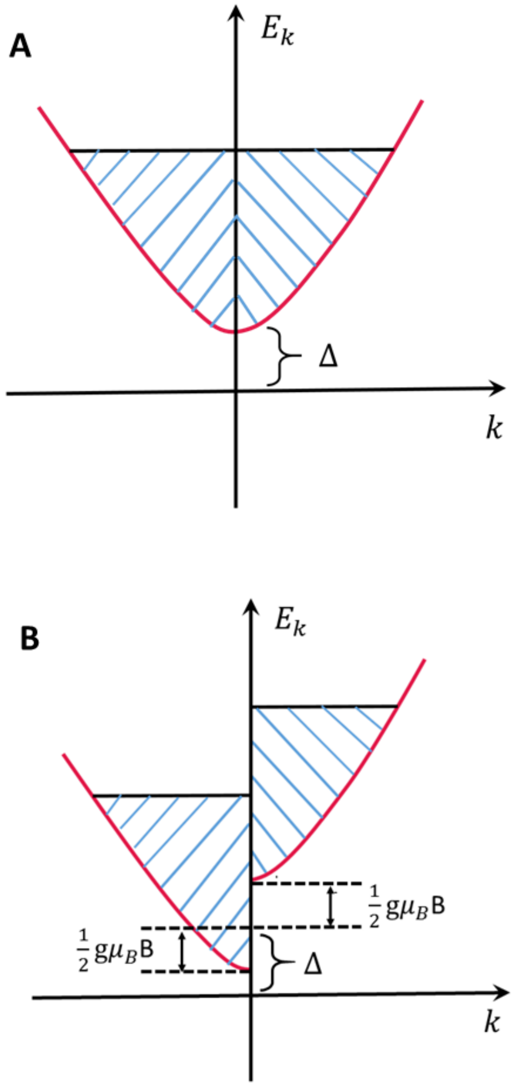

Figure 4.11. Schematic diagram of the dispersion relation for Dirac Fermions with a spin gap Δ. **(A)** In the absence of a magnetic field B, all the Dirac Fermions possess equal energy E_k. **(B)** With finite B, the energy E_k of the Dirac Fermion is spin-split into two levels separated by $g\mu_B B$.

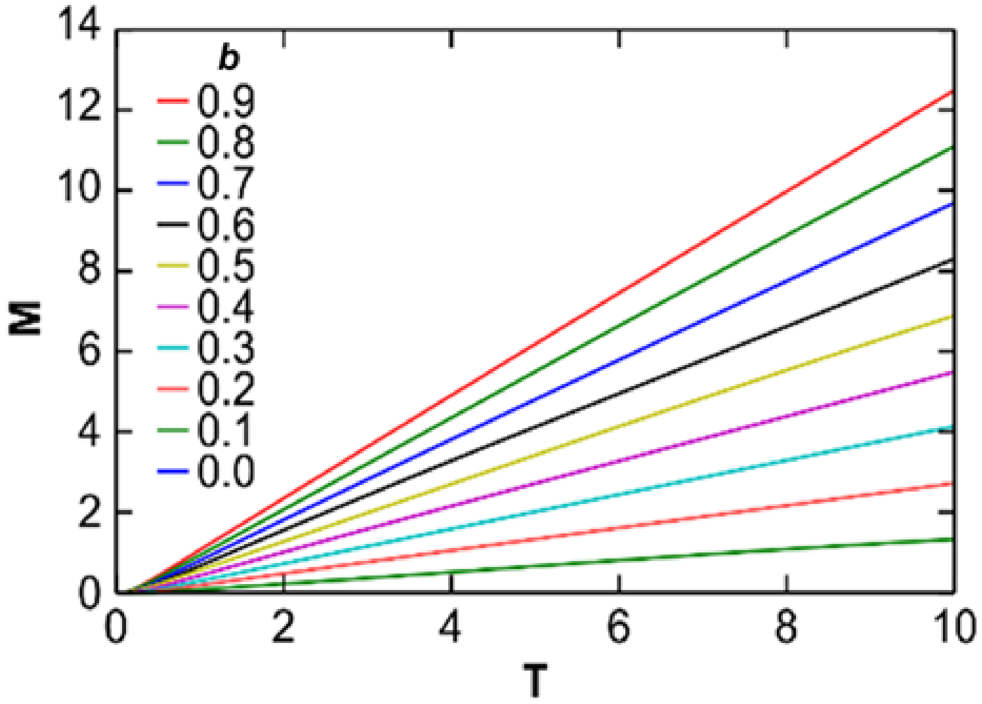

Figure 4.12. Temperature and field dependence of the magnetization $M(B)$ resulting from spinon excitations in the gapped Dirac Fermion model. The magnetic field value is defined as $b \equiv B/\Delta$, where $\Delta = 1$.

As mentioned in Chapter 2, ^{17}K is proportional to the uniform spin susceptibility χ_{spin} of the Cu^{2+} electrons near the ^{17}O sites of interest, and $\chi_{spin} \propto M/B$. Accordingly, the temperature dependence of ^{17}K at various field values B is represented by that of M/B, as shown in Figure 4.13. It should be noted that ^{17}K shows strong field dependence in the low-temperature regime because increasing the magnetic field strength reduces the magnitude of the gap Δ. In the limit of $B \ll \Delta$ and $T \ll \Delta$, it is straightforward to analytically show that χ_{spin} of the gapped Dirac Fermions becomes [90]

$$\chi_{spin} = \frac{dM}{dB} \sim T \cdot exp\,(-\Delta/T). \tag{4.8}$$

In other words, Eq. 4.8 provides a theoretical justification for the empirical fitting formula $^{17}K \sim T \cdot exp(-\Delta / T)$ applied for the data analysis in Figure 4.5 and 4.9.

However, in our NMR measurements, the applied field strength B does not always satisfy the limit $B \ll \Delta$. To assess the viability of the empirical fit for a wide range of B (or $b \equiv B/\Delta$), we summarize the low-temperature behavior of $M/b\,(\propto {}^{17}K)$ as calculated numerically from Eq. 4.8 in Figure 4.14A; Figure 4.14A also shows the empirical fits of M/b such that $M(b)/b \sim T \cdot exp\,(-\Delta/T)$ for $T \leq 0.3\Delta$ (solid lines). We then compare the fitted values of the gap Δ_{fit} (purple diamonds) with the theoretically expected linear field dependence, as indicated by the solid curve in Figure 4.14B. The fitted gap values Δ_{fit} agree well with the theoretical prediction for $b \geq 0.2$. In the entire b range of 0.01–0.99, the deviation between Δ_{fit} and the theoretical values is less than ~20%, which is insignificant compared with the experimental uncertainty of $\Delta\left(B_{ext}\right)$ in Figure 4.9. Recall that we obtained $^{17}K^{(a^*)}$ data at 3.2, 6.1, and 9 T, which correspond to b ~0.36, 0.67, and 1, respectively. Therefore, the low-temperature behavior of ^{17}K derived from the gapped Dirac Fermion model can be approximated very well by the empirical formula $^{17}K \sim T \cdot exp\,(-\Delta/T)$ in the entire range of parameters that is relevant to our experiments.

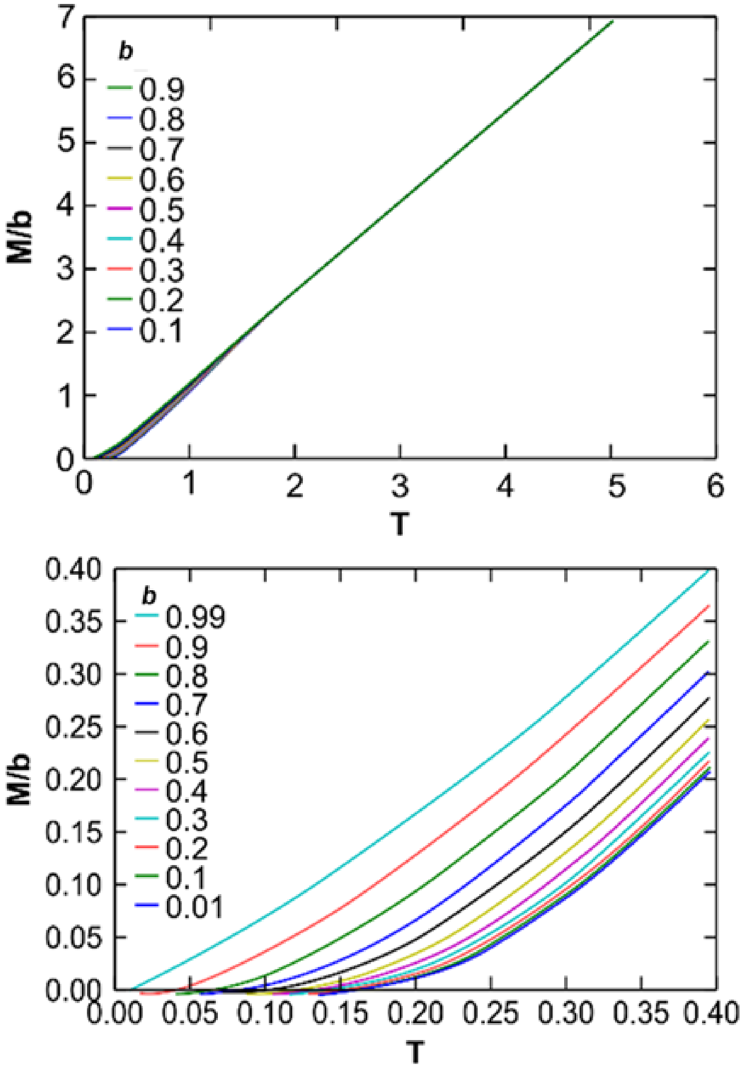

Figure 4.13. Temperature dependence of M/b ($\propto {}^{17}K$) for the gapped Dirac Fermions for various applied fields b. **(A)** M/b becomes field-dependent at low

temperatures owing to the suppression of the gap Δ with increasing field strength b. **(B)** Magnification of the low-temperature region $(T \leq 0.4\Delta)$ of **(A)**.

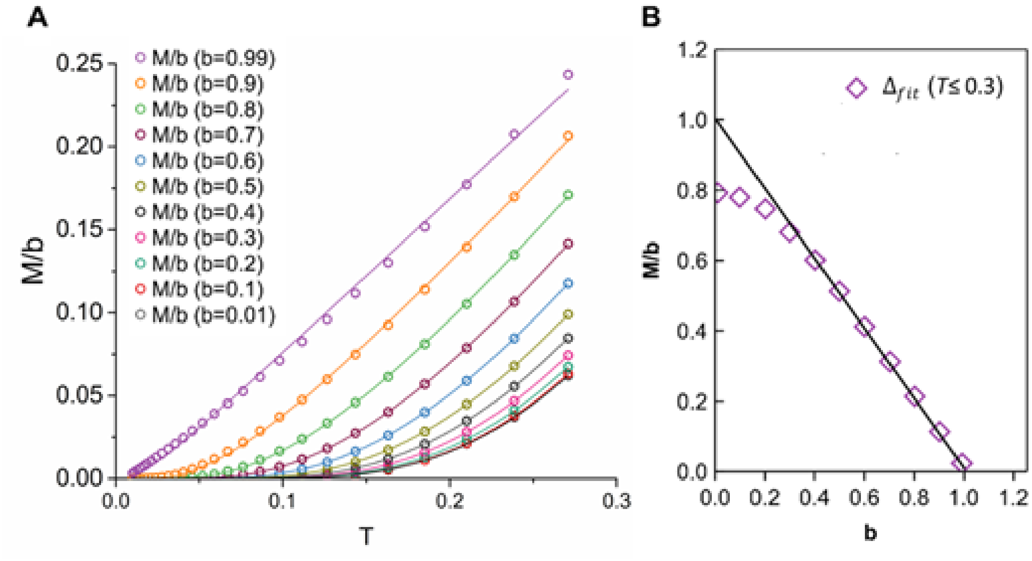

Figure 4.14. A theoretical justification for the empirical fitting function ${}^{17}K \sim T \cdot exp(-\Delta/T)$. **(A)** The low-temperature behavior of M/b at various field values b with fits to the empirical formula $M(b)/b \sim T \cdot exp(-\Delta/T)$ in the temperature range $T \leq 0.3\Delta$ (solid curves). **(B)** A comparison of the spin gap Δ_{fit} deduced from **(A)** (open diamonds) with the expected linear field dependence (solid line).

4.4 Spin-lattice Relaxation Rate $^{17}1/T_1$

To probe the intrinsic low-energy spin fluctuations of the kagomé Cu^{2+} electron spins, we measured the ^{17}O nuclear spin-lattice relaxation rate $^{17}1/T_1$ at the *Main2* ^{17}O sites in $B_{ext} \parallel a^*$ and at the *Main* ^{17}O sites in $B_{ext} \parallel c$. As mentioned in Chapter 2, we typically obtain the $^{17}1/T_1$ data by fitting the recovery of the nuclear magnetization M to the standard form:

$$M(t) = M_0 - A\sum_{j=1}^{5} a_j \, exp\left(-\frac{b_j t}{T_1}\right). \tag{4.9}$$

This fitting function contains three free parameters $M(\infty)$, A, and $^{17}1/T_1$. While all the NMR transitions for $I_z = 5/2$ are characterized by a unique set of transition rates (b_1, b_2, b_3, b_4, b_5) = ($15, 10, 6, 3, 1$), the fitting functions of these transitions involve different sets of coefficients a_j (see Appendix A for the derivation of the standard fitting forms for $I = 5/2$).

In general, the central peak ($I_z = -1/2$ to $+1/2$) shows the strongest intensity and thereby provides the best S/N ratio. However, the second satellite peak ($I_z = \pm 5/2$ to $\pm 3/2$) is more advantageous for accurate measurements of $^{17}1/T_1$ at the *Main2* (or *Main*) ^{17}O sites. Figure 4.15 presents a comparison of the signal recovery for the central and the second satellite peaks observed at 295 K in $B_{ext} = 9T \parallel c$. For the central $I_z = -1/2$ to $+1/2$ transition, the standard fitting function of the T_1 recovery curve is given by

$$M(t)=M(\infty)-A\cdot\left[0.7936\cdot exp\left(-\frac{15t}{T_1}\right)+0.1778\cdot exp\left(-\frac{6t}{T_1}\right)+0.0286\cdot exp\left(-\frac{t}{T_1}\right)\right]. \tag{4.10}$$

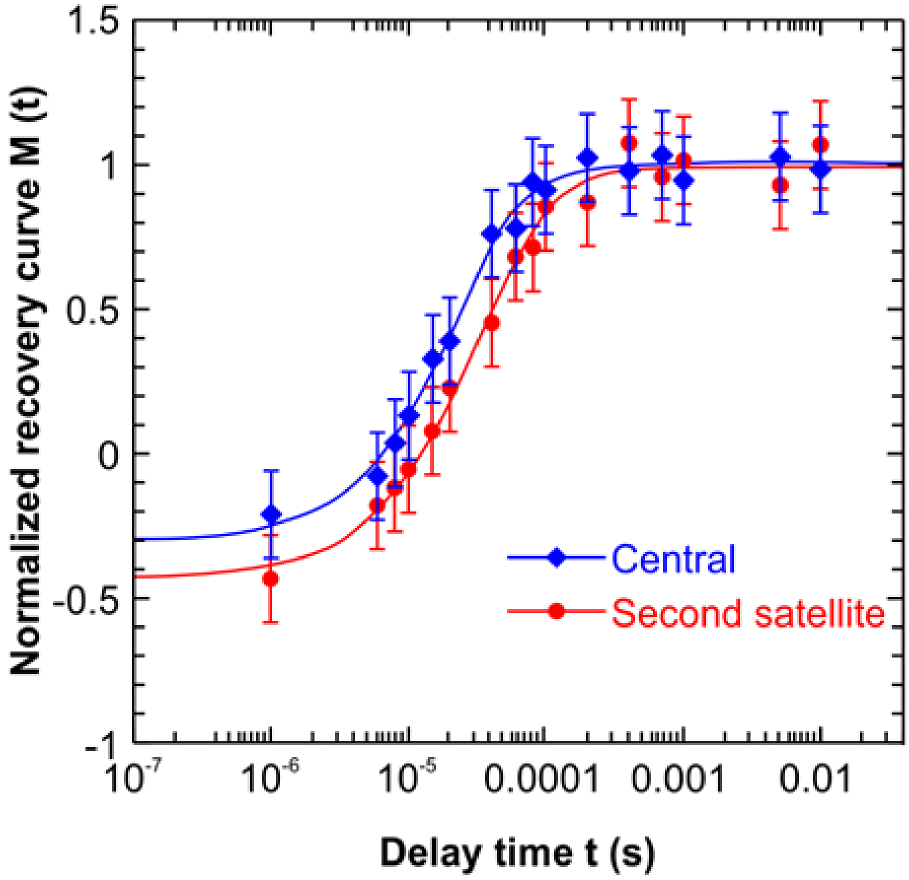

Figure 4.15. A comparison of T_1 recovery curves observed for the central peak (diamonds) and the second satellite peak (circles) of ^{17}O *Main* sites at 295 K at $B_{ext}=9T\parallel c$. The solid lines represent the best fit to the standard formulas, which provide $^{17}1/T_1\sim3100s^{-1}$ for the central transition; this is ~25% less than the value obtained for the second satellite transition, $^{17}1/T_1\sim3880s^{-1}$.

It should be noted that the T_1 recovery process of the central peak is dominated by the fastest normal mode $0.7936 \cdot exp\left(-15t/T_1\right)$; as a result, when the value of $^{17}1/T_1$ exceeds $\sim 2\times10^3\, s^{-1}$, accurate measurements of $^{17}1/T_1$ using the central peak become difficult because the signal begins to recover at a time scale comparable to the duration of the RF pulse itself. Unlike the central transition, the T_1 recovery of the second satellite peak is governed by slower normal modes, such that

$$\frac{M(t)}{M(\infty)} = 1 - \left[0.0714 \cdot exp\left(-\frac{15t}{T_1}\right) + 0.2857 \cdot exp\left(-\frac{10t}{T_1}\right) + 0.4 \cdot exp\left(-\frac{6t}{T_1}\right) \right. \\ \left. +0.2143 \cdot exp\left(-\frac{3t}{T_1}\right) + 0.0286 \cdot exp\left(-\frac{t}{T_1}\right) \right]. \tag{4.11}$$

This feature allows sufficient inversion of signals even for the fast $^{17}1/T_1$. Moreover, as the difference among the transition rates b_j can be as large as a factor of 15, the superposition of NMR peaks arising from distinct transitions will prevent us from fitting the signal recovery properly using the standard formulas. Therefore, only the isolated uppermost satellite peak of the *Main2* (or *Main*) ^{17}O sites provides reliable $^{17}1/T_1$ data. Here, all the $^{17}1/T_1$ data shown in Figure 4.17 are measured at the uppermost second satellite peak of the *Main2* ^{17}O sites (or the *Main* sites at $B_{ext} = 9T \parallel c$) and are estimated using the standard fitting form (Eq. 4.11).

As shown in Figure 4.17, $^{17}1/T_1$ data acquired in the $9T \parallel c$ and $9T \parallel a^*$ geometries display qualitatively the same temperature dependence from 295 K down to 77 K, below which the uppermost second satellite peak is no longer resolvable at 9 T. Fortunately, we could resolve the second satellite peak of *Main2* ^{17}O sites down to 4.2 K at $B_{ext} = 3.2T \parallel a*$, as shown in Figure 4.4A. The extremely weak signal intensity at $3.2T \parallel a*$ obstructed accurate $^{17}1/T_1$ measurements above ~130 K; nonetheless, we confirmed that at 77 and 120 K, the magnitude of $^{17}1/T_1$ obtained at $3.2T \parallel a*$ agrees well with the value obtained at $9T \parallel a*$, indicating that $^{17}1/T_1$ is independent of the field strength above 77 K.

Below ~60 K, $^{17}1/T_1$ measured at $B_{ext} = 3.2\ T \parallel a*$ exhibits a sharp decline, which is qualitatively consistent with the gap behavior observed for $^{17}K^{(a*)}$ (see Figure 4.17). However, $^{17}1/T_1$ does not approach zero below ~5 K but levels off at a small finite value. Such a small constant contribution may be attributed to the residual spin fluctuations induced by the defect Cu^{2+} magnetic moments. Owing to the random occupancy of these Cu^{2+} defects at the Zn^{2+} interlayer sites, the resulting relaxation rate shows a substantial distribution; consequently, the T_1 recovery data observed below ~15 K at $B_{ext} = 3.2\ T \parallel a*$ exhibits obvious deviations from the standard fitting formula (Eq. 4.11), as shown in Figure 4.16A, whereas for $T \gtrsim 15K$, the T_1 recovery data can be fitted reasonably well with the standard form. Therefore, we attempted stretched exponential fits to estimate the $^{17}1/T_1$ values for T < 15K at $B_{ext} = 3.2\ T \parallel a*$, namely,

$$M(t) = M(\infty) - A\sum_{j=1}^{5} a_j \, exp\left(-\frac{b_j t}{T_1}\right)^{\beta} . \tag{4.12}$$

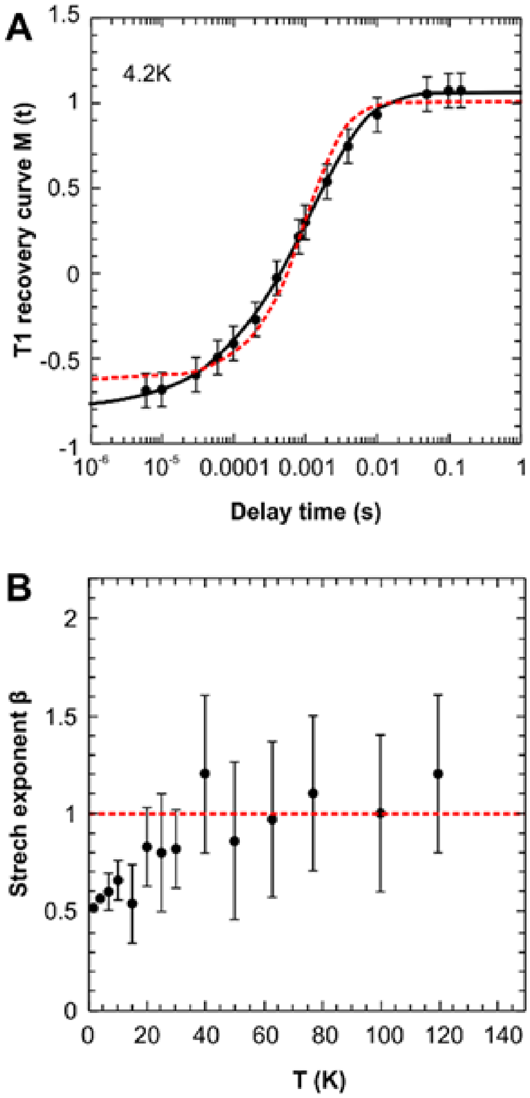

Figure 4.16. Stretched exponential fit of T_1 recovery for the uppermost second satellite peak of *Main2* ^{17}O sites. **(A)** T_1 recovery observed for the second satellite peak of *Main2* ^{17}O sites at 4.2 K in $B_{ext} = 3.2\ T \parallel a*$, with fits to the stretched

exponential formula (solid line) and standard form (dashed line). **(B)** Temperature dependence of the stretched exponent β at $B_{ext} = 3.2\ T \parallel a^*$.

The stretching exponent β reflects the underlying distribution of ${}^{17}1/T_1$. As shown in Figure 4.16B, the resulting fitted value of β approaches 1 as the temperature increases, implying vanishing distribution of ${}^{17}1/T_1$ at the *Main2* ^{17}O sites. Moreover, we confirmed that the ${}^{17}1/T_1$ values obtained using the stretched exponential fit are identical to that provided by the standard fitting function within an uncertainty of ~ ±10% for the entire temperature range.

As discussed in Chapter 2, ${}^{17}1/T_1$ is related to the imaginary part of the dynamical electron spin susceptibility χ'' at the NMR resonant frequency f_{NMR} (~51.9 MHz for 9 T and ~18.5 MHz for 3.2 T), which is

$$1/T_1 \sim T\sum_{\boldsymbol{q}}\left|A_{hf}\right|^2 \chi''(q, f_{NMR}) \tag{4.12}$$

In this expression, $A_{hf}(\mathbf{q})$ is the hyperfine form factor, and the wave vector $\mathbf{q}$ summation is taken over the first Brillouin zone. In Sections 4-2 and 4-3, we showed that it is reasonable to describe the low-temperature behavior of χ_{spin} using the function $T \cdot exp\,(-\Delta/T)$. If we assume $\chi'' \sim T \cdot \exp(-\Delta/T)$, we may write the intrinsic contribution of the spin fluctuations within the kagomé plane as $\left({}^{17}1/T_1\right)_{kagome} \sim T^2 \cdot \exp(-\Delta/T)$. Taking into account the constant background arising from the defect spin fluctuations $({}^{17}1/T_1)_{defect}$, we fitted ${}^{17}1/T_1$ below ~15 K to the empirical formula

$$ {}^{17}1/T_1 \sim T^2 exp(-\Delta/T) + ({}^{17}1/T_1)_{defect}. \tag{4.13}$$

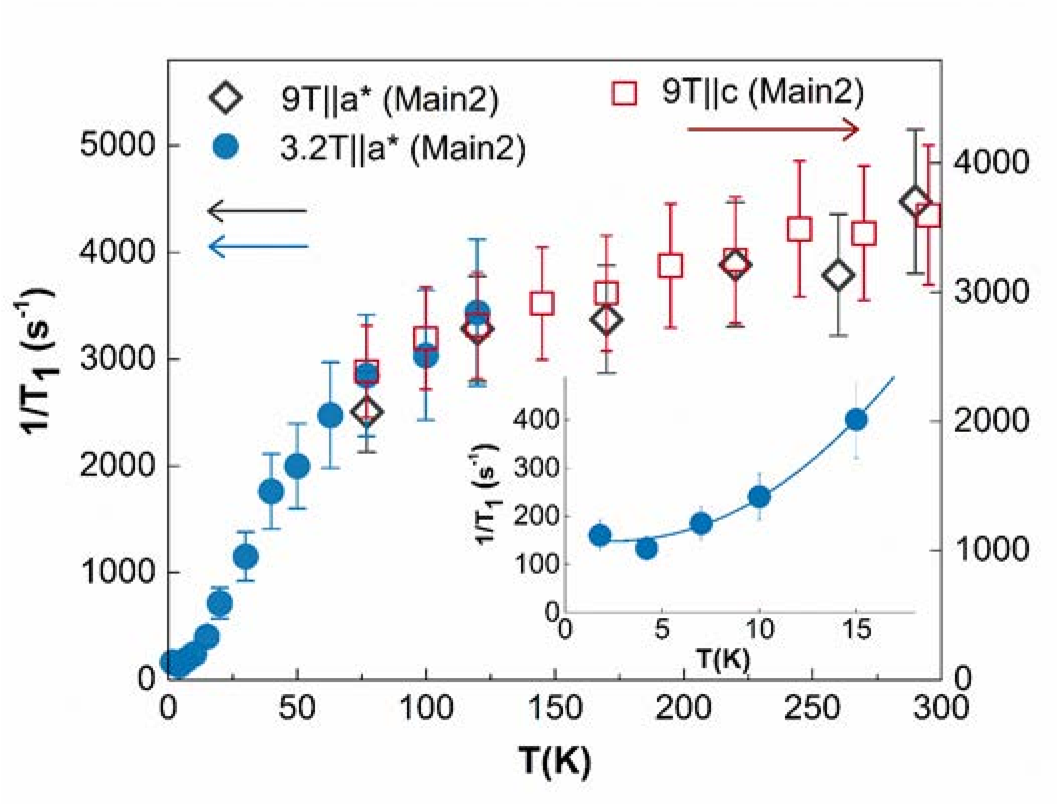

Figure 4.17. The ^{17}O nuclear spin-lattice relaxation rate ${}^{17}1/T_1$ of the intrinsic *Main* (or *Main2*) sites in $B_{ext} \parallel$ c and $B_{ext} \parallel a^*$ measured using the isolated uppermost satellite peak. Inset: Magnification of the low-temperature region of the main panel. The solid line represents the empirical fit ${}^{17}1/T_1 \sim T^2 exp(-\Delta/T) + ({}^{17}1/T_1)_{defect}$ of ${}^{17}1/T_1$ data below ~15 K, which yields $({}^{17}1/T_1)_{defect} \sim 150 s^{-1}$ and Δ ~6.7 K at 3.2 T.

This fit yields a constant defect contribution $({}^{17}1/T_1)_{defect} \sim 150s^{-1}$ and a spin gap Δ of ~6.7 K at 3.2 T. This magnitude of Δ is consistent with that estimated from ${}^{17}K^{(a*)}$ in Figure 4.5 and 4.9, i.e., Δ ~6.8 K.

4.5 Summary

For the $B_{ext} \parallel a*$ geometry, the *Main1* ^{17}O sites show a surprisingly small value of the quadrupole frequency $\nu_Q^{(a*)} \sim 8\text{kHz},$ which results in the bundling of the five resonance peaks of *Main1* into an exceptionally large peak. Such a feature enabled us to clearly identify the *Main 1* peak down to *T* ~0.01 *J* (*J* ~200 K), thereby uncovering the low-temperature behavior of the intrinsic spin susceptibility χ_{kagome} using its Knight shift ${}^{17}K_{Main1}^{(a*)}$.

From the ^{17}O NMR Knight shift measurements, we demonstrated that χ_{kagome} asymptotically tends to zero below T ~0.03 *J* (*J* ~200 K), revealing the presence of a finite gap Δ in the spin excitation spectrum. The magnetic field dependence of the gap follows the expected linear behavior $\Delta\left(B_{ext}\right) = \Delta(0) - g\mu_B SB$. Based on the best linear fit with free parameters, we deduced the zero-field gap $\Delta(0) = 0.03J \sim 0.07J$; this gap closes under a strong magnetic field $B_c \sim 9T$. Moreover, the spin-lattice relaxation rate ${}^{17}1/T_1$ of the *Main2* ^{17}O sites measured at $B_{ext} = 3.2\ T \parallel a*$ exhibits a dramatic decrease below ~60 K, suggesting that the intrinsic low-energy spin excitations diminishes toward

$T = 0$. The gap estimated from the low-temperature behavior of $^{17}1/T_1$ agrees well with that deduced from $^{17}K^{(a^*)}$. Thus, our ^{17}O NMR measurements conducted with $B_{ext} \parallel a^*$ provide concrete evidence for a gapped QSL state in the $S = 1/2$ kagomé lattice of $ZnCu_3(OH)_6Cl_2$. These results serve as the first experimental verification of the recent numerical predictions for the kagomë Heisenberg antiferromagnet described in Ref. [33, 34].

Chapter 5

Defect-induced Phenomena in $ZnCu_3(OH)_6Cl_2$

We now focus on the interplay between the Cu^{2+} defects and the physical properties of the kagomé lattice in $ZnCu_3(OH)_6Cl_2$. As described in Chapter 3, the Cu^{2+} defects occupy the interlayer Zn sites with ~15% probability, which causes the large Curie-Weiss enhancement of the bulk susceptibility χ_{bulk} below ~50 K. Unlike isolated free spins, these S = 1/2 Cu^{2+} defect spins interact with the constituent Cu^{2+} of the kagomé planes directly above and below. Such interaction may have direct impact on the local environment surrounding the defect spins. Here, we describe the temperature dependence of the NMR linewidth of the *Main* ^{17}O sites as well as the behavior of the ^{17}O quadrupole frequency ν_Q, through which we gain additional insight into how the Cu^{2+} defects effect the intrinsic properties of the kagomé lattice.

5.1 NMR Line Broadening of Main ^{17}O Sites

As noted in Chapter 4, the NMR lineshapes measured in both the $B_{ext} \parallel c$ and the $B_{ext} \parallel a^*$ field orientations exhibit dramatic broadening with decreasing temperature. In addition, a comparison of the lineshapes obtained for two different field values of 9 and 3.2T applied along the a^*-axis (Figures 4.2 and 4.4A) revealed that the increase in linewidth is proportional to the magnitude of B_{ext}. This feature implies that the observed broadening of the NMR lineshapes mainly results from the distribution of the Knight shift.

To clarify the mechanism behind such line broadening, we summarize the temperature dependence of the full-width at half-maximum (FWHM) of the *Main1* peak and the uppermost satellite peak of *Main2* in Figure 5.1. The FWHM of both *Main1* and *Main2* peaks shows strong enhancement below ~50 K, similar to the Curie-Weiss behavior of the defect spin susceptibility χ_{defect}, as reflected by the Knight shift $^2K_{NN}$ of the *NN* ^{2}D sites previously observed for deuterated $ZnCu_3(OD)_6Cl_2$ single crystals. These results suggest the following: the interlayer Cu^{2+} defect spins are magnetically polarized along B_{ext} at low temperatures in proportion to $B_{ext} \cdot \chi_{defect}$. These Cu^{2+} defects interact with the Cu^{2+} spins occupying the neighboring kagomé sites and thereby generates spin polarizations within the kagomé plane. Such defect-induced spin polarization is the strongest at the *NN* [$Cu_3(OH)_3$] triangles; however, it is not limited to the *NN* sites but extends throughout the kagomé plane. Owing to the quenched randomness of the Cu^{2+} defects, the line broadening of the *Main* ^{17}O sites follows the Curie-Weiss behavior of χ_{defect}. We note that analogous NMR line broadening is commonly observed in other systems involving magnetic defects, including Kondo impurities in conventional metals and Zn-doped high-T_c cuprates [85, 86, 95].

The magnitudes and directions of the spin polarization vary depending on the distance of the kagomé sites from the defects, in analogy with Mn-doped Cu metals [95]. The polarization of the Cu^{2+} defects induces a net spin density pointing antiparallel to B_{ext} in the s-orbitals of *NN* ^{17}O, leading to the large negative hyperfine coupling $A_{hf}^{defect} < 0$ at the *NN* ^{17}O sites. Moreover, the broadening of the ^{17}O lineshapes is asymmetric, with more spectral weight distributed on the high-frequency end. This high-frequency tail with very fast T_2 is most likely contributed by the *NNN* ^{17}O sites that are affected by a positive Curie-Weiss like spin polarization (see Figures 3.9 and 4.2). However, the NMR peaks of the *NNN* ^{17}O sites do not split off for either field orientations at low temperatures. In fact, their NMR properties are so similar to the *Main* peaks that they can be distinguished only near 295 K, where the peaks are very narrow. This feature of *NNN* ^{17}O sites indicates that, in contrast to the long-range Kondo oscillation typically observed in conventional metals [85, 95], the defect-induced spin polarization in $ZnCu_3(OH)_6Cl_2$ dies out within a very short distance inside the kagomé plane. This observation is consistent with the short-range nature of the spin correlations expected for a gapped state, in which the spin-spin correlation length is expected to be comparable to the Cu-Cu distance [33, 34].

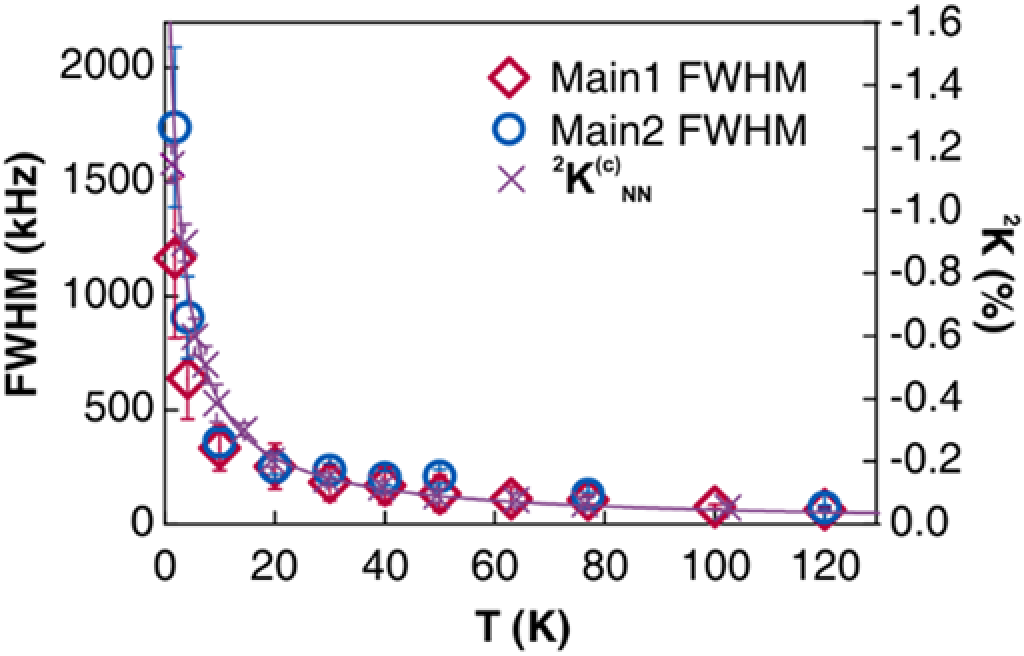

Figure 5.1. Full-width at half-maximum (FWHM) of *Main1* and the uppermost satellite peak of *Maint2* measured at $B_{ext} = 3.2\ T \parallel a^*$ in comparison with $^2K^{(c)}$ of the *NN* ^{2}D sites.

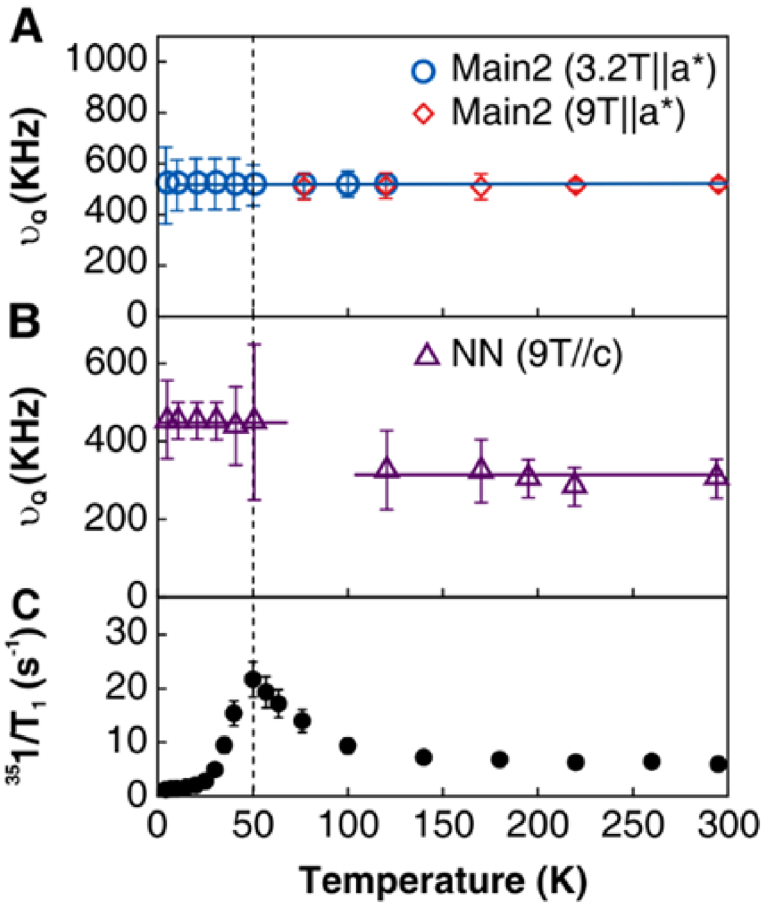

Figure 5.2. The temperature dependence of ν_Q at the *Main2* **(A)** and *NN* sites **(B)**. ν_Q at the *Main2* sites remains constant, whereas ν_Q at the NN sites shows a noticeable change below ~100 K. Earlier ^{35}Cl powder NMR measurements reported the enhancement of the ^{35}Cl nuclear spin-lattice relaxation rate $^{35}1/T_1$ below ~100 K [81], as confirmed here for $B_{ext} = 3.2\ T \parallel a^*$ **(C)**. The observed change of ν_Q at *NN* sites combined with the behavior of $^{35}1/T_1$ suggests that the lattice near the *NN* ^{17}O sites gradually develops a distortion below ~100 K. However, the average crystal structure does not change as a function of temperature.

5.2 ^{17}O Quadrupole Frequency

The quadrupole frequency ν_Q measures the strength of the nuclear quadrupole interaction, which is the coupling between the quadrupole moment of the nucleus Q and the electric field gradient (EFG) originated from the charge distribution surrounding the nucleus. Since the EFG is sensitive to changes in the local structural environment, ν_Q provides a means for probing lattice distortions occurring in the vicinity of the nucleus under study.

As shown in Figure 5.2B, the *NN* ^{17}O sites have a quadrupole frequency $\nu_Q \sim 300kHz$ in the high-temperature regime at $B_{ext} = 3.2\ T \parallel a^*$. The NMR peaks of the *NN* ^{17}O sites became hardly observable between ~50 K and ~100 K; however, they gradually reappeared in the lineshapes with a larger $\nu_Q \sim 450kHz$ below 50 K. This feature indicates that the lattice environment surrounding the Cu^{2+} defects gradually distorts at low temperatures. In contrast, ν_Q of the *Main2* ^{17}O sites measured at $B_{ext} = 3.2\ T \parallel a^*$ remains constant over the entire temperature range, as shown in Figure 5.2A; therefore, the lattice distortion is limited within the vicinity of the Cu^{2+} defects, and the average structure of the kagomé lattice does not change with temperature. This finding is consistent with the X-ray diffraction measurements that suggest the absence of a global structural phase transition in $ZnCu_3(OH)_6Cl_2$ [70].

Moreover, our group earlier made note of the intriguing temperature dependence of the ^{35}Cl (I = 3/2) spin-lattice relaxation rate $^{35}1/T_1$ for powder samples [81], which provides additional insight into the local structure distortion near the Cu^{2+} defects. As shown in Fig. 5-3, $^{35}1/T_1$ is strongly enhanced below ~100 K and reaches a maximum at ~50 K. The peak of $^{35}1/T_1$ shifts to lower temperature as the ^{35}Cl NMR frequency f_{NMR} decreases (f_{NMR} is proportional to the applied field strength as $f_{NMR} = {}^{35}\gamma_N\, B_{ext}$), In contrast, $^{1}1/T_1$ of ^{1}H decreases smoothly below ~100 K without exhibiting a peak. As ^{1}H has a nuclear spin I=1/2, $^{1}1/T_1$ is insensitive to the lattice fluctuations. Thus, we conclude that the peak of $^{35}1/T_1$ near ~50 K results from the enhancement of lattice fluctuations at f_{NMR}, and the frequency-dependent peak of $^{35}1/T_1$ indicates slow freezing of the lattice vibrations. For our ^{17}O enriched single crystal, we confirmed that $^{35}1/T_1$ observed at $B_{ext} =$ 3.2 $T \parallel a^*$ displays similar behavior as that reported for powder samples, as shown in Figure 5.2C.

Combining the observed change of ν_Q at the *NN* ^{17}O sites and the temperature dependence of $^{35}1/T_1$, we suggest that a local lattice distortion gradually develops near the Cu^{2+} defect below ~100 K, which generates the strong enhancement of lattice fluctuations. As a result, the relaxation rate of the *NN* ^{17}O sites becomes very fast, making the corresponding signals difficult to detect in the lineshapes. At ~50 K and below, a new local structure is established near the Cu^{2+}

defects. Therefore, the relaxation of the ^{17}O sites becomes slow again, leading to the re-emergence of the well-defined *NN* peaks with a different ν_Q value.

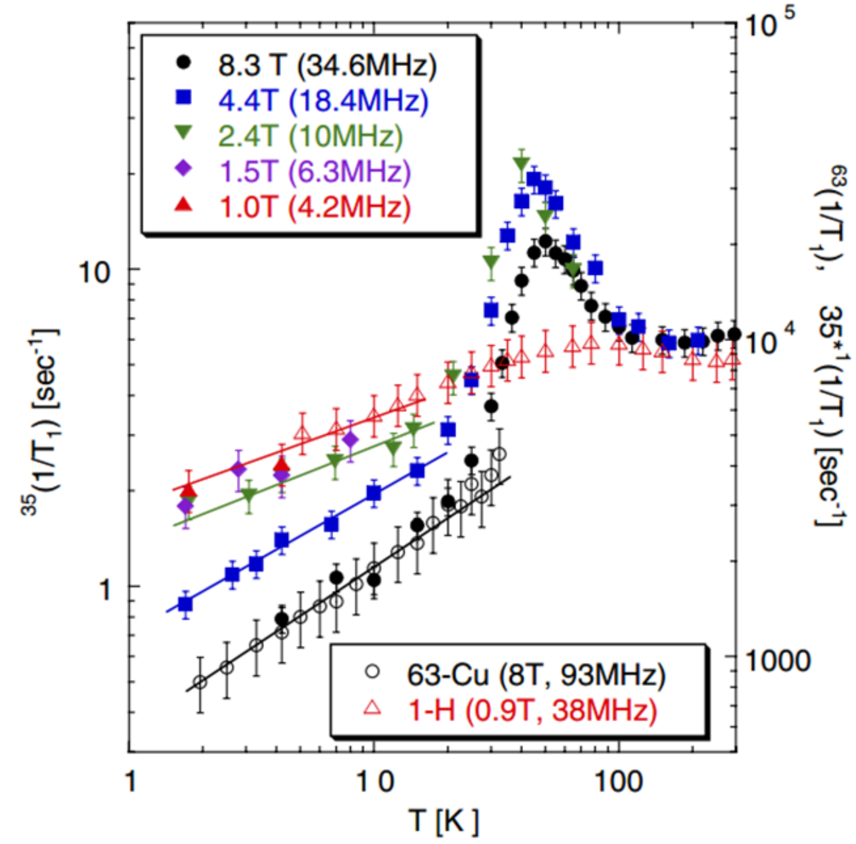

Figure 5.3. Temperature dependence of ^{35}Cl NMR spin-lattice relaxation rate $^{35}1/T_1$ at various magnetic fields (filled symbols). ^{1}H relaxation rate $^{1}1/T_1$ and ^{63}Cu relaxation rate $^{63}1/T_1$ (open symbols) are also superposed on $^{35}1/T_1$ measured in a comparable magnetic field. This figure is reprinted with permission from Ref [81]. Copyright (2008) by American Physical Society.

5.3 Summary

In summary, although the temperature dependence of the average Knight shift of the Main ^{17}O sites, as represented by the peak frequency, reveals the intrinsic gap-behavior of the kagomé lattice in $ZnCu_3(OH)_6Cl_2$, the Main ^{17}O sites are not entirely free of the influence of defects. This influence is reflected in the strong increase in the linewidth of the Main ^{17}O peaks at low temperatures.

Moreover, the quadrupole frequency ν_Q at *NN* ^{17}O sites exhibits a substantial change at low temperatures, revealing a local structure distortion near the Cu^{2+} defects. Nevertheless, the ν_Q of the *Main2* ^{17}O sites remains independent of temperature, which indicates the absence of a global structural distortion in $ZnCu_3(OH)_6Cl_2$.

Chapter 6

Conclusions

In this chapter, we summarize the major results of our ^{17}O single-crystal NMR measurements in $ZnCu_3(OH)_6Cl_2$. As the best realization of the S = 1/2 kagomé Heisenberg antiferromagnet known so far, $ZnCu_3(OH)_6Cl_2$ is among the most promising candidates of a QSL state. However, the presence of defects in this material hindered experimental investigations into its intrinsic ground-state properties. NMR is an ideal local probe that has enabled us to unveil the nature of the defects and, more importantly, to distinguish the intrinsic behavior of the kagomé lattice from the defect-induced phenomena.

From NMR lineshape measurements at $B_{ext} = 9T \parallel c$, we successfully identified resonance peaks arising from the nearest-neighbor (*NN*) ^{17}O sites of the Cu^{2+} defects occupying the interlayer Zn sites. Based on their relative integrated intensity, we estimated that the *NN* ^{17}O sites account for approximately ~15% of the total population, which implies that the S = 1/2 Cu^{2+} defects replace the nonmagnetic Zn^{2+} with ~15% probability (equivalent to ~5% of excess Cu^{2+} at Zn^{2+} sites). This finding is consistent with the ^{2}D NMR [82] and the anomalous X-ray diffraction measurements [70] on single crystals. In the presence of a magnetic field

B_{ext}, the polarized Cu^{2+} defects induce a strong Curie–Weiss-like spin polarization at the *NN* ^{17}O sites due to the hybridization effect. The transfer hyperfine coupling associated with the polarization is negative, namely $A_{hf}^{defect} < 0$. Consequently, the Knight shift $^{17}K_{NN}^{(c)}$ at the *NN* ^{17}O sites is dominated by a large, negative Curie–Weiss contribution at low temperatures, similar to the case of the *NN* ^{2}D sites [82]. Moreover, we emphasize that our ^{17}O single-crystal lineshapes show no evidence for the presence of nonmagnetic Zn^{2+} on the kagomé Cu^{2+} sites, in disagreement with the earlier ^{17}O powder-NMR study [78]. The comparison of the ^{17}O powder-averaged spectra with our high-resolution single-crystal lineshapes reveals that Ref. [78] misidentified the *NN* ^{17}O sites of the magnetic Cu^{2+} defects as the ^{17}O sites neighboring the Zn anti-site defects inside the kagomé plane. Thus, the results from our ^{17}O single-crystal NMR measurements eliminate the possibility of anti-site disorder being the trivial cause of the paramagnetic ground state of $ZnCu_3(OH)_6Cl_2$.

We found that the application of B_{ext} along the a*-axis provides the optimal condition for investigating the low temperature behavior of the intrinsic spin susceptibility χ_{kagome}. In the $B_{ext} \parallel a^*$ geometry, we identified the ^{17}O NMR signals arising from the two inequivalent *Main* ^{17}O sites, *Main1* and *Main2*, with an integrated intensity ratio of 2:1. Owing to the very small quadrupole frequency $\nu_Q^{(a^*)} \sim 8\text{kHz}$, the five $I_z = m$ to $m+1$ resonance peaks of the *Main1* ^{17}O sites are bundled into a single large peak that we could identify at temperatures as low as 1.8K (~0.01*J*). Such a feature also allowed us to measure the *Main1* peak selectively by applying the optimal RF pulse duration for observation of all five NMR transitions simultaneously [56].

By tracking the temperature dependence of the Knight shift ${}^{17}K_{Main1}^{(a*)}$ at *Main1* ^{17}O sites, we demonstrated that χ_{kagome} asymptotically tends to zero below T ~0.03J (J ~200K), which indicates the presence of a finite gap Δ in the spin excitation spectrum. The field dependence of the spin gap $\Delta\left(B_{ext}\right)$ exhibits the expected linear behavior $\Delta\left(B_{ext}\right) = \Delta(0) - g\mu_B SB_{ext}$ and the application of a high magnetic field B_c ~ 9T completely suppresses the gap. The best linear fit yields the zero-field gap $\Delta(0) = 0.03J \sim 0.07J$, which is comparable with the numerical prediction, $\Delta(0) \sim 0.1J$, based on DMRG calculations [33, 34]. Moreover, the low-temperature behavior of the ^{17}O nuclear spin-lattice relaxation rate ${}^{17}1/T_1$ observed at the *Main2* ^{17}O sites at $B_{ext} = 3.2\text{T} \parallel a*$ is consistent with the diminishing intrinsic spin excitations toward $T = 0$. The magnitude of Δ deduced from ${}^{17}1/T_1$ agrees very well with that extracted from ${}^{17}K^{(a*)}$. These results provide strong evidence for a gapped quantum spin-liquid state in the $S = 1/2$ kagomé lattice of ZnCu$_3$(OH)$_6$Cl$_2$.

The linewidth of the *Main*1 peak and the uppermost satellite peak of *Main2* measured at $B_{ext} = 3.2\text{T} \parallel a*$ increases strongly below ~ 50 K, in analogy with the Curie–Weiss behavior of χ_{defect} at low temperatures. This feature seems to imply that the Cu^{2+} defect spins induce a short-range spin density oscillation within the kagomé layers, thereby causing the widely distributed Knight shift ${}^{17}K$ among the intrinsic *Main* ^{17}O sites. Such dramatic line broadening leads to the large uncertainties in the magnitude of $^{17}K_{Main1}^{(a*)}$ below 10K, which prevented us from definitely determining the nature of the lowest-lying excited state based on the linear slope of $\Delta\left(B_{ext}\right)$.

Moreover, we found that the quadrupole frequency ν_Q at *NN* ^{17}O sites exhibits a noticeable change at low temperatures. Combined with the frequency-dependent peak observed for $^{35}1/T_1$, our results indicate a local structure distortion in the vicinity of the Cu^{2+} defects. In contrast, ν_Q of the *Main2* ^{17}O sites measured at $B_{ext} = 3.2\mathrm{T} \,||\, a*$ remains constant over the entire temperature range. Therefore the average structure of the kagomé lattice does not change with temperature. This finding is in agreement with the X-ray diffraction measurements that show no evidence for a global structural phase transition in $ZnCu_3(OH)_6Cl_2$.

Bibliography

[1] L. Balents, Nature, **464**, 199 (2010).

[2] P. A. Lee, Science, **321**, 1306 (2008).

[3] Physics Today, **60**, (2), 16 (2007).

[4] C. Lhuillier and G. Misguich, “Introduction to Quantum Spin Liquids” in *Introduction to Frustrated Magnetism*, edited by C. Lacroix, P. Mendels, and F. Mila (Springer Series in Solid-State Sciences, 2011) Vol. 164.

[5] P. W. Anderson, Science **235**, 1196 (1987).

[6] B. Normand, Contemporary Physics **50**, 533 (2009).

[7] P. A. Lee, Reports on Progress in Physics, **71**(1), 012501, (2008).

[8] S. Liang, B. Doucot and P. W. Anderson, Phys. Rev. Lett. **61**, 365 (1988).

[9] F. Alet, A. M. Walczak, and M. P. A. Fisher, Physica A **369**, 122 (2006).

[10] X.-G. Wen, *Phys. Rev. B.* **65**, 165113 (2002).

[11] Y. Ran, M. Hermele, P. A. Lee, and X.-G. Wen, Phys. Rev. Lett. **98**, 117205 (2007).

[12] M. Hermele, Y. Ran, P. A. Lee, and X.-G. Wen, Phys. Rev. B. **77**, 224413 (2008).

[13] P. Lecheminant, “One-Dimensional Spin Liquids” in *Frustrated Spin Systems*, edited by H. T. Diep (World scientific, Singapore, 2004).

[14] J. C. Bonner and M. E. Fisher, Phys. Rev. A. **135**, 640 (1964).

[15] L. D. Faddeev and L. A. Takhtajan, Phys. Lett. A, **85**, 375 (1981).

[16] D. A. Tennant, R. A. Cowley, S. E. Nagler, and A. M. Tsvelik, Phys. Rev. B **52**, 13368 (1995).

[17] J. S. Helton, PhD thesis, Massachusetts Institute of Technology, 2009.

[18] N. D. Mermin and H. Wagner, Phys. Rev. Lett. **17**, 1133 (1966).

[19] J. T. Chalker, “Geometrically Frustrated Antiferromagnet: Statistical Mechanics and Dynamics” in *Introduction to Frustrated Magnetism*, edited by C. Lacroix, P. Mendels, and F. Mila (Springer Series in Solid-State Sciences, 2011) Vol. 164.

[20] A. P. Ramirez, Annu. Rev. of Mater. Sci. **24**, 453 (1994).

[21] Y. Shimizu, K. Miyagawa, K. Kanoda, M. Maesato, and G. Saito, Phys. Rev. Lett. **91**, 107001 (2003).

[22] S. Yamashita *et al*., Nat. Phys. **4**, 459 (2008).

[23] T. Itou, A. Oyamada, S. Maegawa, R. Kato, Nature Phys. **6**, 673 (2010)

[24] M. P. Shore, E. A. Nytko, B. M. Bartlett, and D. G. Nocera, J. Am. Chem. Soc. **127**, 13462 (2005).

[25] Y. Okamoto, H. Yoshida, and Z. Hiroi, J. Phys. Soc. Jpn. **78**(3), 033701 (2009).

[26] M. Yoshida, Y. Okamoto, M. Takigawa, and Z. Hiroi. J. Phys. Soc. Jpn. **82**(1), 013702 (2013).

[27] O. Janson, J. Richter, P. Sindzingre, and H. Rosner. Phys. Rev. B. **82**,104434 (2010).

[28] H. Yoshida, J.-I. Yamaura, M. Isobe, Y. Okamoto, G. J. Nilsen, and Z. Hiroi. Nat. Commun. **3** 860 (2012).

[29] O. Janson, J. Richter, and H. Rosner. Phys. Rev. Lett. **101**, 106403 (2008).

[30] P. Mendels and A. S. Wills, "Kagomé Antiferromagnets: Material Vs. Spin Liquid Behaviors" in *Introduction to Frustrated Magnetism*, edited by C. Lacroix, P. Mendels and F. Mila (Springer Series in Solid-State Sciences, 2011) Vol. 164.

[31] B. D. Gaulin and J. S. Gardner "Experimental Studies of Pyrochlore Antiferromagnets" in *Introduction to Frustrated Magnetism*, edited by C. Lacroix, P. Mendels, and F. Mila (Springer Series in Solid-State Sciences, 2011) Vol. 164.

[32] S. Sachdev, Phys. Rev. B. **45,** 12377 (1992).

[33] S. Yan, D. A. Huse, and S. R. White, Science **332**, 1173 (2011).

[34] S. Depenbrock, I. P. McCulloch, and U. Schollwöck, Phys. Rev. Lett. **109**, 067201 (2012).

[35] Y. M. Lu, Y. Ran, and P. A. Lee, Phys. Rev. B. **83**, 224413 (2011).

[36] H.-C. Jiang, Z. Wang and L. Balents. Nat Phys. **8**, 902 (2012).

[37] Y. Wan and O. Tchernyshyov. Phys. Rev. B. **87**, 104408 (2013).

[38] Z. Hao and O. Tchernyshyov, *Phys. Rev. B.* **87**, 214404 (2013).

[39] F. Mila, Phys. Rev. Lett. **81**, 2356 (1998).

[40] H. C. Jiang, Z. Y. Weng, and D. N. Sheng. Phys. Rev. Lett. **101**, 117203 (2008).

[41] P. Nikolic and T. Senthil, Phys. Rev. B. **68**, 214415 (2003).

[42] R. R. P. Singh and D. A. Huse, Phys. Rev. B. **77,** 144415 (2008).

[43] G. Evenbly and G. Vidal. Phys. Rev. Lett. **104**, 187203 (2010).

[44] D. Poilblanc, M. Mambrini, and D. Schwandt. Phys. Rev. B. **81**, 180402, (2010).

[45] R. Budnik and A. Auerbach. Phys. Rev. Lett. **93**, 187205, (2004).

[46] Y. Iqbal, F. Becca and L. Poilblanc. New. Jour. of. Phys. **14**, 115031 (2012).

[47] S. R. White. Bull. Am. Phys. Soc. **57**. MAR. L19.1 (2012).

[48] P. Sindzingre and C. Lhuillier. Europhys. Lett. **88**, 27009 (2009).

[49] M. Elhajal, B. Canals, and C. Lacroix. Phys. Rev. B. **66**, 014422 (2002).

[50] L. Messio, O. Cépas, and C. Lhuillier. Phys. Rev. B, **81**, 064428 (2010).

[51] Y. Huh, L. Fritz and S. Sachdev. Phys. Rev. B, **81**, 144432 (2010).

[52] Elstner and A. P. Young, Phys. Rev. B **50**, 6871 (1994).

[53] M. Rigol and R. R. P. Singh, Phys. Rev. Lett. **98**, 207204 (2007).

[54] A. Abragam, *Principle of Nuclear Magnetism* (Oxford University Press, Oxford, 1961).

[55] C. P. Slichter, *Principles of Magnetic Resonance* (Springer, New York, 1996).

[56] E. Fukushima and S. B. W. Roedar, *Experimental Pulse NMR: A Nuts and Bolts Approach* (Addison-Wesley, 1981).

[57] R. M. White, *Quantum Theory of Magnetism* (Springer, New York, 1970).

[58] S. Blundell, *Magnetism in Condensed Matter* (Oxford University Press, Oxford, 2001).

[59] N. W. Ashcroft and N. D. Mermin, *Solid State Physics* (Brooks/Cole, 1976).

[60] M. Kardar, *Statistical Physics of Partials* (Cambridge University Press, Cambridge, 2007)

[61] C. Cohen-Tannoudji, B. Diu, and F. Laloë, *Quantum Mechanics* (Wiley and Hermann, Paris, 1977).

[62] V. Jaccarino, *Proc. of Int. School of Physics, Enrico Fermi* (Academic Press, New York, 1967), Vol. 37, pp. 335-385.

[63] A. Abragam and B. Bleaney, *Electron Paramagnetic Resonance of Transition Ions* (Oxford University Press, New York, 1980).

[64] F. Mila and T. M Rice, Physica C **157**, 561 (1989).

[65] B. Shastry, Phys. Rev. Lett. **63**, 1288 (1989).

[66] T. Moriya, J. Phys. Soc. Jpn. **18**, 516 (1963).

[67] A. Narath, Phys. Rev. **162**, 320 (1967).

[68] E. R. Andrew and D. P. Tunstall, Proc. *Phys*. *Soc*. **78**, 1 (1961).

[69] K. R. Thurber, Ph. D. thesis, Massachusetts Institute of Technology, 1999.

[70] D. E. Freedman *et al.*, J. Am. Chem. Soc. **132**, 16185 (2010).

[71] H. A. Jahn and E. Teller, Proceedings of the Royal Society of London, Series A **161**, 220 (1973).

[72] C. K. Jørgensen, *Modern Aspects of Ligand Field Theory* (North-Holland, Amsterdam, 1971).

[73] J.S. Helton *et al*., Phys. Rev. Lett. **98**, 107204 (2007).

[74] P. Mendels *et al*., Phys. Rev. Lett. **98,** 077204 (2007).

[75] M.A.de Vries *et al*., Phys. Rev. Lett. **103,** 237201 (2009).

[76] T.-H. Han *et al*., Phys., Rev. B. **83**, 100402(R) (2011).

[77] T.-H. Han *et al*., Nature **492**, 406 (2012).

[78] A. Olariu *et* al., Phys. Rev. Lett. **100,** 087202 (2008).

[79] Y. Shimizu *et al*., Phys. Rev. Lett. **91**, 107001 (2003).

[80] S. S. Lee and P. A. Lee, Phys. Rev. Lett. **95**, 036403 (2005).

[81] T. Imai, E. A. Nytko, B.M. Bartlett, M.P. Shores, and D. G. Nocera, Phys. Rev. Lett. **100**, 077203 (2008).

[82] T. Imai, M. Fu, T.-H. Han, and Y. S. Lee, Phys. Rev. B. **84**, 020411(R) (2011).

[83] T. Dodds, S. Bhattacharjee, and Y. B. Kim, Phys. Rev. B. **88** 224413 (2013).

[84] M. Punk, D. Chowdhury, and S. Sachdev, Nat. Phys. **10**, 289 (2014).

[85] D. V. Lang, D. C. Lo, J. B. Boyce, and C. P. Slichter, Phys. Rev. B. **9**, 3077 (1974).

[86] J. Bobroff *et al*., Phys. Rev. Lett. **86**, 4116 (2001).

[87] F. Tedoldi, R. Santachiara, and M. Horvatic, Phys. Rev. Lett. **83**, 412 (1999).

[88] K. Matan *et al*., Nat. Phys. **6**, 865 (2010).

[89] T. Han, S. Chu, and Y. S. Lee, Phys. Rev. Lett. **108**, 157202 (2012).

[90] P. A. Lee (private communication).

[91] T. Imai *et al*., Phys. Rev. Lett. **81**, 220 (1998).

[92] M. Itoh *et al.*, Physica C. **263**, 486(1996).

[93] P. Singer *et al*., Phys. Rev. B. **72**, 014537 (2005).

[94] K. R. Thurber *et al*., Phys. Rev. Lett. **87**, 247202 (2001).

[95] A. J. Heeger, A. P. Klein and P. Tu, Phys. Rev. Lett. **17**, 803(1966).

Appendix A

Calculation of T_1 NMR Recovery Curves for $I = 5/2$

In our T_1 measurements, we monitored the recovery of the spin-echo intensity $M(t)$ as a function of the delay time *t*. Then we obtained the magnitude of ${}^{17}1/T_1$ by fitting the observed T_1 recovery curves to the standard formulas for the magnetic relaxation. In this appendix, we describe the procedure for calculating the standard fitting functions for the ^{17}O nuclear spin ($I = 5/2$), following the work of Narath [67] and Andrew and Tunstall [68].

According to the time dependent perturbation theory, the transition probability per unit time $W_{m\leftrightarrow m'}$ between two nuclear energy levels *m* and m' is given by

$$W_{m\leftrightarrow m'} = W\cdot[\langle m'|I^{+}|m\rangle^{2} + \langle m'|I^{-}|m\rangle^{2}]. \tag{A.1}$$

In this equation, *W* is the fundamental transition rate, and $1/T_1 = 2W$ for the case of $I = 1/2$. The quantum operators I^{+} and I^{-} are known as the “raising” and “lowering” operators, respectively, such that

$$I^{+}\left|m\right\rangle = \sqrt{I(I+1)-m(m+1)}\left|m+1\right\rangle; \\ I^{-}\left|m\right\rangle = \sqrt{I(I+1)-m(m-1)}\left|m-1\right\rangle. \tag{A.2}$$

The matrix elements $\left\langle m'\right|I^{+}\left|m\right\rangle$ and $\left\langle m'\right|I^{-}\left|m\right\rangle$ are zero unless $m' = m\pm 1$. The magnetic relaxation can only induce transitions between neighboring nuclear states, and the transition probability can be written as

$$W_{m\leftrightarrow m-1} = W(I+m)(I-m+1). \tag{A.3}$$

For $I = 5/2$, the values of $W_{m\leftrightarrow m-1}$ for the allowed nuclear transitions are

$$W_{-1/2\leftrightarrow +1/2} = 9W; \\ W_{\pm 1/2\leftrightarrow +\pm 3/2} = 8W; \\ W_{\pm 3/2\leftrightarrow +\pm 5/2} = 5W. \tag{A.4}$$

Now we define the deviation from the equilibrium population for each nuclear level as N_m; the coupled rate equations for $I = 5/2$ are written as

$$\dot{N}_{5/2} = -5W(N_{5/2}-N_{3/2}); \\ \dot{N}_{3/2} = 5W(N_{5/2}-N_{3/2}) - 8W(N_{3/2}-N_{1/2}); \\ \dot{N}_{1/2} = 8W(N_{3/2}-N_{1/2}) - 9W(N_{1/2}-N_{-1/2}); \\ \dot{N}_{-1/2} = 9W(N_{1/2}-N_{-1/2}) - 8W(N_{-1/2}-N_{-3/2}); \\ \dot{N}_{-3/2} = 8W(N_{-1/2}-N_{-3/2}) - 5W(N_{-3/2}-N_{-5/2}); \\ \dot{N}_{-5/2} = 5W(N_{-3/2}-N_{-5/2}). \tag{A.5}$$

To convert the above equations to the form presented in Andrew and Tunstall [68], we define $\tilde{N}_{m+1/2} \equiv N_{m+1} - N_m$, and transform Eq. (A.5) to the following $2I = 5$ coupled linear differential equations

$$\begin{aligned}
\dot{\tilde{N}}_2 &= \dot{N}_{5/2} - \dot{N}_{3/2} = (-10\tilde{N}_2 + 8\tilde{N}_1)W;\\
\dot{\tilde{N}}_1 &= \dot{N}_{3/2} - \dot{N}_{1/2} = (5\tilde{N}_2 - 16\tilde{N}_1 + 9\tilde{N}_0)W;\\
\dot{\tilde{N}}_0 &= \dot{N}_{1/2} - \dot{N}_{-1/2} = (8\tilde{N}_1 - 18\tilde{N}_0 + 8\tilde{N}_{-1})W;\\
\dot{\tilde{N}}_{-1} &= \dot{N}_{-1/2} - \dot{N}_{-3/2} = (9\tilde{N}_0 - 16\tilde{N}_{-1} + 5\tilde{N}_{-2})W;\\
\dot{\tilde{N}}_{-2} &= \dot{N}_{-3/2} - \dot{N}_{-5/2} = (8\tilde{N}_{-1} - 10\tilde{N}_{-2})W.
\end{aligned} \tag{A.6}$$

We then write Eq. (A.6) in the matrix form

$$\dot{\tilde{\mathbf{N}}}(t) = W\begin{pmatrix} -10 & 8 & 0 & 0 & 0\\ 5 & -16 & 9 & 0 & 0\\ 0 & 8 & -18 & 8 & 0\\ 0 & 0 & 9 & -16 & 5\\ 0 & 0 & 0 & 8 & -10 \end{pmatrix}\tilde{\mathbf{N}}(t) \tag{A.7}$$

The above 5×5 matrix is denoted as **A**; $\dot{\tilde{\mathbf{N}}}(t)$ and $\tilde{\mathbf{N}}(t)$ are column vectors. The solutions of Eq. (A.6) take the form

$$\tilde{N}_i(t) = \sum_n a_{i,n} exp(-\lambda_n t), \tag{A.8}$$

where λ_n are the eigenvalues of **A** and $\alpha_{i,n}$ are the components of the corresponding eigenvectors. By solving this eigenvalue problem via MATLAB program, we obtained the magnitude of the eigenvalues λ_n as listed below

$$\begin{aligned}
\lambda_1 &= 30W;\\
\lambda_2 &= 20W;\\
\lambda_3 &= 12W;\\
\lambda_4 &= 6W;\\
\lambda_5 &= 2W.
\end{aligned} \tag{A.9}$$

The corresponding matrix of eigenvectors is given by

$$\mathbf{V} = \begin{pmatrix} -0.1976 & -0.4417 & 0.6239 & 0.4472 & -0.6325 \\ 0.4940 & 0.5522 & -0.1560 & 0.4472 & -0.3162 \\ -0.6587 & 0 & -0.4159 & 0.4472 & 0 \\ 0.4940 & -0.5522 & -0.1560 & 0.4472 & 0.3162 \\ -0.1976 & 0.4417 & 0.6239 & 0.4472 & 0.6325 \end{pmatrix} \tag{A.10}$$

To properly normalize the eigenvectors in **V**, we must set the initial condition for each nuclear state, which indicates how the nuclear spin system has been perturbed from thermal equilibrium. For example, when conducting T_1 measurements at the central resonance peak, we inverted the population of the $\left|+1/2\right\rangle$ and $\left|-1/2\right\rangle$ states; accordingly, the initial conditions are $N_{1/2} = -1/2$, $N_{-1/2} = +1/2$, and $N_m = 0$ for $m \neq \pm 1/2$. Converting to the notation $\tilde{N}_{m+1/2} \equiv N_{m+1} - N_m$, we obtained the initial conditions for the central I_z = - 1/2 to +1/2 NMR transition

$$\tilde{\mathbf{N}}_0(0) = \begin{pmatrix} 0 \\ 1/2 \\ -1 \\ 1/2 \\ 0 \end{pmatrix} \tag{A.11}$$

Similarly, the initial conditions for the I_z = ±3/2 to ±1/2 and I_z = ±5/2 to ±3/2 transitions are given by

$$\tilde{\mathbf{N}}_1(0) = \begin{pmatrix} 1/2 \\ -1 \\ 1/2 \\ 0 \\ 0 \end{pmatrix} \text{ and } \tilde{\mathbf{N}}_2(0) = \begin{pmatrix} -1 \\ 1/2 \\ 0 \\ 0 \\ 0 \end{pmatrix} \tag{A.12}$$

Then the components $a_{i,n}$ of the properly normalized eigenvectors can be calculated based on the relation

$$a_{m,n} = V_{m.n} \sum_i (V^{-1})_{n,i} \tilde{N}_i(0), \tag{A.13}$$

where $(V^{-1})_{n,i}$ are the components of the inverse matrix of **V**, which is

$$\mathbf{V}^{-1} = \begin{pmatrix} -0.1205 & 0.4820 & -0.7230 & 0.4820 & -0.1205 \\ -0.3234 & 0.6468 & 0 & -0.6468 & -0.3234 \\ 0.5343 & -0.2137 & -0.6412 & -0.2137 & 0.5343 \\ 0.3194 & 0.5111 & 0.5750 & 0.5111 & 0.3194 \\ -0.5647 & -0.4518 & 0 & 0.4518 & 0.5467 \end{pmatrix} \tag{A.14}$$

For the central I_z = - 1/2 to +1/2 transition, we solved for $a_{3,n}$, where the index 3 indicates the third row of **V**, such that

$$\begin{aligned} a_{3,1} &= -0.6587 \cdot \left[(\frac{1}{2} \cdot 0.4820) + \left(1 \cdot 0.7230\right) + (\frac{1}{2} \cdot 0.4820) \right] = -0.7936; \\ a_{3,3} &= -0.4159 \cdot \left[(-\frac{1}{2} \cdot 0.2137) + \left(1 \cdot 0.6412\right) + (-\frac{1}{2} \cdot 0.2137) \right] = -0.1778; \\ a_{3,4} &= 0.4472 \cdot \left[(\frac{1}{2} \cdot 0.5111) + \left(-1 \cdot 0.5750\right) + (\frac{1}{2} \cdot 0.5111) \right] = -0.0286; \\ a_{3,2} &= a_{3,5} = 0. \end{aligned} \tag{A.15}$$

Using the conventional unit, $1/T_1 = 2W$, we wrote the recovery of nuclear magnetization $M(t)$ as $\dfrac{M(t)}{M(\infty)} = 1 - \tilde{N}(t)$. Substituting Eq. (A.9) and (A.15) into Eq. (A.8), we obtained the standard fitting form for the T_1 recovery at the central I_z = - 1/2 to +1/2 transition

$$\frac{M(t)}{M(\infty)} = 1 - \left[0.7936 \cdot exp\left(-\frac{15t}{T_1}\right) + 0.1778 \cdot exp\left(-\frac{6t}{T_1}\right) + 0.0286 \cdot exp\left(-\frac{t}{T_1}\right)\right]. \tag{A.15}$$

Following the same procedure, we calculated the T_1 recovery for the first satellite (I_z = ±3/2 to ±1/2) transition

$$\begin{aligned}\frac{M(t)}{M(\infty)} = 1 - \Bigg[&0.4464 \cdot exp\left(-\frac{15t}{T_1}\right) + 0.4464 \cdot exp\left(-\frac{10t}{T_1}\right) + 0.025 \cdot exp\left(-\frac{6t}{T_1}\right) \\ &+0.0536 \cdot exp\left(-\frac{3t}{T_1}\right) + 0.0286 \cdot exp\left(-\frac{t}{T_1}\right)\Bigg],\end{aligned} \tag{A.16}$$

and for the second satellite (I_z = ±52 to ±3/2) transition

$$\begin{aligned}\frac{M(t)}{M(\infty)} = 1 - \Bigg[&0.0714 \cdot exp\left(-\frac{15t}{T_1}\right) + 0.2857 \cdot exp\left(-\frac{10t}{T_1}\right) + 0.4 \cdot exp\left(-\frac{6t}{T_1}\right) \\ &+0.2143 \cdot exp\left(-\frac{3t}{T_1}\right) + 0.0286 \cdot exp\left(-\frac{t}{T_1}\right)\Bigg].\end{aligned} \tag{A.17}$$

Appendix B

Goniometer Design for Single-Crystal NMR Measurements

The ^{17}O single-crystal NMR measurements presented in this thesis were conducted in two different field geometries, $B_{ext} \parallel c$ and $B_{ext} \parallel a^*$. To ensure accurate alignment of the static magnetic field B_{ext} with respect to the crystalline axis, we designed a two-axis goniometer for our 4K NMR probe, as shown in Fig. B-1. The goniometer comprises three parts, labelled as (a), (b) and (c), respectively. This design enables rotations about two orthogonal axes, both perpendicular to the direction of B_{ext} (i.e. the reference direction of the goniometer). We glued the single crystal onto the flat platform of Part a) (see Fig. B-2) and manually oriented Part a) and b) to align the crystalline axis of interest to the reference direction of the goniometer. X-ray diffraction (XRD) measurements were employed to guide the manual orientation and to confirm the correct crystal alignment. The accuracy of our crystal alignment is approximately $\pm 1^\circ$.

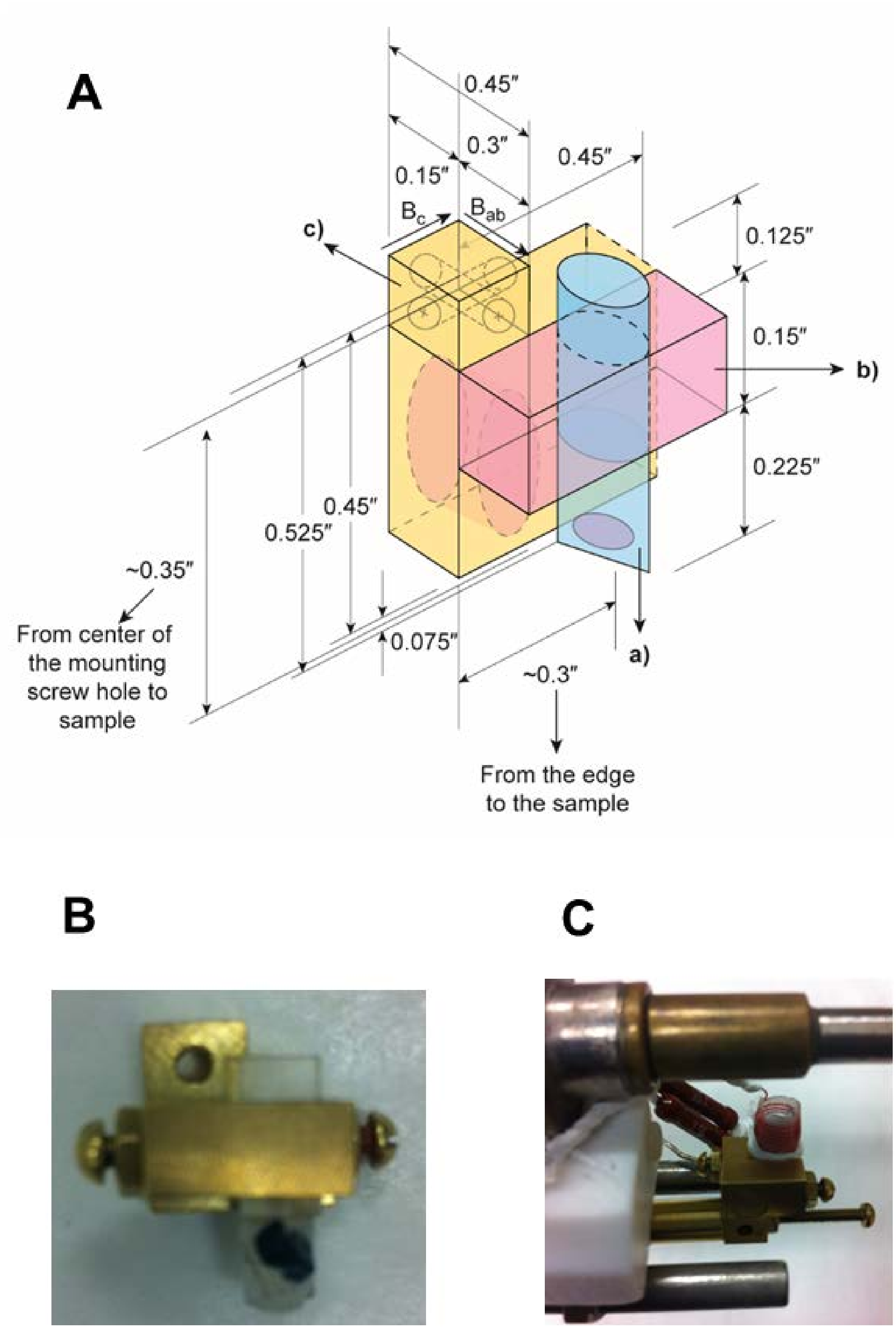
A
0.45″
0.3″
0.15″
0.45″
B_c
B_{ab}
c)
0.125″
0.15″
b)
0.225″
0.45″
0.525″
~0.35″
From center of the mounting screw hole to sample
0.075″
a)
~0.3″
From the edge to the sample
B
C

Figure B.1. Design for the two-axis goniometer. **(A)** Schematic drawing of the goniometer; the three constituent parts are indicated in different colors. **(B)** Photo of the goniometer. **(C)** The goniometer mounted onto the 4K NMR probe head.

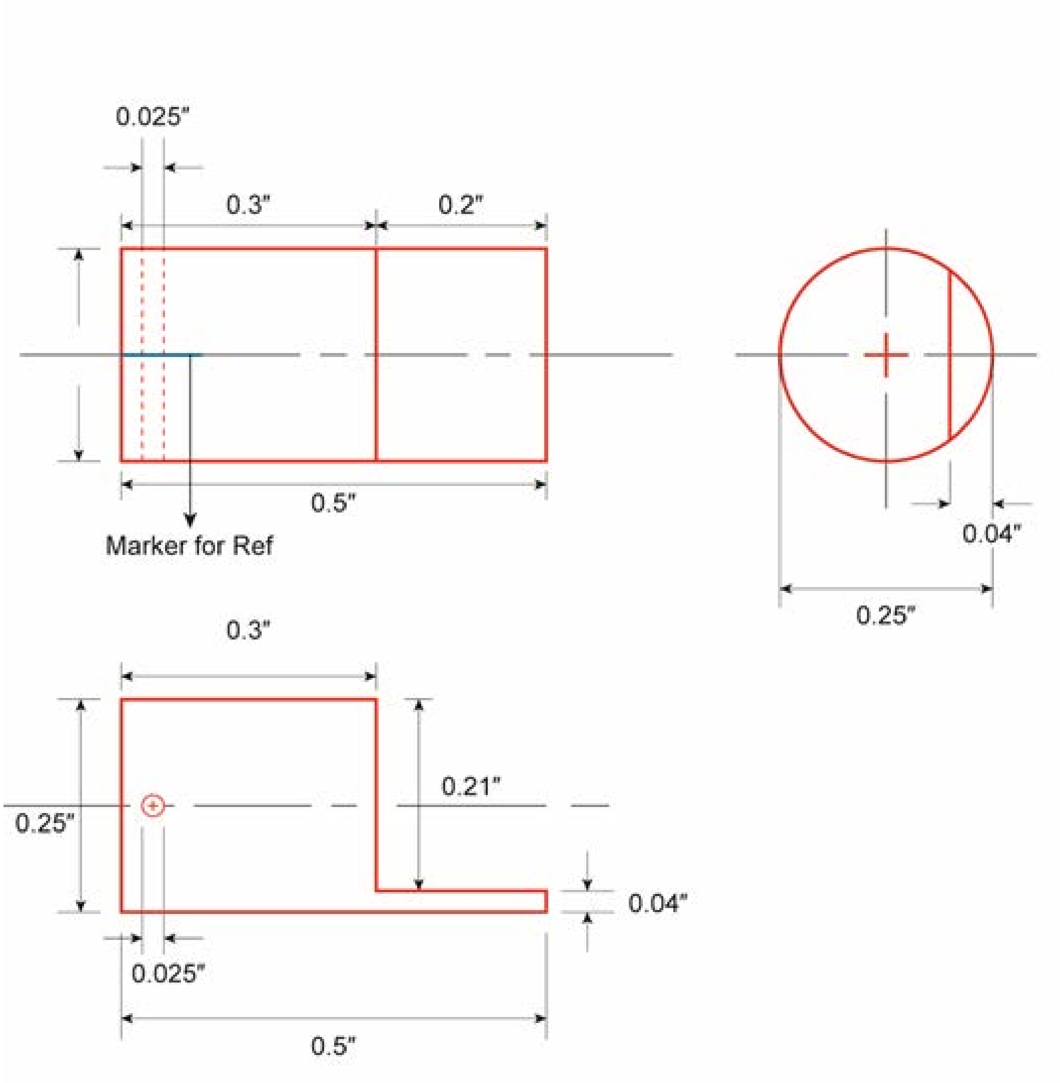

Figure B.2. Technical drawing for Part (a) of the goniometer.

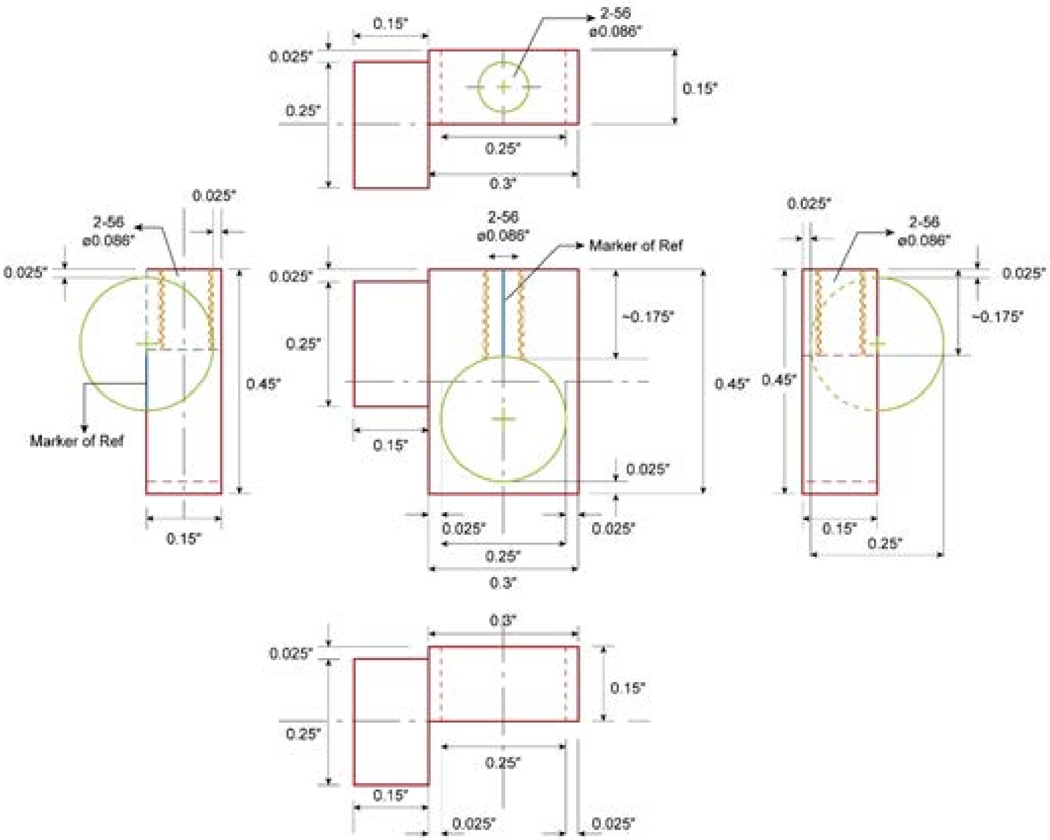

Figure B.3. Technical drawing for Part (b) of the goniometer.

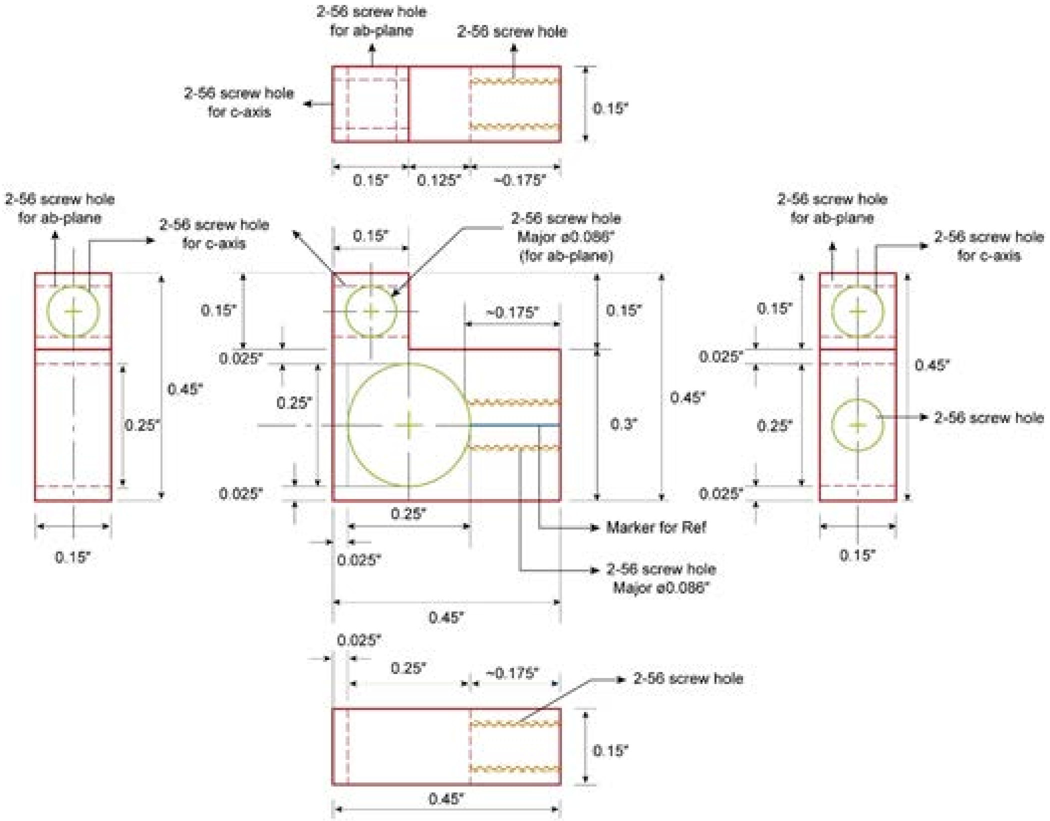

Figure B.4. Technical drawing for Part (c) of the goniometer.